Contents

ASM Sc. J.
Volume 2(2), 2008

RESEARCH ARTICLES

Continued on the inside of the back cover.

ISSN 1823-6782

MOSTI

AKADEMI SAINS MALAYSIA

ASM Science Journal 2(2) 2008

ASM Science JOURNAL

In Pursuit of Excellence in Science

Vol. 2, No. 2, December 2008 • ISSN : 1823-6782

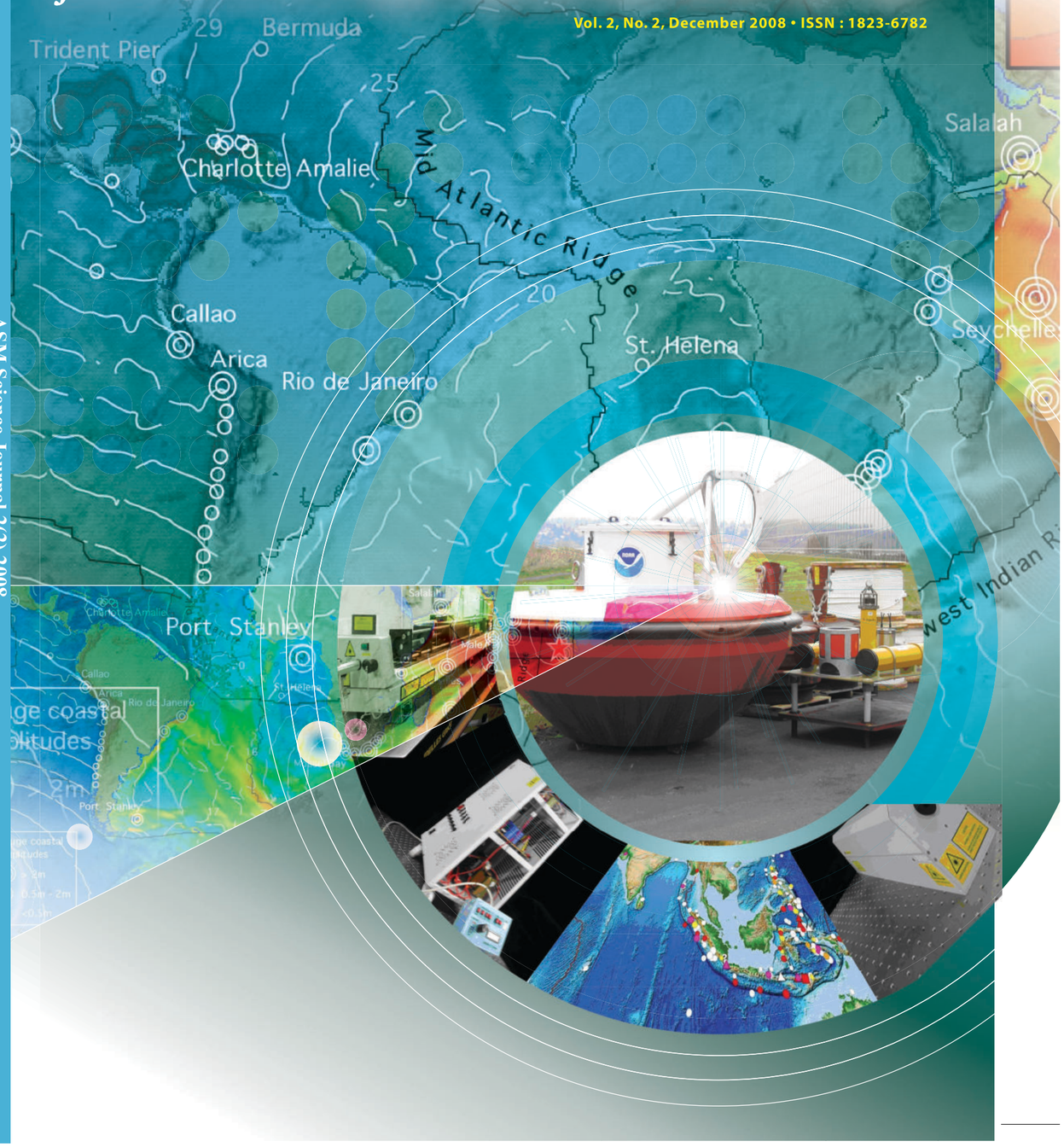

ASM Science
JOURNAL

Editorial

In this fourth issue and second volume of the Journal, an attempt is made to introduce the thematic issue of *photonics*. The term describes the 'combination of light technologies and electronics in telecommunication' which now can be defined 'as the field in science, medicine and technology investigating and using laser light'.

ASM Science Journal is mainly a multi-disciplinary one but periodically, adhering to the aims and objectives, a collection of articles devoted to a single subject area is deemed fit to be published. This is to address current impending issues and the demands cum needs of the scientific community and society pertaining to a specific area of a scientific discipline. The next thematic issue will be on Antarctic research.

The Editorial Board is grateful to the guest editor, Prof Harith Ahmad of University of Malaya and his committee comprising experts in the area of photonics who selected, reviewed and approved nine research articles (pp. 107–168), covering a myriad of topics on tuning range characteristics, multiwavelength fiber laser, design of variable gain-flattened EDFA, wideband double-pass Raman fiber amplifier, chromatic dispersion measurement technique, the effect of fiber length on SNR in laser linewidth measurement, fabrication tolerance, loss analysis, grating waveguide, polarisation splitter, resonant tunnelling, Er-Yb co-doped phosphate DFB laser, optical code generating device and erbium/ytterbium co-doped fiber amplifier, etc.

To complement the R&D articles on photonics, a topic on science forum (pp. 169–182) which describes laser research at the University of Technology Malaysia, addressing the broad field of spectrum from laser materials, electronic devices and laser application was also included.

Prof Md. Ikram Mohd Said
Editor-in-Chief/Chairman, Editorial Board *ASM Sc. J.*

Cover:

Background is a portion of a map extracted from a figure (p. 173) showing numerical modeling of the computed tsunami amplitudes around the globe after the 26 December 2004 Indian Ocean Tsunami; in the centre of the concentric circle is the Deep Ocean Alerting and Reporting of Tsunami (DART) buoy's main component and pressure transducer (p. 174); the section of the map in the lower sector of the figure shows the Sunda arc (p. 171), the area responsible for 80% of the tsunamis recorded in the Indian Ocean (Source: National Oceanic and Atmospheric Administration, US Department of Commerce)—all from the review article on *Tsunami Warning Systems* (pp. 169–177).

The rest of the gadgets shown are the laser head and flashlamp drive—the first laser developed solid state Nd:YAG at University Technology Malaysia (p. 180), and the Q-switched Nd:YAG laser system (p. 179)—from the article on *Laser Research at the University of Technology Malaysia* (pp. 179–182).

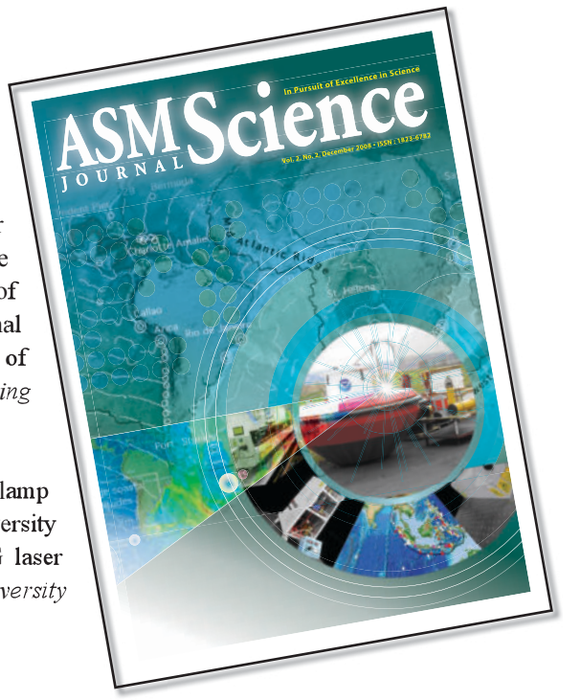

The Academy of Sciences Malaysia (ASM)

The Academy of Sciences Malaysia (ASM) was established, under the *Academy of Sciences Act 1994* which came into force on 1 February 1995, with the ultimate aim to pursue excellence in science. Thus the mission enshrined is to pursue, encourage and enhance excellence in the field of science, engineering and technology for the development of the nation and the benefit of mankind.

The functions of the Academy are as follows:

- To promote and foster the development of science, engineering and technology
- To provide a forum for the interchange of ideas among scientists, engineers and technologists
- To promote national awareness, understanding and appreciation of the role of science, engineering and technology in human progress
- To promote creativity among scientists, engineers and technologists
- To promote national self-reliance in the field of science, engineering and technology
- To act as a forum for maintaining awareness on the part of the Government of the significance of the role of science, engineering and technology in the development process of the nation and for bringing national development needs to the attention of the scientists, engineers and technologists
- To analyse particular national problems and identify where science, engineering and technology can contribute to their solution and accordingly to make recommendations to the Government
- To keep in touch with developments in science, engineering and technology and identify those developments which are relevant to national needs to bring such developments to the attention of the Government
- To prepare reports, papers or other documents relating to the national science, engineering and technology policy and make the necessary recommendations to the Government
- To initiate and sponsor multi-disciplinary studies related to and necessary for the better understanding of the social and economic implications of science, engineering and technology
- To encourage research and development and education and training of the appropriate scientific, engineering and technical man power
- To establish and maintain relations between the Academy and overseas bodies having the same or almost similar objectives in science, engineering and technology as the Academy
- To advise on matters related to science, engineering and technology as may be requested by the Government from time to time; and
- To carry out such other actions that are consistent with the *1994 Academy of Sciences Act* as may be required in order to facilitate the advancement of science, engineering and technology in Malaysia, and the well being and status of the Academy.

The Academy is governed by a Council. Various Working Committees and Task Forces are charged with developing strategies, plans and programmes in line with the Academy's objectives and functions.

The functions of the Council are:

- To formulate policy relating to the functions of the Academy
- To administer the affairs of the Academy
- To appoint such officers or servants of the Academy as are necessary for the due administration of the Academy
- To supervise and control its officers and servants
- To administer the Fund; and
- To convene general meetings of the Academy to decide on matters which under this Act are required to be decided by the Academy.

The Academy has Fellows and Honorary Fellows. The Fellows comprise Foundation Fellows and Elected Fellows. The Academy Fellows are selected from the ranks of eminent Malaysian scientists, engineers and technocrats in the fields of medical sciences, engineering sciences, biological sciences, mathematical and physical sciences, chemical sciences, information technology and science and technology development and industry.

The Future

Creativity and innovation are recognised the world over as the key measure of the competitiveness of a nation. Within the context of K-Economy and the framework of National Innovation System (NIS), ASM will continue to spearhead efforts that will take innovation and creativity to new heights in the fields of sciences, engineering and technology and work towards making Malaysia an intellectual force to be reckoned with.

Published by the Academy of Sciences Malaysia

ASM Sci. J., **2(2)**, 107–113

Tuning Range Characteristics of Linear Cavity L-band Multiwavelength Brillouin-erbium Fibre Laser

M.H. Al-Mansoori[1*], M. A. Mahdi[2], S.J. Iqbal[2] and M. K. Abdullah[2]

In this paper, the tuning range characteristics of a multiwavelength L-band Brillouin-erbium fibre laser utilizing a linear cavity is described. The dependency of the Stokes signal tuning range on the laser's pumping power and single mode fibre length is elaborated. The proposed laser configuration exhibited a wide tuning range of 11 nm from 1599 nm to 1610 nm. The maximum number of 28 output channels with a spacing of 10.5 GHz was achieved by setting the Brillouin pump wavelength and power at 1603.1 nm and 1.1 mW, respectively. The wider tuning range and higher number of Brillouin Stokes contributed to the higher efficiency of double-pass amplification in the erbium gain medium and also to the bidirectional generation of Brillouin Stokes in the single-mode fibre.

Key words: Multiwavelength fibre laser; L-band laser, optical fibre devices; non-linear-Brillouin scattering; tuning range; Stokes signal; erbium-doped fibre

Multiwavelength fibre laser sources operating on long-wavelength band (L-band) have been viewed as a natural extension of the conventional band (C-band) multiwavelength fibre laser sources for increasing the overall capacity of the dense wavelength division multiplexing (DWDM) system. Several techniques have been reported to realize multi-wavelength oscillation on L-band (1570 nm – 1610 nm) (Kim *et al*. 2001; Mao & Lit 2002). Up to seven channels with 3.2 nm spacing have been obtained on a ring cavity erbium doped fibre laser (EDFL) (Kim *et al*. 2001). A tunable Fabry-Perot etalon was used as the intracavity comb filter to achieve multiwavelength operation in L-band erbium-doped fibre (EDF) ring laser (Mao & Lit 2002). A maximum of six stable lines with a spacing of 1.3 nm in the wavelength range of 1590 nm were produced at room temperature.

Recently fibre non-linearities have been proposed as one of the various techniques to realize multi-wavelength oscillation on L-band Brillouin-erbium fibre lasers (BEFLs) utilizing the non-linear Brillouin gain and linear EDF gain in a ring cavity (Harun *et al*. 2002a; Harun & Ahmad 2002; Harun *et al*. 2002b), and in a linear cavity BEFLs (Haddud *et al*. 2005). Threshold power for the first Stokes is about 33 mW and a laser comb of up to 20 lines including the anti-Stokes has been obtained with a 10 GHz line spacing (Harun *et al*. 2002a). A dual cavity BEFL that consists of two Erbium-doped ring cavity lasers that share a length of single-mode fibre (SMF) has been reported with 10 nm tuning range and the generation of 10 lines including the anti-Stokes line (Harun & Ahmad 2002b). Up to five BEFL lines have been obtained by recycling backward the C-band amplified spontaneous emission as the secondary pump source for the unpumped EDF (Harun *et al*. 2002b). A Fabry Pérot laser cavity that used a 50 m long EDF formed by fiber loop mirrors has been reported with 24 lines of Brillouin Stokes (Haddud *et al*. 2005). Using a high threshold power of 60 mW to get the first Stokes, two 980 nm pump lasers were used to pump the EDF through two wavelength selective couplers (WSCs). That resulted an increase in the cost and maintenance of the laser source. L-band amplification in Erbium-doped fibre is conventionally lower compared to its conventional C-band amplification. Thus, the main challenge of generating cascaded Brillouin Stokes in the L-band using the nature of erbium amplification principles is to design an efficient laser resonator.

In this paper, we report a tuning range characterization of a linear cavity L-band multiwavelength BEFL source. The efficiency of generating multiple lines is attributed to the double-pass Stokes amplification in the EDF and bidirectional Stokes generation in the single mode fibre. The architecture uses a single EDF pump laser, short EDF length which exhibits a low threshold operation, a wide tuning range of about 11 nm and is able to produce up to 28 stable output channels with an equal channel spacing of 10.5 GHz.

[1] Department of Electronics and Communication Engineering, College of Engineering, University Tenaga Nasional, 43009 Kajang, selangor, Malaysia

[2] Wireless and Photonics Networks Research Center, Faculty of Engineering, Universiti Putra Malaysia, 43400 UPM Serdang, Selangor, Malaysia

[*] Corresponding author (e-mail: mansoori@ieee.org)

EXPERIMENTAL

The experimental set-up of the L-band multiwavelength Brillouin-erbium comb fibre laser is shown in Figure 1. In the scheme, the linear resonator consisted of two mirrors (M1 and M2) at both ends of the cavity, a 1480 nm-pump laser, a wavelength selective coupler (WSC) to multiplex the pump and signal lights, 12 m length of EDF and 6.7 km of SMF-28 fibre placed between a 3-dB coupler and M1 to act as the Brillouin gain medium. The EDF was characterized by 900 p.p.m. of Er^{3+}-ion concentration, an absorption coefficient of 19 dB/m at 1530 nm and a cut-off wavelength of around 1420 nm. The Brillouin pump (BP) was provided by an external-cavity tuneable laser source with a maximum power of 3.5 mW and a 100 nm tuning range from 1520 nm to 1620 nm.

The linear cavity operated as a bidirectional EDFL with oscillating modes at the EDF peak gain without BP injection. In order to create Brillouin Stokes, BP was injected through the 3-dB coupler into the SMF-28 fibre, which was down-shifted by 0.088 nm from the BP wavelength. The first-order Brillouin Stokes propagated in the opposite direction of the BP, passed into the EDF and was reinjected into the long SMF for double-pass amplification in each round trip. If the total gain generated was equal to the cavity loss, a laser oscillation formed between M1 and M2. The higher-order Brillouin Stokes signals could be generated in both directions by the lower-order Brillouin Stokes signals that travelled along SMF-28 fibre two times in a round. This cascading of Brillouin Stokes generation continued until the total gain in the laser cavity was less than the cavity loss. The output of the system was taken at the output port of the 3-dB coupler as shown in Figure 1.

RESULTS AND DISCUSSIONS

The intensity of the free-running cavity modes in the operation of Erbium-doped fiber laser is proportional to the increment of pump power into the EDF1480 nm pump laser. Figure 2 shows the free-running cavity modes at 50 mW and 100 mW of 1480 nm pump power with no injected BP power. Increasing the EDF pump power would increase the oscillating intensity of the EDFL cavity modes. The Erbium gain could be shared to have both free-running cavity modes and Brillouin Stokes co-existing at the same time. However, the free-running cavity modes could be suppressed by increasing the BP power.

BEFL tuning range is defined as the generation of Brillouin Stokes in the absence of free-running EDFL cavity modes. Figure 3 shows the tuning characteristic of the Brillouin Stokes signals without any free-running EDFL cavity modes at 3.5 mW and 50 mW of BP power and 1480 nm pump power, respectively. A tunable range of up to 11 nm with a uniform generation of up to 11-Brillouin Stokes was obtained. By tuning the BP wavelength from 1599 to 1610 nm, the Brillouin Stokes shifted simultaneously with respect to its BP wavelength.

The trend of the tuning range and the average number of output channels generated within the tuning range with 1480 nm pump power is shown in Figure 4. At a fixed BP power of 3.5 mW, the tuning range decreased as the 1480 nm pump power increased. The result obtained was very much within expectations since at a lower 1480 nm pump power, the mode competition between the EDFL cavity modes and Stokes signals could be reduced. Therefore, the system could be tuned wider if the 1480 nm pump power was

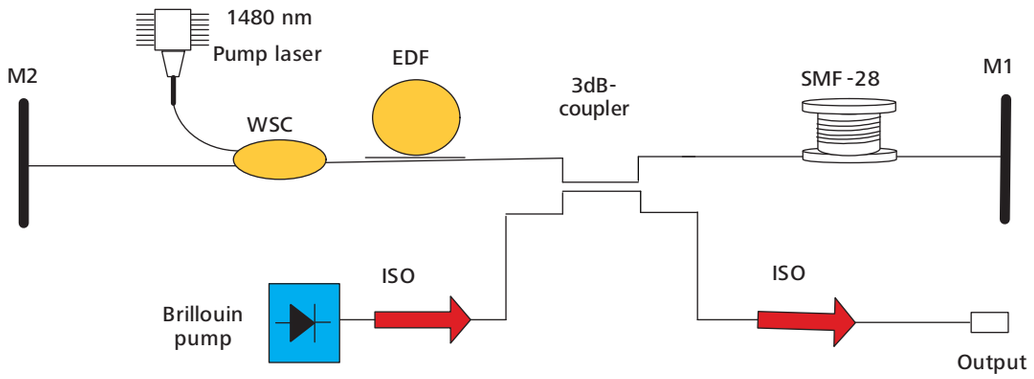

Figure 1. Experimental setup of L-band multiwavelength Brillouin-erbium comb fibre laser.

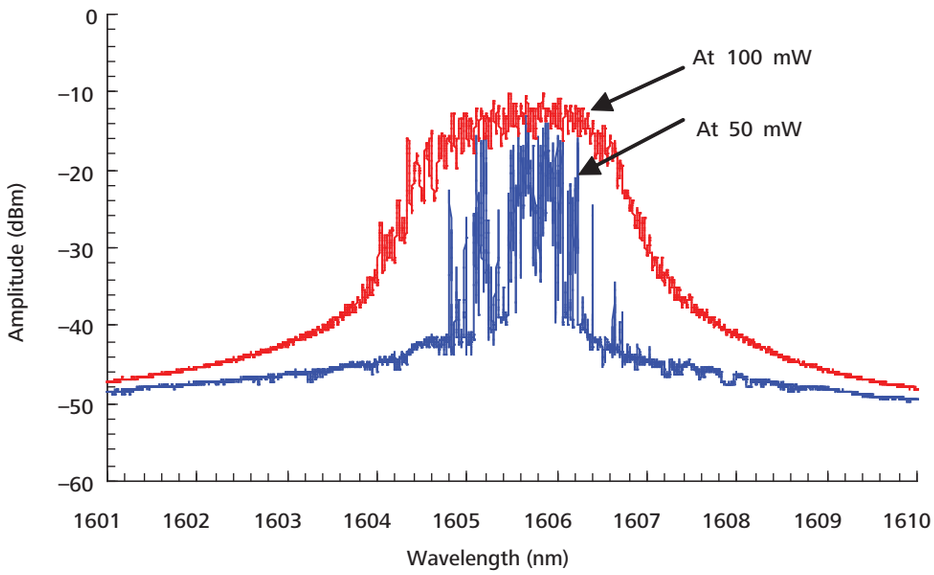

Figure 2. Free-running EDFL cavity modes at 50 mW and 100 mW of 1480 nm pump power.

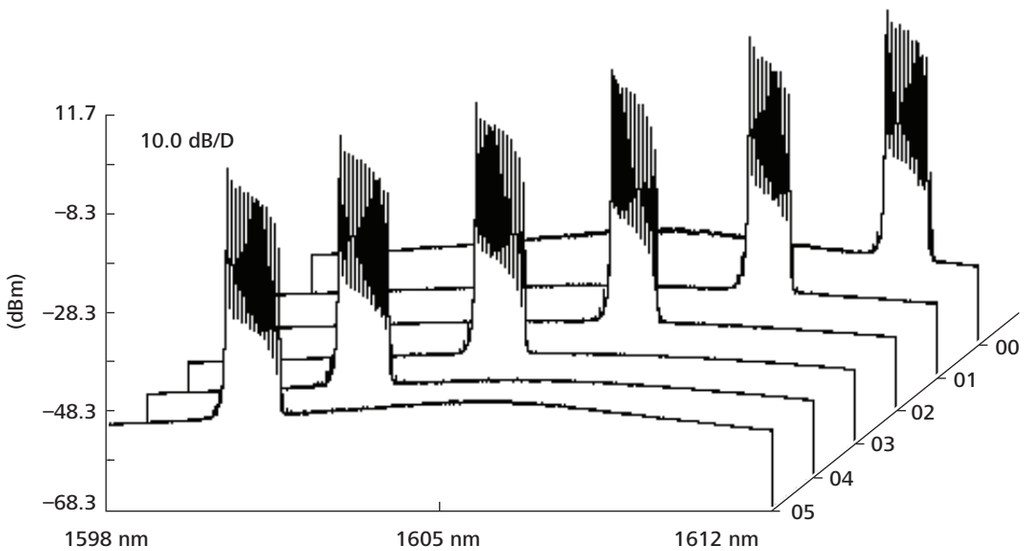

Figure 3. Tuning range characteristic of the Brillouin Stokes signals without any free-running EDFL cavity modes at 3.5 mW BP power and 1480 nm pump power set at 50 mW.

maintained low enough to reduce this mode competition. On the other hand, the average number of output channels increased as the 1480 nm pump power increased at the expense of reduction on the tuning range. As can be seen in Figure 4, at a higher 1480 nm pump power of 150 mW, an average number of 24-channel output was generated over only a 5 nm tuning range.

The wide tuning range was achieved at the expense of reduction in the number of the Stokes signals generated. This reduction in the number of Stokes signals was due to the fact that the EDF gain was not high enough to produce cascaded Stokes signals at a low 1480 nm pump power. The Erbium gain thus enabled producing a higher number of Stokes signals at the expense of the tuning range. A study on the effect of SMF length on the tuning range and the average number of output channels generated within the tuning range was also carried out for the seven different lengths of SMF. Figure 5 shows the effects of SMF length on the BEFL tuning range and the average number of output channels. The result was again obtained at 3.5 mW and 50 mW of BP and 1480 nm pump powers, respectively. As depicted in Figure 5, the tuning range and the average number of output channels increased as the SMF length increased. The higher Brillouin gain provided by longer lengths of SMF allowed the SBS to take place at a wider spectral range. In addition, shorter lengths of SMF produced smaller Brillouin gain which in turn resulted in smaller spectral range for the Stokes signal as depicted in Figure 5.

In order to optimize the operation of BEFL in producing a maximum number of Brillouin Stokes, three parameters must be adjusted: BP power; BP wavelength and a 1480 nm pump power. From previous works, the number of Brillouin Stokes can be increased by increasing the primary pump into the EDF (Harun *et al*. 2002a; Harun & Ahmad 2002; Harun *et al*. 2002b; Haddud *et al*. 2005). This was only true if the BEFL operation was within the tuning range whereby the free-running cavity modes were totally suppressed. Figure 6 elaborates the impact of the 1480 nm pump power on the number of output channels generated at different BP wavelengths. A low threshold power of 22 mW from a 1480 nm pump laser was required to get the first Stokes at 1.5 mW BP power. As shown in Figure 6, at a fixed value of BP power of 1.5 mW, an increase in the 1480 nm pump power above 100 mW resulted in reduction of the number of output channels generated. This was due to the presence of free-running cavity modes that pulled the available energy in the laser cavity into their wavelengths since their gain was higher than the BP region. In the experiment, at 100 mW of the 1480 nm pump laser, a higher number of output channels was found when the BP wavelength and power were tuned to 1603.1 nm and 1.1 mW, respectively.

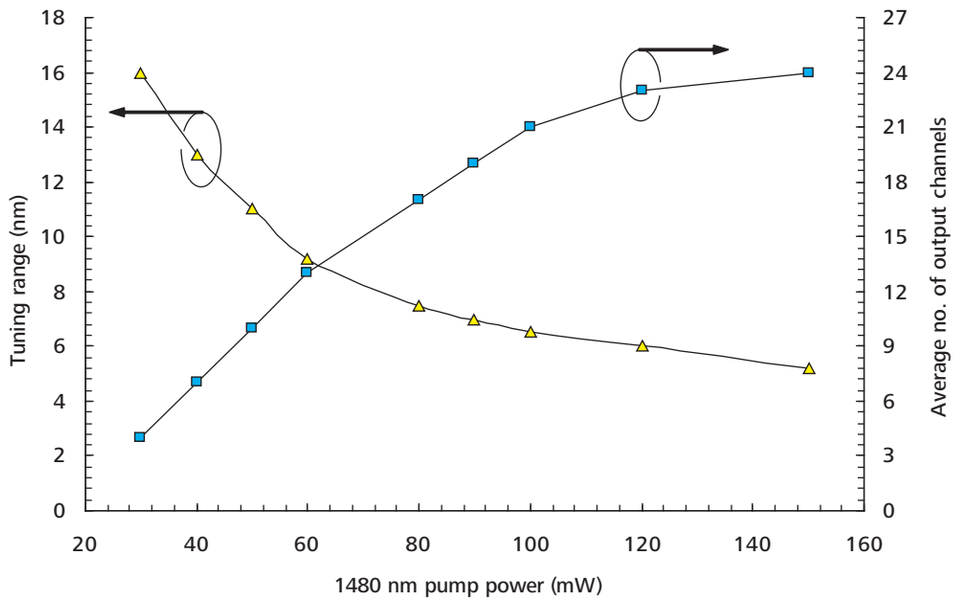

Figure 4. Tuning range and the average number of output channels generated against 1480 nm pump power at 3.5 mW BP power.

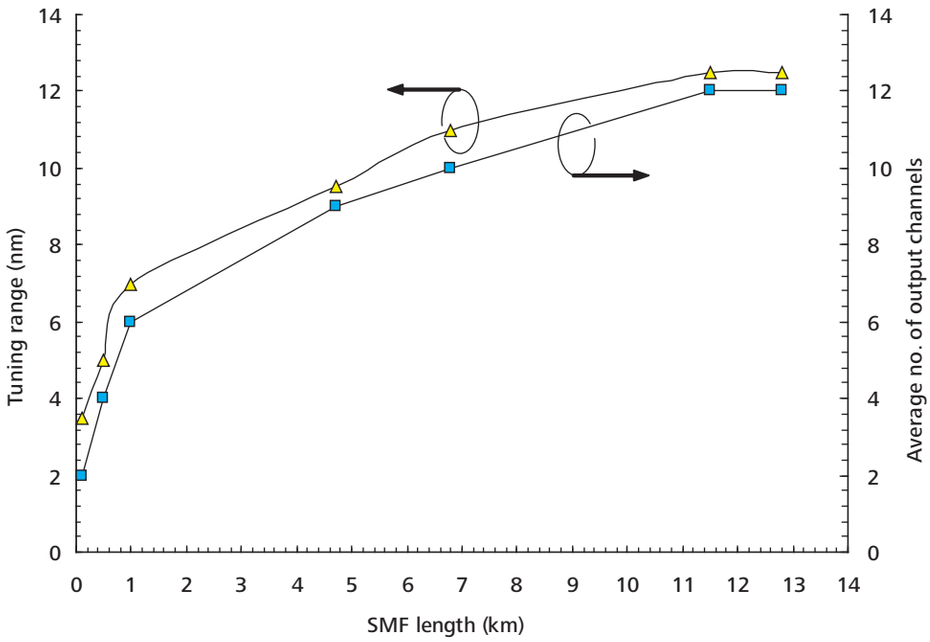

Figure 5. Tuning range and the average number of output channels generated against SMF length at 50 mW of 1480 nm pump power and BP power was set at 3.5 mW.

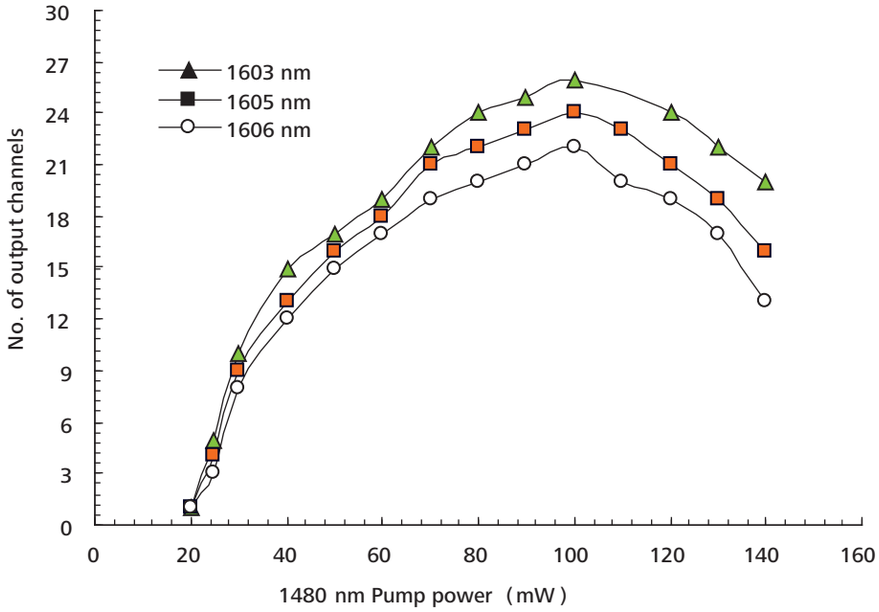

Figure 6. Number of output channels generated against 1480 nm pump power at different BP wavelengths; BP power was set at 1.5 mW.

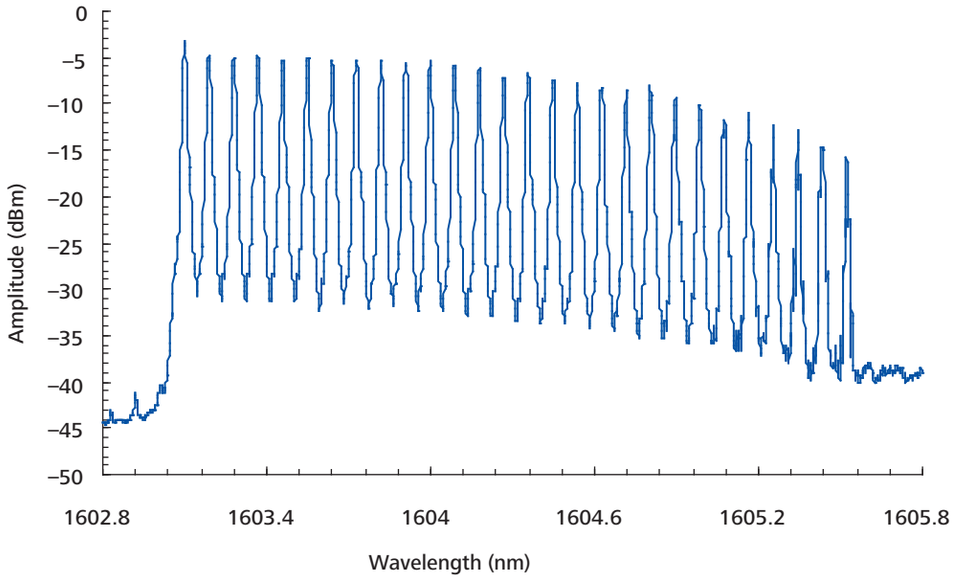

Figure 7. Output spectrum of L-band multiwavelength linear cavity BEFL at BP of 1.1 mW and 1480 nm pump power set to 100 mW.

Under this condition, the competition between free-running cavity modes and Brillouin Stokes was very high around the peak of EDF gain. Therefore, the BP power was carefully set to suppress the competition from the free-running cavity modes. At the same time, the output spectrum was observed from OSA with a resolution bandwidth of 0.015 nm. In the experiment, the optimization of the BP wavelength and power managed to produce up to 28 output channels with equal channel spacing of 10.5 GHz as depicted in Figure 7. Referring to Figure 7, the first channel represents the BP which was also circulating in the laser cavity. The total output power from this setting was 5.7 mW. The proposed linear-cavity BEFL configuration was able to produce a better result in terms of number of Brillouin Stokes as compared to the ring-cavity BEFL. Based on the findings, the efficiency of generating multiple Brillouin Stokes in the proposed linear-cavity was due to low cavity loss, double-pass amplification in Erbium-doped fibre and bidirectional generation of Brillouin Stokes in the single-mode fibre.

CONCLUSION

The tuning range of a multiwavelength L-band Brillouin-erbium comb fibre laser operating in the long-wavelength band utilizing a linear-cavity resonator was successfully demonstrated. The efficiency of the linear-cavity fibre laser was attributed to the double-pass amplification in the erbium gain medium and bidirectional Brillouin Stokes generation in the single-mode fibre. Therefore, a larger tuning range was obtained compared to the traditional ring-cavity laser configuration due to higher hybrid gain in the proposed linear-cavity. In the experiment, a tuning range of 11 nm from 1599 nm to 1610 nm with a uniform generation of up to 11 channels was measured without any free-running cavity modes. With regard to the single mode fibre lengths, it was found that at longer SMF-fibres the Stokes signal peak power was low and a wider tuning range could be achieved. Short lengths of SMF required higher laser power for a sufficient acoustic wave to be set up in the fibre to induce scattering. The maximum number of Brillouin Stokes was obtained through optimizing the operation of BEFL. A total of 28 output channels with equal channel spacing of 10.5 GHz was achieved at 1.1 mW BP power and the 1480 nm pump power was driven at 100 mW.

Date of submission: April 2008
Date of acceptance: November 2008

REFERENCES

Haddud, TA, Al-Mansoori MH, Kadir MZ, Shaharudin, S, Abdullah MK & Mahdi MA 2005, '24-line of Brillouin-erbium fiber utilizing Fabry Perot cavity in L-band', *Microwave Opt. Technol. Lett*., vol. 45, no. 2, pp. 165–167.

Harun, SW & Ahmed H 2002, 'Multiwavelength laser comb in L-band region with dual-cavity Brillouin/erbium fiber laser', *J. of Appl. Phys*., vol. 41, no. 11A, pp. 1234–1236.

Harun, SW, Tamchek N, Abd-Rahman MK, Poopalan, P & Ahmed, H 2002, 'Brillouin/Erbium-doped fiber laser with multiple wavelength generation in L-band', *IEICE Trans. Commun*., vol. E85-B, no. 7, pp. 1386–1388.

Harun, SW, Tamchek, N, Poopalan, P & Ahmed, H 2002, 'Efficient multiwavelength generation of Brillouin/erbium fiber laser at 1600-nm region', *Microw. Opt. Technol. Lett*., vol. 35, no. 6, pp. 506–508.

Kim, SK, Chu, MJ, & Lee, JH 2001, 'Wideband multiwavelength erbium-doped fiber ring laser with frequency shifted feedback', *Journal Opt. Commun*., vol. 190, pp. 291–302.

Mao, Q & Lit, JW 2002, 'L-Band multiwavelength oscillation in erbium-doped fiber ring laser', *Microwave Opt. Technol. Lett*., vol. 32, pp. 88–91.

ASM Sci. J., **2(2)**, 115–122

Variable-gain Erbium-doped Fibre Amplifier for Loss Variation Studies in a Transmission Span

M.A. Mahdi[1]*, S.J. Sheih[2], M.H. Al-Mansoori[1], A.K. Zamzuri[3] and F.R.M. Adikan[4]

A four-stage erbium-doped fibre amplifier with the gain bandwidth of 35 nm is demonstrated. The amplifier was designed to include a dispersion compensating module to compensate the accumulated dispersion by signals. The amplifier design permited some dynamic features such as the amplifier's gain could be adjusted from 15 dB to 30 dB by varying the input signal power from –26 dBm to 8 dBm. The maximum output power of 23 dBm was obtained with a maximum allowable gain flatness of 1.5 dB.

Key words: erbium-doped; optical amplifier; gain-flattening; optical fibre communication

Optical fibres, one of several kinds of transport media for telecommunication, can carry an enormous amount of information for broadband applications between widely separated transmitters and receivers. Although low transmission loss is the main advantage of optical fibres over other transport media, regeneration is still needed to compensate for transmission losses in long haul point-to-point transmission systems and for splitting losses in networking systems. The discovery of erbium-doped fibre amplifiers (EDFAs) in 1987 cultivated a new dimension of signal amplification in optical fibres. In addition to this discovery, the breakthrough research of multiple wavelength transportation riding on EDFA nurtured the most powerful technology in the history of optical fibre communications, renowned as wavelength-division multiplexed (WDM) systems.

Wideband optical amplifiers have been investigated thoroughly in order to cope with the broad bandwidth available for optical communications in the range between 1480 nm to 1620 nm. A gain equalizing filter (GEF) was used to flatten the gain ripple (flatness) of EDFA in the C-band from 1528 nm to 1563 nm (Wysocki *et al*. 1997). A gain flatness of less than 1dB was obtained using this approach. On the other hand, most published technologies used different fibre hosts of erbium-doped fibre together with GEF to obtain wide bandwidth of more than 40 nm such as tellurite-host fibre (Yamada *et al*. 1998); bismuth-host fibre (Sugimoto *et al*. 2002); phosphorous/aluminum co-doped silica-host fibre (Tanaka *et al*. 2002) and multi-component silica-host fibre (Ellison *et al*. 2001). These new materials are not ready for field deployment because of reliability. Therefore, most of the optical transmission systems were developed based on EDFA related technologies.

Besides amplification of the attenuated signals, the effect of fibre dispersion accumulated by the signals is also important. Therefore, dispersion compensation is essential for long-haul communication. One of the attractive approaches is to use a coil of dispersion compensating module (DCM). However, the DCM incurs additional losses in the transmission span. In order to reduce these losses, the DCM is utilized as a discrete Raman amplifier (Islam 2002). Nevertheless the requirement of high pump powers delays the deployment of discrete Raman amplifiers in transmission systems. In the end, the DCM must be integrated with the EDFA. This study demonstrates the design of a variable gain-flattened EDFA that has gain bandwidth of 35 nm. Its dynamic property on the input powers and operating gains creates a room of flexibility to resolve unpredictable transmission span losses. Its dynamic gain ranges from 15 dB to 30 dB with a gain flatness of less than 1.5 dB.

AMPLIFIER DESIGN CONCEPT

The specifications of the variable gain-flattened EDFA are shown in Table 1. The gain bandwidth was 35 nm from

[1] Photonics Laboratory, Department of Computer and Communication Systems Engineering, Faculty of Engineering, Universiti Putra Malaysia, 43400 UPM Serdang, Selangor, Malaysia

[2] Qyotta, 339 Bernado Ave., Suite 111, Mountain View, CA 94043, United States of America

[3] Lightwave Systems Unit, TM Research and Development Sdn Bhd, Idea Tower, Universiti Putra Malaysia, Malaysian Technology Development Corporation, 43400 Serdang, Selangor, Malaysia

[4] Department of Electrical Engineering, Faculty of Engineering, University of Malaya, 50603 Kuala Lumpur, Malaysia

* Corresponding author (e-mail: adzir@ieee.org)

1529 nm to 1564 nm. For a 100 GHz (0.8 nm) spacing, this bandwidth could accommodate up to 44 channels. However, we set 40 channels as our typical channel loading in transmission systems. This assumption was very useful in order to limit the maximum power into the mid-stage which comprised of a dispersion compensating module (DCM). A gain flatness of 1.5 dB was expected from this research work. The input power ranged from –26 dBm to 8 dBm with the maximum output power of 23 dBm. The operating gain was adjustable to between 15 dB and 30 dB. The noise figure of this variable gain-flattened EDFA was inversely proportional to the operating gain value. The expected noise figure value was divided into four bands as shown in Table 1. The minimum noise figure of 5.2 dB was set at the maximum gain of 30 dB.

The design of variable gain-flattened EDFA is depicted in Figure 1. There were four stages of optical amplifier and the loss element was placed in between the amplifier stages. The dispersion compensating module (DCM) which had a maximum loss of 10 dB was placed in between EDFA #1 and EDFA #2. Since the DCM consisted of a small core of fibre, the power of the amplified signal was set to 0 dBm/channel (40 channels, 100 GHz spacing). Therefore, the total composite output power from the first stage EDFA was set to 16 dBm. This requirement was needed to minimize the non-linear effects in the DCM that could degrade the performance of the EDFA. The second loss element deployed in the EDFA architecture was the variable optical attenuator (VOA). The VOA was utilized to change the operating gain value of the EDFA. Since the EDFA was designed to vary from 15 dB to 30 dB gain, the maximum attenuation value of 15 dB was required to achieve the design objective. The third loss element of gain equalizing filter (GEF) was placed in between EDFA #3 and EDFA #4. The GEF was designed based on the total loss of passive components used in the amplifier architecture as well as the maximum targeted gain of 30 dB. In our design estimation, the maximum loss of GEF was around 10 dB which was spectrally dependent.

Table 1. Design specification of the variable gain-flattened EDFA.

Parameter	Specification limit	Unit
Wavelength	1529 ~ 1564	nm
Input power dynamic range	–26 ~ 8	dBm
Power output	23	dBm
Gain adjustable range	15 ~ 30	dB
NF for gain = 15 dB	13.5 ~ 14.0	dB
NF for gain = 20 dB	8.5 ~ 9.0	dB
NF for gain = 25 dB	6.2 ~ 6.5	dB
NF for gain = 30 dB	5.2 ~ 5.5	dB
Overall gain flatness	1.5	dB
Power into mid-stage	16	dBm

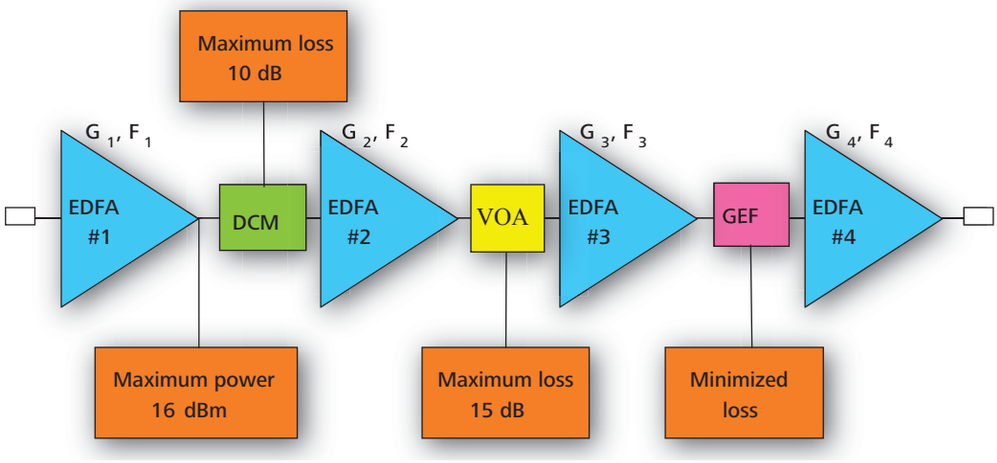

Figure 1. Block diagram of the four-stage erbium-doped fibre amplifier.

FIBRE AMPLIFIER ARCHITECTURE

The detailed architecture of the variable gain-flattened EDFA is depicted in Figure 2. In terms of pumping structure, the only limitation of the EDFA design was the number of pump lasers that could be supported by the electronic board. In our case, the number of pump lasers was limited to four units only. Thus the design of the EDFA had to take this limitation into consideration. Since the EDFA #1 had a limitation on the maximum output power, some of its pumping power could be shared with the subsequent amplifier stage. In addition, for any multi-stage amplifier design, the initial stages needed to have the characteristics of low noise and high gain. In order to achieve this, 980 nm laser diodes (LDs) were used to produce this low noise characteristic. Based on this design understanding, the 980 nm pump lasers were used to provide the energy for optical amplification from EDFA #1 to EDFA #3. In addition to this, the forward-pumped scheme was also used for all these three amplifier stages. The first 980 nm LD of 200 mW maximum powers were divided by a 3-dB coupler and injected into the EDFA #1 and the EDFA #3. The EDFA #2 was solely pumped by another 200 mW power of 980 nm LD to ensure that the signal gain was as high as possible, to minimize the loss introduced by the DCM. Finally the EDFA #4 was pumped bi-directionally by two 1480 nm LDs with 200 mW maximum output power.

In order to determine the approximate length of EDF used for the EDFA design, we performed a simulation using the VPIcomponent Maker^{TM} Fibre Amplifier simulation software. In this simulation, we used the absorption and emission coefficient values obtained directly from the manufacturer. Based on the simulation results of the amplifier design, the total length of erbium-doped fibre (EDF) was found to be around 42 m. The distribution of the EDF length for each amplifier stage is shown in Table 2. The EDF had an absorption coefficient of 5.9 dB/m at 1530 nm, a cutoff wavelength of 910 nm and a numerical aperture of 0.22.

Lastly, the GEF characteristic is shown in Figure 3. The targeted GEF-shape was obtained from the simulation results, while the measured GEF-shape was obtained from the experimental results. We used a long-period fibre Bragg grating as the GEF. The fabricated GEF had good agreement with the desired GEF and the error was close to 1 dB at 1534 nm and 1539 nm. The GEF curve was not smooth in between 1552 nm and 1561 nm.

RESULTS AND DISCUSSIONS

The measurements of gain and noise figures were performed using the optical spectrum analyzer. In order to measure the gain flatness of the developed EDFA, 40 channels were deployed simultaneously from 1530.33 nm to 1561.42 nm. The input signal powers were set at –7 dBm, –2 dBm, 3 dBm and 8 dBm for gains of 30 dB, 25 dB, 20 dB and 15 dB, respectively. The total output power was fixed at 23 dBm for all signal powers. The pump powers of 980 nm and 1480 nm LDs were varied accordingly to achieve the desired output power of 23 dBm. The experimental results are shown in Figure 4(a). For an operating gain of 30 dB, the VOA was set at 0 dB. For other gain values, the VOA was set accordingly in order to maintain gain flatness. For example, the VOA was set at 10 dB for an operating gain of 20 dB.

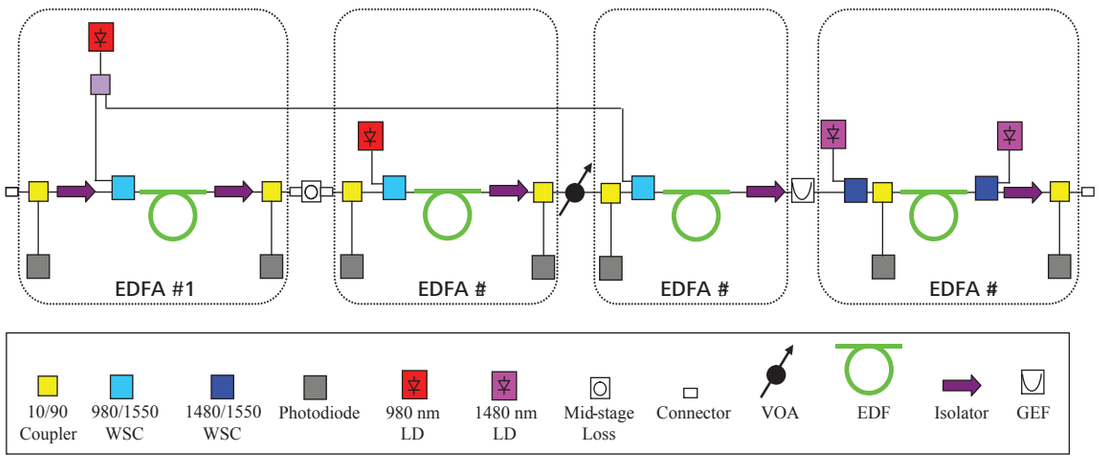

Figure 2. Architecture of a variable gain-flattened EDFA that consists of four stages of optical amplification, the mid-stage is used to insert a DCM to compensate the accumulated dispersion by the signals.

Table 2. EDF length distribution of the variable gain-flattened EDFA.

	EDFA #1	EDFA #2	EDFA #3	EDFA #4	Unit
Length	7	9	7	19	m

Based on the findings, the total pump powers for the EDFA #4 were adequate to achieve the 23-dBm output power. The available pump power for the EDFA #4 was 400 mW from two 1480 nm LDs. The output spectrum of the variable gain-flattened EDFA is depicted in Figure 4(b). The operating gain was 30 dB and the input power was set at –7 dBm. The floor spectrum was flat until 1566 nm to indicate that the developed EDFA could cover up to 37 nm, 2 nm more than the design target of 35 nm.

In order to measure gain flatness, all the gain values were normalized as illustrated in Figure 4(c). The best gain flatness of about 1.2 dB was obtained for the operating gain of 30 dB. As the operating gain reduced (signal power increased), the gain flatness degraded from 1.2 dB to 1.7 dB. Our target specification showed that this value was less than 1.5 dB. The reason that the gain flatness could not be maintained was due to the effect of spectral hole burning (SHB) (Desurvire *et al*.1990; Bolshtyansky 2003). Thus the short wavelengths around 1530 nm at high signal power had higher powers. To overcome this problem, the GEF was modified to balance up the impact of SHB in low and high signal powers. Based on the normalized gain curve, the GEF curve was modified by increasing the loss for the short wavelengths. Then the new GEF shape was used in the same experiment again.

The measured results for the operating gains of 15 dB and 30 dB are shown in Figure 5(a) and Figure 5(b), respectively. Based on the findings, the gain flatness was improved from 1.7 dB to 0.9 dB for an operating gain of 15 dB. It could be seen that the gain shape for the operating gain of 30 dB was inverted from its original shape.

This was due to the fact that more losses were introduced in this wavelength range. The gain flatness performance degraded from 0.6 dB to 0.7 dB. However, the new gain flatness was still lower than the target value of 1.5 dB. The gain flatness degradation was expected for the large operating gains in order to compensate the poor gain flatness at small operating gains. The noise figure was also measured at different gain levels as shown in Figure 6. The maximum noise figures were 5.8 dB, 7.2 dB, 10 dB and 15.4 dB for the 30-dB, 25-dB, 20-dB and 15-dB operating gains, respectively. In this work, all the noise figure values were larger than the specifications limit.

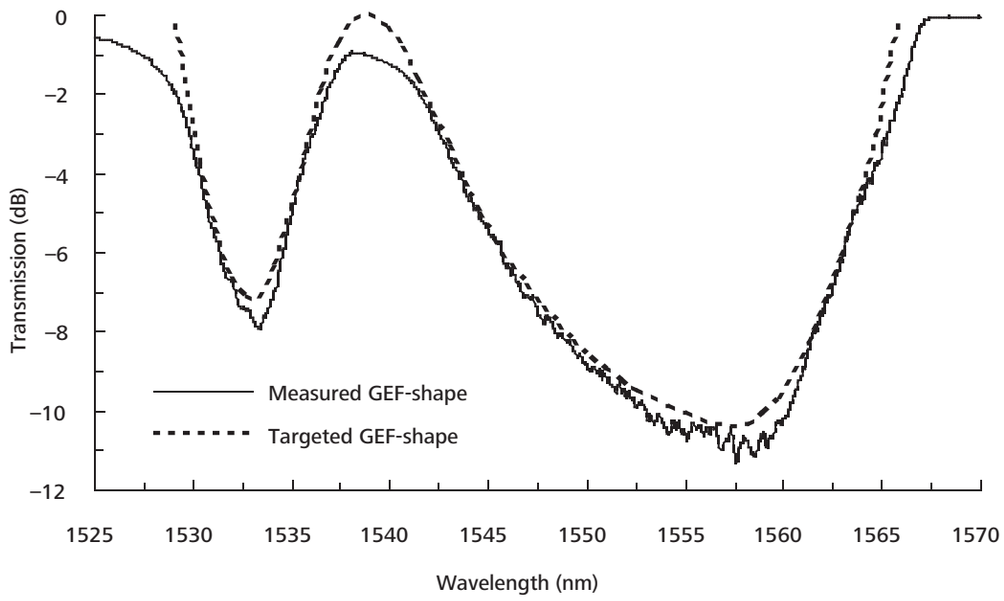

Figure 3. GEF transmission spectrum of the developed four-stage EDFA.

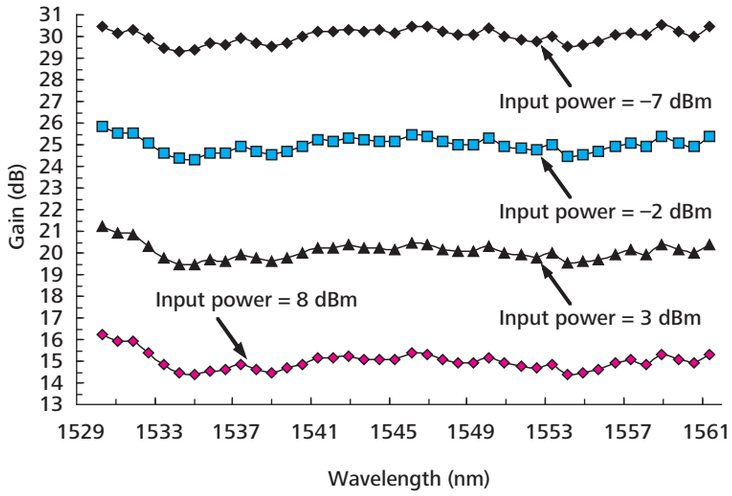

(a)

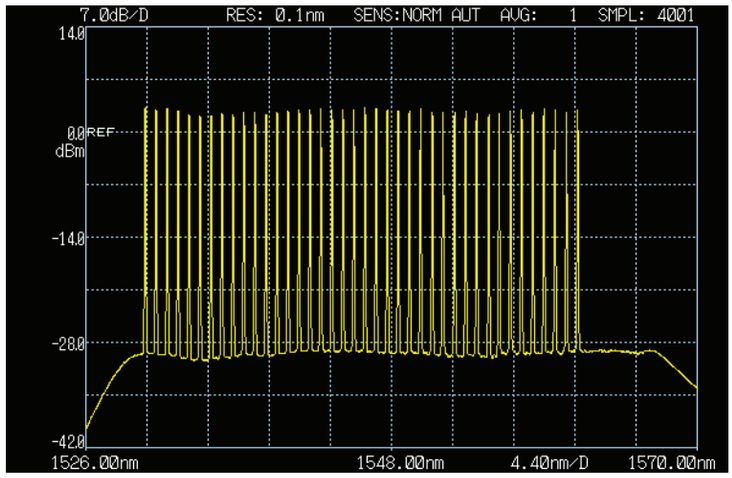

(b)

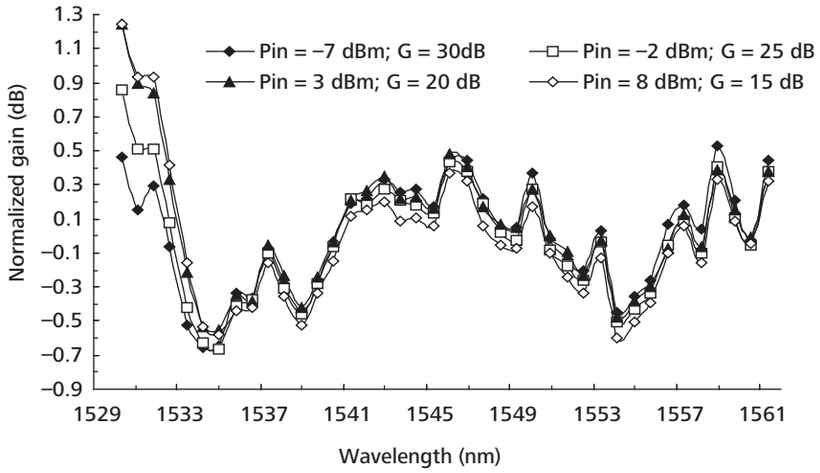

(c)

Figure 4. Experimental results of the variable gain-flattened EDFA: (a) various operating gains; (b) output spectrum of the 30-dB operating gain and (c) the normalized gain at different operating gains.

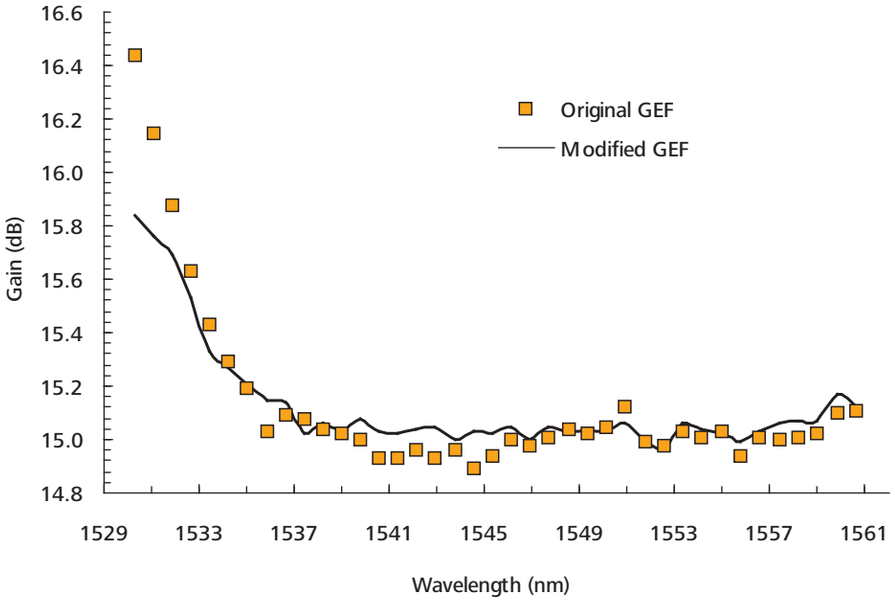

(a)

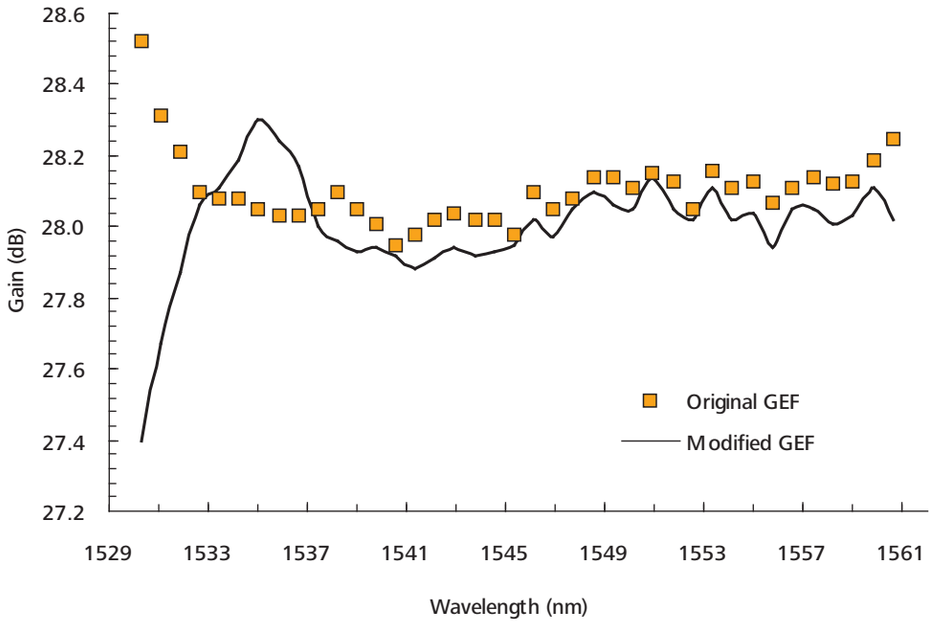

(b)

Figure 5. Comparison of gain flatness between original GEF and the modified GEF at the operating gain of (a) 15 dB and (b) 30 dB.

Several factors have been identified as contributors to the higher noise figures. These are (a) the first stage design was not completely optimized and gain at longer wavelengths could be increased to reduce the noise figures; (b) the input isolator was a double-stage type that had higher insertion loss compared to a single-stage type isolator. However, this component was critical to minimize the effect of backward amplified spontaneous emission when it propagated back into the system at the input port; (c) the third stage amplifier was inefficient due to large signal powers at the input point that could cause saturation. Therefore, higher pump power was required to increase gain and thus minimize noise figures. It was also possible to interchange the pumping scheme between EDFA #2 and EDFA #3; and (d) the use of couplers for each input and output port of the amplifier introduced losses in the amplifier systems. However, this condition was important to monitor the condition between amplifier stages for automatic detection in the future.

The most important criteria to obtain a low noise figure was to control the insertion loss of each component used in the amplifier architecture. Another approach to solve this problem was to use integrated components that could package multiple components in a single enclosure. It was expected that insertion loss could be reduced with this technology advancement.

CONCLUSION

The variable gain-flattened EDFA with 35 nm bandwidth was successfully demonstrated. The design of EDFA consisted of four amplifier stages. The first three stages were pumped by 980 nm pump lasers in forward-pumping configuration to get low noise figures. The final amplifier stage was pumped bi-directionally by two 1480 nm pump lasers to achieve high output power of 23 dBm. The EDFA was designed to incorporate a DCM for long-haul applications. The gain-flatness of less than 1.5 dB was maintained over a 15 dB dynamic gain range. The gain ranged from 15 dB to 30 dB when the input power varied from –26 to 8 dBm. The effect of SHB was minimized by adjusting the shape of the GEF to increase attenuation in short wavelengths, around 1529 nm. The measured noise figure was slightly higher than the desired ones due to high insertion losses from the passive components. The wide range of input powers and operating gains provided a flexibility of operators for deployment in transmission systems in which most of the requirements were unique. The study showed that the amplifier could be designed as the universal subsystem in order to increase manufacturing capability.

Date of submission: April 2008
Date of acceptance: November 2008

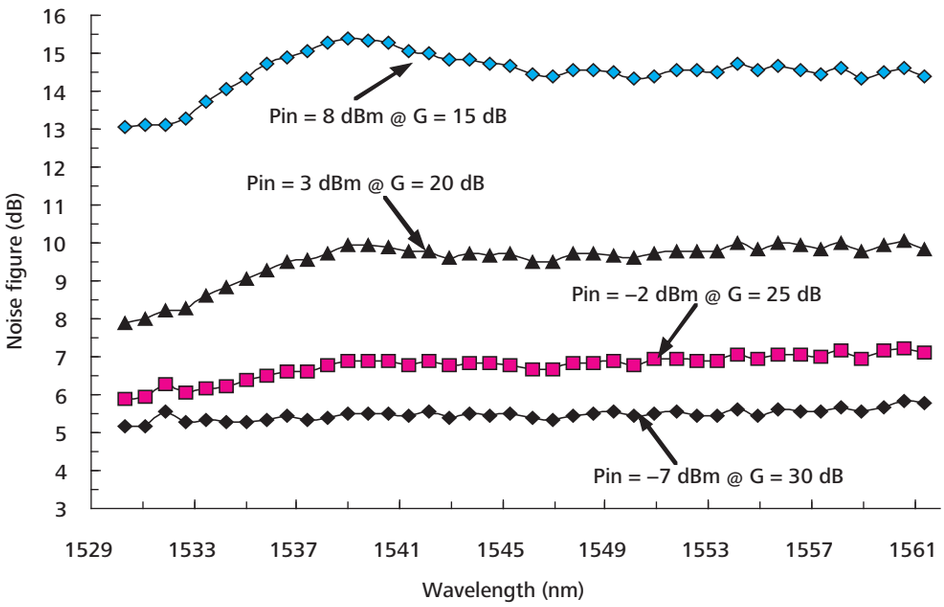

Figure 6. Noise figure against signal wavelength at different operating gains: 15-dB; 20-dB; 25-dB and 30-dB.

REFERENCES

Bolshtyansky, M 2003, 'Spectral hole burning in erbium-doped fibre amplifiers', *Journal of Lightwave Technology*, vol. 21, no. 4, pp. 1032–1038.

Desurvire, E, Sulhov, JW, Zyskind, JL & Simpson, JR 1990, 'Study of spectral dependance of gain saturation and effect of inhomogeneous broadening in erbium-doped aluminosilicate fibre amplifiers', *IEEE Photonics Technology Letters*, vol. 2, pp. 653–655.

Ellison, AJG, Goforth, DE, Samson, BN, Minelly, JD, Trentelman, JP, McEnroe, DL & Tyndell, BP 2001, 'Extending the L-band to 1620 nm using MCS fibre', in *Proceedings of Optical Fiber Communication*, paper TuA3.

Islam, MN 2002, 'Raman amplifiers for telecommunications', *IEEE Journal of Selected Topics in Quantum Electronics*, vol. 8, no. 3, pp. 548–559.

Sugimoto, N, Ochiai, K, Ohara, S, Hayashi, H, Fukusawa, Y, Hirose, T & Reyes, M 2002, 'Highly efficient and short length Lanthanum co-doped Bi_2O_3-based EDF for extended L-band amplification', in *Proceeding of Optical Amplifiers and their Applications*, PD5-1~PD5-3.

Tanaka, S, Imai, K, Yazaki, T & Tanaka, H 2002, 'Ultra-wideband L-band EDFA using phosphorus co-doped silica-fibre', in *Proceedings of Optical Fiber Communication*, pp. 458–459.

Wysocki, PF, Judkins, J, Espindola R, Andrejco, M, Vengsarkar A & Walker, K 1997, 'Broad-band erbium-doped fibre amplifier flattened beyond 40 nm using long-period grating', *IEEE Photonics Technology Letters*, vol. 9, no. 10, pp. 1343–1345.

Yamada, M, Mori, A, Kobayashi, K, Ono, H, Kanamori, T, Oikawa, K, Nishida, Y & Ohishi, Y 1998, 'Gain-flattened tellurite-based EDFA with a flat amplification bandwidth of 76 nm', *IEEE Photonics Technology Letters*, vol. 10, no. 9, pp. 1244–1246.

ASM Sci. J., **2(2)**, 123–127

Wideband Double-pass Discrete Raman Amplifier with Pump Reflector

M.A. Mahdi[1]*, M.I. Md. Ali[2], A. Ahmad[2] and A.K. Zamzuri[2]

In this paper a study on the wideband double-pass Raman fibre amplifier with mirror as the pump reflector is reported. The pump lights at 1435 nm and 1455 nm were launched in a co-directional manner with respect to the input signal. The double-pass direction of the signal was achieved through a fibre loop mirror constructed using an optical circulator. It was shown that multiple signal amplification was achieved without any disturbance of stimulated Brillouin scattering.

Key words: discrete Raman amplifier; double-pass; fibre Bragg grating; wideband; pump reflector; fibre loop mirror; Brillouin scattering

Optical fibre amplifiers have transformed telecommunication systems especially in the long-haul communication arena. The advent of Erbium-doped fibre amplifiers in 1989 has stimulated research activities in this area with a transformation from single channel amplification to that of multiple channel amplification. The technical challenge of multiple channel amplification is to have a wide bandwidth amplifier. The amplification bandwidth of Erbium-doped fibre amplifiers can be extended from 35 nm (Wysocki *et. al*. 1997) to 80 nm (Sun *et. al*. 1997) by combining the C-band and L-band in the amplifier structure. However, the amplification bandwidth of the Erbium-doped fibre amplifier is limited by the Erbium's energy transition.

On the other hand, an alternative technique of optical amplification relies on the non-linear effect in optical fibre known as stimulated Raman scattering. Raman amplification occurs due to the transition between vibrational modes in the transmission fibre medium (Agrawal 2006). Since the process of Raman amplification does not depend on the energy transitions of the active materials, the amplification can take place at any wavelength. This feature is very attractive as the amplification bandwidth can be easily tailored by the proper arrangement of the pump wavelength. A bandwidth of 100 nm has been reported using standard single-mode fibres (Emori & Namiki 1999). Despite this significant advantage, Raman amplification has a low power of conversion efficiency. Therefore Raman fibre amplifiers must be designed to incorporate higher gain efficiency to be able to compete with the Erbium-doped fibre amplifier. Double-pass discrete Raman amplifier (DRA) has been reported recently to rectify the problem (Tang & Shum 2003). The double-pass DRA structure is designed by placing a broadband reflector at the other end of the dispersion compensating fibre (DCF). Besides reflecting the signals, the broadband reflector is also utilized to reflect the pump light which improves the Raman gain as well (Nicholson 2003). Gain improvement is recorded for this double-pass DRA structure. Nevertheless the amplifier structure suffers poor noise figure for large signals due to multi-path interference (Tang *et. al*. 2004). In order to mitigate this problem, a gain-clamped technique is proposed which limits the amplification to a lower value (Tang *et. al*. 2004). However, this approach is unfavorable because the double-pass DRA is pushed to operate at its lower capability.

We have investigated the issue of poor noise figures for large signals and discovered that the noise figure degradation was caused by stimulated Brillouin scattering rather than multi-path interference (Md. Ali *et. al*. 2006). This issue was only applicable if the signal power used for the amplification was too large. In practice, the DRA was utilized to amplify multiple signals simultaneously, therefore the intensity of the signal was greatly reduced. Thus, the generation of stimulated Brillouin scattering was almost eliminated under the environment of multiple channels.

In this paper, we demonstrate optical amplification of 16 channels using a double-pass Raman fibre amplifier (RFA). The proposed double-pass discrete RFA was constructed together with a mirror as the pump reflector.

[1] Wireless and Photonics Networks Research Center, Faculty of Engineering, Universiti Putra Malaysia, 43400 UPM Serdang, Selangor, Malaysia.
[2] Lightwave Systems Unit, TM Research & Development Sendirian Berhad, Idea Tower, Universiti Putra Malaysia-Malaysian Technology Development Corporation, 43400 Serdang, Selangor, Malaysia.
* Corresponding author (e-mail: adzir@ieee.org)

CHARACTERIZATION OF DOUBLE-PASS DISCRETE RAMAN AMPLIFIER

The proposed configuration of the double-pass DRA is depicted in Figure 1 (in dashed-box). The Raman gain was provided by the 3-km DCF forward-pumped by high-power grating stabilized Raman pump unit (RPU) at 1435 nm. The DCF loss of 2.9 dB was measured at 1530 nm. The total dispersion compensation value was –360 ps/nm designed to compensate accumulated dispersion for 80 km TrueWave® transmission fibre. The input signal of 1530 nm was obtained from the tunable laser source (TLS). The level of the signal was varied by changing the value of the variable optical attenuator (VOA).

In order to enhance the Raman gain efficiency, a FBG with > 99% reflectivity at 1435 nm was inserted at the fibre end of the wavelength selective coupler-2 (WSC2). The residual pump power, after travelling in the gain medium of DCF was reflected by high reflectivity FBG and travelled back into the DCF. In the continuous mode, the signal would experience bi-directional pumping in the 3-km DCF, without using an additional pump. The double-pass amplification was established by using a fibre loop mirror constructed by looping back the second optical circulator (OC2). The output signal was taken at port 3 of the first optical circulator (OC1) and measured using the optical spectrum analyzer (OSA). The proposed double-pass DRA architecture could be easily transformed to a single-pass DRA by disconnecting point A as shown in Figure 1.

The gain performance of double pass DRA in comparison with a typical single pass system was studied. In Figure 2, Raman net gains for single-pass and double-pass DRAs were plotted with the same 3-km DCF. The input signal was maintained at –25 dBm at 1530 nm, 10 Gbps NRZ-modulated source. More than 20 dB gain was achieved with these designs at a small signal condition when the injected pump powers were 740 mW and 410 mW for single-pass and double-pass DRAs, respectively. This showed that only 55% pump power was required for the double-pass DRA to achieve the same gain value of the single-pass DRA. The maximum gain of 21 dB was obtained at 422 mW pump power for the double-pass DRA. We also defined gain slope efficiency as the increment of gain over the increment of pump power. In this experiment, the gain slope efficiency values for single-pass and double-pass DRAs were 0.033 dB/mW and 0.069 dB/mW, respectively. These values were higher than those values obtained from the previous report in which the pump laser was launched co-propagating with the signal (Tang *et al*. 2004). The counter-propagating pump scheme exhibited a better performance due to a better pump distribution along the DCF.

The noise figure (NF) performance as a function of injected pump power for single-pass and double-pass DRAs is depicted in Figure 3. In this experiment, the input signal power was fixed at –25 dBm and wavelength at 1530 nm. When both DRA designs were unpumped, the total NF was equal to the total loss experienced by the signal. In this case, it was clearly shown that the double-pass DRA produced higher NF because the signal propagated twice in the design and accumulated more losses compared to the single-pass DRA. However, the NF was improved as the pump power was increased for the double-pass DRA. Towards the end, the NF for double-pass DRA was maintained at less than 5 dB. Even though the total gain was higher than the single-pass DRA for pump power greater than 83 mW, as shown in Figure 2, the total NF was still higher than the single-pass DRA. In order to populate pump light along the DCF in the double-pass configuration, higher pump powers were required due to the bidirectional amplification of the signal. This condition created high amplification rate at the end of the DCF (close to WSC2) and pump depletion was expected to occur in this region. Therefore, the input section of the DCF (close to WSC1)

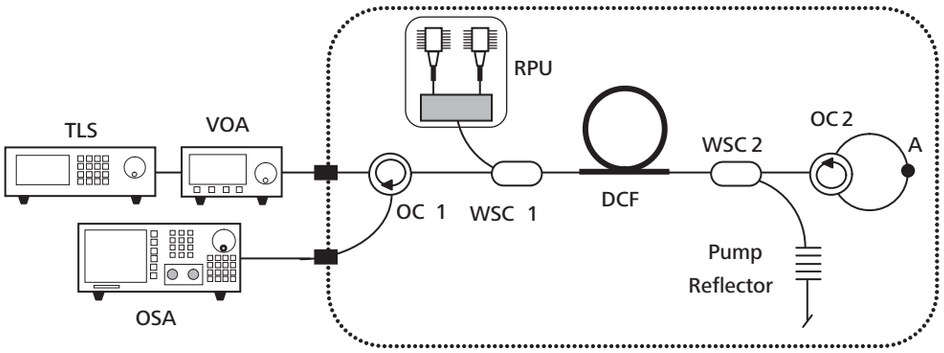

Figure 1. Configuration of double-pass discrete Raman amplifier with pump reflector and fibre loop mirror.

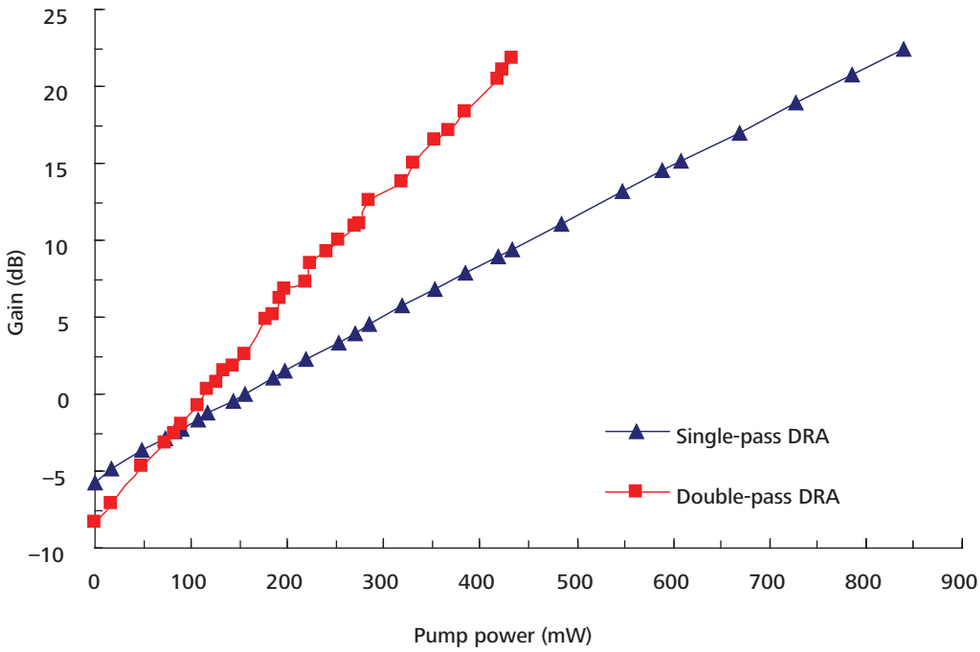

Figure 2. Raman gain comparison for single-pass and double-pass DRAs at input signal power and wavelength of −25 dBm and 1530 nm, respectively.

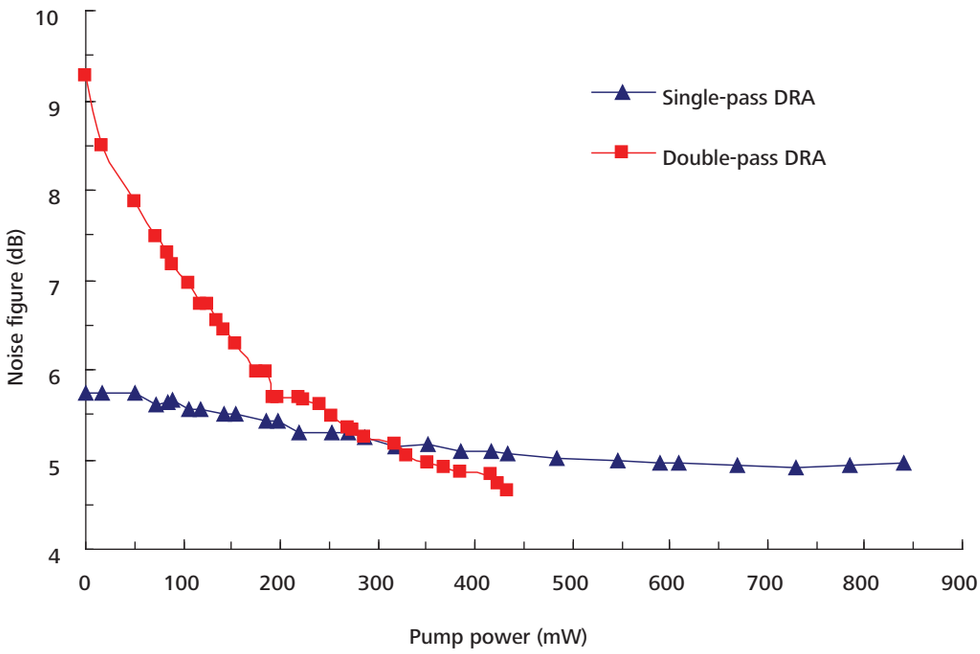

Figure 3. Experimental NF versus input pumping power for single-pass and double-pass DRAs at input signal power and wavelength of −25 dBm and 1530 nm, respectively.

became lossy in the under-pumped condition whereby the signal experienced a net loss instead of gain. The impact of Rayleigh backscattering is quite small due to the short length of fibre and low signal power (Tang *et al*. 2004). We observed that the measurement of NF was not impacted by multi-path interference (MPI) noise for low signal powers. Therefore, the proposed double-pass DRA architecture was suitable to be deployed as a pre-amplifier whereby the noise accumulation at the signal was not influenced by the MPI noise.

Another important factor that needs to be taken into account is the noise attributed by the pump-signal relative intensity noise (RIN) transfer. Since the FBG was used as the pump reflector, the residual pump travelled in the same direction as the input signal, thus this factor should be investigated (Wysocki *et al*. 1997). In order to verify the influence of the pump-signal RIN transfer, we studied the performance comparison between double-pass DRA with and without FBG, as depicted in Figure 4.

WIDEBAND DOUBLE-PASS DICRETE RAMAN AMPLIFIER

From the previous section, it is clearly shown that the double-pass DRA was efficient in terms of amplifying signal. The same gain value was achieved at a lower pump power in which the gain efficiency was increased. Since the configuration of the double-pass DRA utilized single-pump wavelength, the amplification bandwidth was limited at the peak wavelength of around 1530 nm and it was difficult to achieve a flat gain. In order to cover the whole C-band for a wider bandwidth, the double-pass DRA could be re-designed by deploying another set of Raman pump unit (RPU) at 1455 nm as depicted in Figure 4.

Since two pump wavelengths were used in the amplifier, the pump reflector was formed by replacing the FBG with a broadband reflector. Two pump wavelengths at 1435 nm and 1455 nm were multiplexed via a pump combiner (PC). For this experiment, the maximum pump power for the 1455 nm was only 340 mW.

To study further on the effect of multi-channel on double-pass DRA, experimental investigation was performed using a 16-channel input. The 16-channel input was selected within 1544.7 nm to 1561.3 nm with 100 GHz spacing between each adjacent channel. All the channels were multiplexed using a fused-coupler-based multiplexer. In this experiment, the pump power was set at 420 mW and 340 mW for 1435 nm and 1455 nm, respectively. The latter was set at a lower value due to the restriction of output power from the laser diode. The optical spectrum was measured using 0.2 nm OSA resolution. The input of each channel was fixed at –12 dBm, thus the total output of all channels equaled 0 dBm. The input and output spectra are depicted in Figure 5.

From the experiment, the output spectrum was flat from 1545.7 nm to 1561.3 nm. The measured gain value was maintained at 9.7 dB with variation of less than 0.5 dB for all channels. The presence of stimulated Brillouin scattering was not observed in this experiment. Thus, we have demonstrated experimentally that the double-pass DRA could amplify multiple channels simultaneously with an almost negligible effect of stimulated Brillouin scattering. This experiment showed that the double-pass DRA was a potential candidate for wavelength division multiplexed systems. The advantage of utilizing DCF as the amplifying medium could benefit as it concurrently compensated the effect of fibre dispersion.

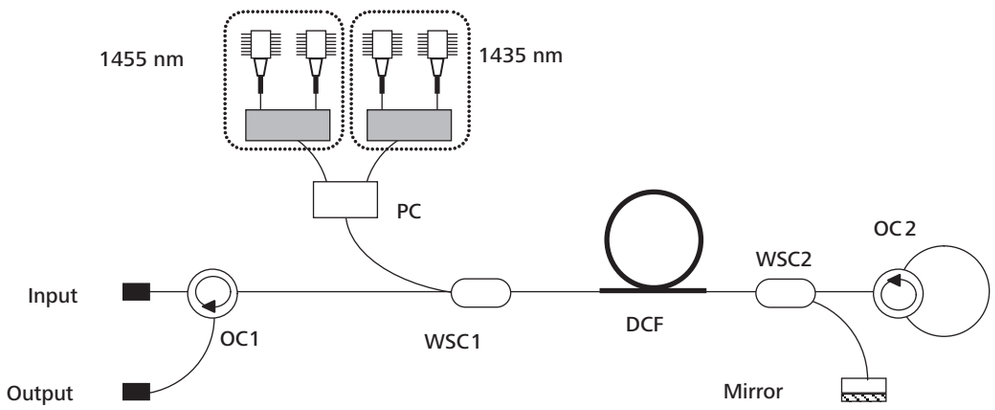

Figure 4. Configuration of wideband double-pass DRA with a mirror as the pump reflector.

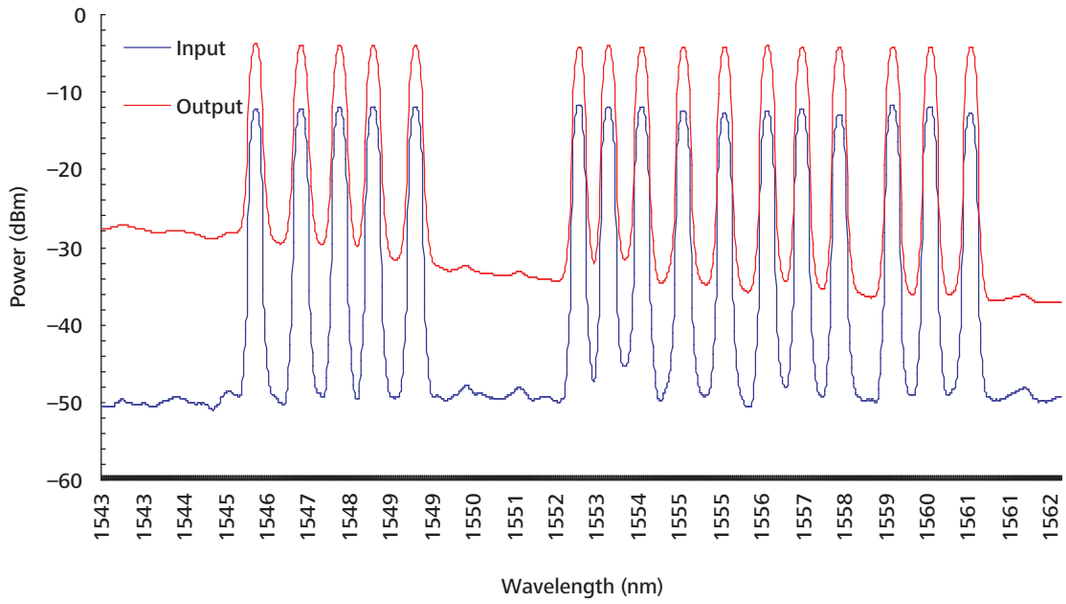

Figure 5. Spectra of 16 channels, input and output signals from the wideband double-pass DRA.

CONCLUSION

A wideband double-pass discrete Raman amplifier has been successfully demonstrated. Dual pump wavelengths at 1435 nm and 1455 nm were utilized to provide wideband amplification. The amplifier structure consisted of a pump reflector formed by a mirror to reflect the remaining pump wavelengths at the end of the dispersion compensating fibre. The double-pass amplification of the signal was achieved by looping back the signal into the amplifying medium via a fibre loop mirror. Sixteen channels were successfully amplified from 1545.7 nm to 1561.3 nm without any presence of stimulated Brillouin scattering. The proposed double-pass amplifier has great potential to complement the Erbium-doped fibre amplifier in WDM systems.

Date of receipt: April 2008
Date of acceptance: November 2008

REFERENCES

Agrawal, GP, *Nonlinear fiber optics*, 4th edn, Academic Press, New York, 2006.

Emori, Y & Namiki, S 1999 '100 nm bandwidth flat gain Raman amplifiers pumped and gain-equalized by 12-wavelength-channel WDM high power laser unit', *Electronics Letters*, vol. 35, no. 16, pp. 1355–1356.

Md. Ali, MI, Zamzuri, AK, Ahmad, A, Mohamad R & Mahdi, MA 2006 'Experimental validation of double-pass discrete Raman amplifier limitation for large signals,' *IEEE Photonics Technology Letters*, vol. 18, no. 3, pp. 493–495.

Nicholson, JW 2003 'Dispersion compensating Raman amplifiers with pump reflectors for increased efficiency', *IEEE Journal of Lightwave Technology*, vol. 21, no. 8, pp. 1758–1762.

Sun, Y, Sulhoff, JW, Srivastava, AK, Zyskind, JL, Strasser, TA, Pedrazzani, JR, Wolf, C, Zhou, J, Judkins, JB, Espindola, RP & Vengsarkar, AM 1997, '80 nm ultra-wideband erbium-doped silica fibre amplifier', *Electronics Letters*, vol. 33, no. 23, pp. 1965–1967.

Tang, M & Shum, P 2003 'Design of double-pass discrete Raman amplifier and the impairments induced by Rayleigh backscattering,' *Optics Express*, vol. 11, no. 16, pp. 1887–1893.

Tang, M, Gong, YD & Shum, P 2004 'Dynamic properties of double-pass discrete Raman amplifier with FBG-based all-optical gain clamping techniques,' *IEEE Photonics Technology Letters*, vol. 16, no. 3, pp. 768–770.

Wysocki, PF, Judkins, J, Espindola, R, Andrejco, M, Vengsarkar, A & Walker, K 1997 'Broad-band erbium-doped fiber amplifier flattened beyond 40 nm using long-period grating', *IEEE Photonics Technolology Letters*, vol. 9, no. 10, pp. 1343–1345.

ASM Sci. J., **2(2)**, 129–132

Theoretical Analysis and Optimization of Chromatic Dispersion Measurement Using the Technique of Relative Power of Two Beating Frequencies

H.A. Abdul-Rashid[1*], M.T. Al-Qdah[1], H.T. Chuah[1] and M. Tayahi[2]

The operating principle and the performance of chromatic dispersion (CD) measurement technique are discussed through developed numerical models. The performance of the CD measurement technique was studied in terms of the measurement range and sensitivity as the wavelength separation was varied. Based on the numerical model, the technique sensitivity increased with wavelength separation. However, this increase in sensitivity was traded off with a narrower measurement range. The measurement technique was optimized at 5.0 GHz wavelength separation with a sensitivity of 0.009 (dB/ps/nm) and measurement range of 2500 ps/nm.

Key words: chromatic dispersion; measurement technique; wavelength separation; relative power; beating frequencies; numerical model; optimization parameters; four-wave mixing

Chromatic dispersion (CD) is based on the fact that different spectral components of an optical signal travels down the fibre at different speeds. In high-speed optical communication systems, the small tolerance to CD is one of the most crucial considerations. Network operators would like to have tunable, drop-in CD compensators that depend on reliable CD measurement technique. Other CD measurement techniques include measuring the phase delay between the upper sideband and the lower sideband of an out-of-band subcarrier tone (Petersen *et al*. 2002), measuring the magnitude of amplitude modulation (AM) component converted from phase modulated pilot tones (Park *et al*. 2000) and employing non-linear optical detection (Wielandy *et al*. 2003). These techniques either suffer from high complexity or being limited to single wavelength channel.

This paper proposed a chromatic dispersion measurement using the relative power of two beating frequencies (Al-Qdah *et al*. 2005). The measurement was made by launching two optical signals pump and probe with a radial frequency separation of ω_1 into a spool of fibre through a phase conjugator. The semi-conductor optical amplifier (SOA) which was used as an optical phase conjugator, produced another two phase conjugated signals as a result of four-wave mixing (FWM). The relative power between the beating signals at frequencies ω_1 and $2\omega_1$, the main beating and FWM beating were used to determine the accumulated CD in the fibre.

The CD measurement technique using two beating frequencies was then optimized for the sensitivity and measurement range against wavelength separation. It was found that the sensitivity of the technique increased with wavelength separation. However, this increase in sensitivity was traded off with a shorter measurement range. Based on the measurements made, the CD measurement technique could be optimized at 5.0 GHz wavelength separation with a sensitivity of 0.009 (dB/ps/nm) and measurement range of 2500 (ps/nm). The next section deliberates on the numerical model of the CD measurement technique and the optimization of the sensitivity and measurement range. The numerical model results were also presented and analyzed.

NUMERICAL MODEL

The proposed CD measurement technique is shown in Figure 1. The optical phase conjugation was achieved using an SOA. The phase conjugator inverted the phase of the probe signal $E_{probe}(z,t)$ and translated it to the FWM conjugated signal $E_{FWM}(z,t)$. The same translation and phase conjugation happens to the pair $E_{pump}(z,t)$ and $E_{FWM2}(z,t)$. The photodetector converted the combined electric field $E_{total}(z,t)$ into photocurrent $I(t)$.

In Equation 1, the attenuation factor was ignored since it was a common factor for all the terms and the terms

[1] Center for Photonics, Research, Innovation and Applications, Faculty of Engineering, Multimedia University, Cyberjaya 63100, Selangor, Malaysia.

[2] Department of Electrical Engineering, Mail Stop 260, University of Nevada, Reno, NV 89557, USA

[*] Corresponding author (e-mail: hairul@mmu.edu.my / hairul.azhar@mmu.edu.my; drhairul@gmail.com)

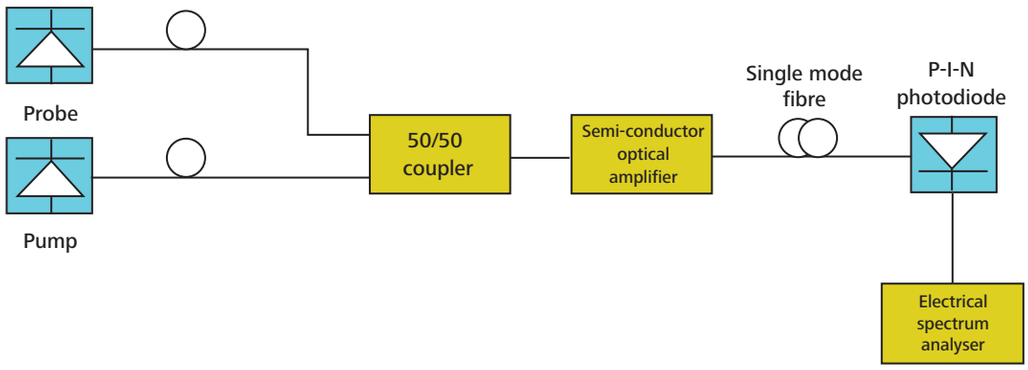

Figure 1. Setup of CD measurement technique using the two beating frequency technique.

Equation 1

$$I(t) = \Re \cdot \left(\begin{array}{l} P_o \cos\left(\omega_{probe}\, t - \omega_{pump}\, t + \beta_{pump}\, z - \beta_{probe}\, z\right) \\ + \sqrt{P_o P_{FWM\,1}} \cos\left[\omega_{pump}\, t - \omega_{FWM\,1}\, t + \beta_{FWM\,1}\, z - \beta_{pump}\, z + \phi_{chirp}(t)\right] \\ + \sqrt{P_o P_{FWM\,2}} \cos\left[\omega_{FWM\,2}\, t - \omega_{probe}\, t + \beta_{probe}\, z - \beta_{FWM\,2}\, z + \phi_{chirp}(t)\right] \\ + \sqrt{P_o P_{FWM\,1}} \cos\left[\omega_{probe}\, t - \omega_{FWM\,1}\, t + \beta_{FWM\,1}\, z - \beta_{probe}\, z + \phi_{chirp}(t)\right] \\ + \sqrt{P_o P_{FWM\,2}} \cos\left[\omega_{FWM\,2}\, t - \omega_{pump}\, t + \beta_{pump}\, z - \beta_{FWM\,2}\, z + \phi_{chirp}(t)\right] \end{array} \right) \quad (1)$$

where:

P_o, $P_{FWM\,1}$ and $P_{FWM\,2}$ are the average optical power for the pump or the probe and the two FWM phase conjugated signals, respectively;

ω_{pump}, ω_{probe}, $\omega_{FWM\,1}$ and $\omega_{FWM\,2}$ are the angular optical frequency for the pump, probe and the two FWM phase conjugated signals, respectively;

β_{pump}, β_{probe}, $\beta_{FWM\,1}$ and $\beta_{FWM\,2}$ are the propagation constants for the pump, probe and the two FWM phase conjugated signals, respectively;

$\phi_{chirp}(t)$ is the phase associated with chirp of the SOA

corresponding to the sum of the angular optical frequencies which were filtered out. Based on the property of the FWM effect and since $\omega_{probe} - \omega_{pump} = \omega_1$, the first three terms in Equation 1 had the same centre frequency ω_1 and the last two terms had center frequencies at $2\omega_1$. The first three terms in Equation 1 centred at ω_1 were denoted as the main beating term, $I_{main\text{-}beating}$. The last two terms centred at $2\omega_1$ were denoted as FWM beating term, $I_{FWM\text{-}beating}$.

The phase differences in the main beating term were random processes and were uncorrelated to each other. Therefore, the total average power of the main beating term $P_{main\text{-}beating}$ was constant although the accumulated

CD values changed. Since the average optical power of the pump and probe were equal, we could assume $P_{\text{FWM 1}} = P_{\text{FWM 2}}$. By taking the PSD of $I_{\text{main-beating}}(t)$, the $P_{\text{main-beating}}$ can be written as in Equation 2:

$$P_{\text{main-beating}} = \frac{P_o^{\,2}}{2} + P_o P_{\text{FWM 1}} \tag{2}$$

$P_{\text{FWM-beating}}$ could be found the same way. Since the terms in $I_{\text{FWM-beating}}(t)$ were a result of the beating between two correlated optical signals and their frequency separation were the same, we could assume that $\beta_{\text{FWM 1}}z - \beta_{\text{probe}}z - \beta_{\text{FWM 2}}z - \beta_{\text{pump}}z$. By taking the PSD of $I_{\text{FWM-beating}}(t)$, the $P_{\text{FWM-beating}}$ could be written as:

$$P_{\text{FWM-beating}} = \frac{P_o P_{\text{FWM 1}}}{2}\left[\cos\left(\frac{z\lambda_o^{\,2}}{4\pi c} D 2\omega_1^{\,2} + \phi_{\text{chirp}}(t)\right)\right] \tag{3}$$

In order to measure the accumulated CD in the transmission fibre, the total average power in Equation 3 was observed as shown in Equation 2. The total average power in Equation 3 is dependent on accumulated CD, the linewidth enhancement factor of the SOA (chirp) and wavelength separation. For a known SOA linewidth enhancement factor and at a fixed frequency separation, the total average power was only proportional to the accumulated CD value.

Using the expressions in Equation 2 and 3, the relative main to FWM beating power P_{relative} was given as in Equation 4:

$$P_{\text{relative}} = \frac{P_o^{\,2} + 2P_o P_{\text{FWM 1}}}{P_o P_{\text{FWM 1}}\left[\cos\left(\frac{z\lambda_c^{\,2}}{4\pi c} D 2\omega_1^{\,2} + \phi_{\text{chirp}}(t)\right)\right]^2} \tag{4}$$

Optimization Parameters

Performance of the CD measurement technique could be measured by the sensitivity and measurement range. The more sensitive and the wider the measurement range of the measurement, the better the technique. The focus in this numerical model was to study the change in the sensitivity and measurement range with respect to wavelength separation.

The sensitivity of the CD measurement technique could be defined as the rate of change of P_{relative} with respect to the accumulated CD. The sensitivity of the CD measurement technique was higher when the rate of change of P_{relative} was faster. The sensitivity of the CD measurement Ω_{CD} was found to be proportional to

$$\Omega_{\text{CD}} \propto \left(\frac{\lambda_o^{\,2}\,\omega_1^{\,2}}{2\pi c}\right)\cdot\tan\left(\frac{zD\,\lambda_o^{\,2}\,\omega_1^{\,2}}{2\pi c} + \phi_{\text{chirp}}(t)\right) \tag{5}$$

The measurement range could be defined as the range between two minimum points of the expression described in Equation 5. The measurement range was wider when these two points were further apart. The measurement was effective only between these two minimum points since the sensitivity was minimized beyond these two points. The measurement range of the CD measurement Θ_{CD} could be quantified by solving Equation 5 for accumulated CD, resulting in:

$$\Theta_{CD} = \frac{2c\pi^2}{\lambda_o^{\,2}\omega_1^{\,2}} \tag{6}$$

NUMERICAL MODEL RESULTS

The numerical model setup is shown in Figure 1, where the pump and probe laser wavelength and output power were 1550 nm and 1550.04 nm, both at 5.0 dBm. Both the optical sources were provided by two different tunable laser sources which allowed changes in the wavelength separation. The SOA used as the phase conjugator had a linewidth enhancement factor of 3.0. Different lengths of fiber spools provided the means to increase the accumulated CD. In each set of measurements in the numerical model, the wavelength separation was changed to study the changes in the sensitivity and measurement range of the CD measurement technique by observing the relative power P_{relative}. The sensitivity of the CD measurement technique reduced with closer wavelength spacing, where the slope of the relative power P_{relative} was less steep as the accumulated CD changed. This observation could be explained by Equation 5 which indicated that the sensitivity of the CD measurement technique Ω_{CD} increased with wavelength separation ω_1. However, one can also observe a wider measurement range at closer wavelength spacing as contained in Equation 6.

Based on the numerical model, the sensitivity and measurement range of the CD measurement technique were derived and plotted in Figure 2 as the wavelength separation was changed. Practically, the sensitivity of the technique for a particular wavelength separation could be represented by the ratio of maximum difference of P_{relative} over the measurement range. The measurement range was taken from Equation 6. Figure 2 illustrates that the CD measurement technique was optimized when the wavelength separation was 5.0 GHz with sensitivity of 0.009 (dB/ps/nm) and measurement range of 2500 (ps/nm).

CONCLUSION

This paper reports the optimization of the CD measurement technique using relative power of two beating frequencies.

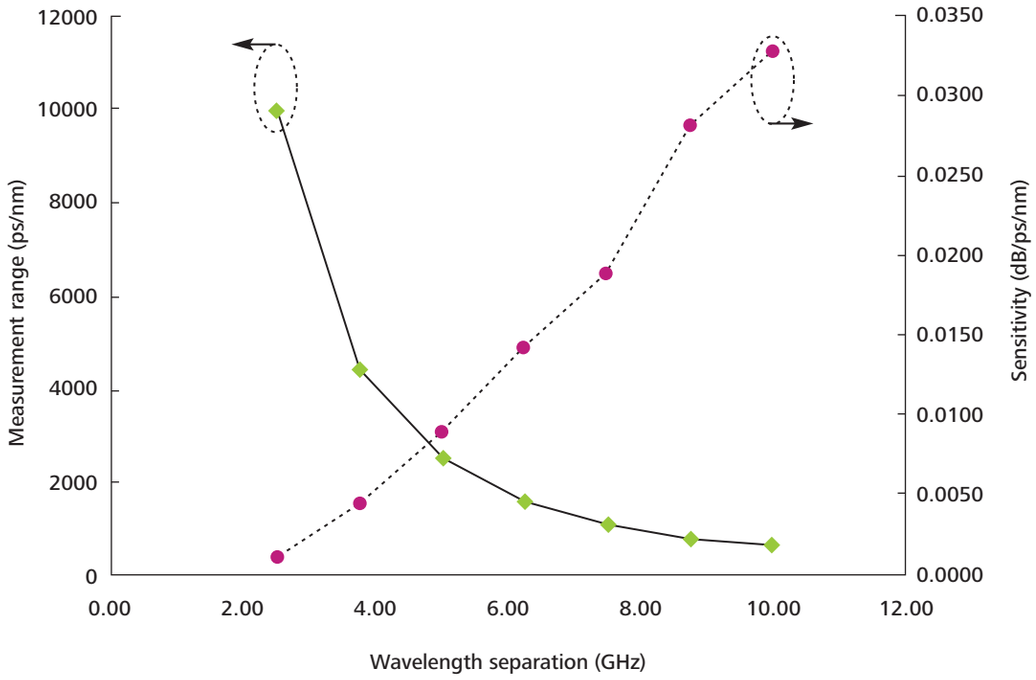

Figure 2. Numerical model of sensitivity and measurement range of the CD measurement technique.

The study focused on the measurement range and sensitivity as the wavelength separation between the pump and probe laser was varied. Based on the numerical model results the CD measurement technique sensitivity increased with wavelength spacing. However, this increase in sensitivity was traded off by the reduction in measurement range. The CD measurement technique was optimized when the wavelength separation was 5.0 GHz with sensitivity of 0.009 (dB/ps/nm) and measurement range of 2500 (ps/nm). With the optimization, a more accurate measurement of the accumulated CD in the fibre could be made while having a wider measurement range.

Date of submission: April 2008
Date of acceptance: October 2008

REFERENCES

Al-Qdah, MT, Abdul-Rashid, HA, Abdullah, MK & Ali, BM 2005, 'Chromatic dispersion measurement using relative power of two beating frequencies', *Microwave and Optical Technology Letters*, vol. 46, no. 3, pp. 268–271.

Park, J, Youn,CJ, Lee, JH & Chung, YC 2000, 'Chromatic dispersion monitoring technique in WDM network', *IEEE Photon. Technol. Lett*. vol. 12, pp. 900–902.

Petersen, MN, Pan, Z, Havstad, SA & Willner, AE 2002, 'Online chromatic dispersion monitoring and compensation using a single inband subcarrier tone', *IEEE Photon. Technol. Lett*., Vol. 14, no. 4, pp. 570–572.

Wielandy, S, Fishteyn, M, Her, T, Kudelko, D & Zhang, C 2003, 'Dispersion monitoring and automatic compensation based on a differential nonlinear detection scheme', in *Tech. Dig. Optical Fiber Communications (OFC 2003)*, pp. 166–168.

ASM Sci. J., **2(2)**, 133–137

SNR Improvements in Self-heterodyne Detection Technique for Laser Linewidth Measurements

R. Manimaran[1] and H.A. Abdul-Rashid[1*]

This paper proposes a signal-to-noise-ratio (SNR) improvement by using an external phase modulator that allowed flexible control of the spectrum amplitude by varying the modulation index for linewidth measurements. Compared with the conventional self-heterodyne detection technique, the results obtained in this study showed an SNR improvement as high as 10 dB. This 10 dB improvement in SNR could help to reduce the usage of a particular length of a single mode fibre (normally about 50 Km) when measuring a linewidth in the region of 10 kHz.

Key words: self-heterodyne; coherent length; linewidth; laser characteristics; SNR improvement; spectrum amplitude; detection technique; phase modulation; simulation

Lasers with ultra-long coherent length or exceptionally low phase noise have become a strong interest in optical communication. Measuring the linewidth of such lasers is then very important, nonetheless very challenging. Several methods of measuring the laser linewidth have been researched extensively, namely self-homodyne, heterodyne (Chen 2006) and self-heterodyne techniques (Nezu *et al*. 1989). The self-heterodyne detection technique provides more accurate results compared to other methods and its simplicity and high resolution makes it an obvious choice to measure laser line width. However, for this system to measure the line width accurately, the two interfering waves should be mutually independent which requires the fibre length which provide the delay to be at least 6 times the coherence length of the source as suggested by Richter (1986). This requirement for accuracy becomes dominant when the system is applied to measure very narrow line width lasers as the fibre length requirement will be very long. Incorporating excessively long optical fibres is associated with degradation factors such as fibre non-linearity (Mercer, 1991) and attenuation. Under such situations, the output SNR is degraded and affect the accuracy of linewidth measurement as extracting the linewidth using 20 dB measurement may no longer be possible. This paper studies the effect of fibre length on SNR in laser linewidth measurement using the self-heterodyne detection technique. The authors propose SNR improvements by using an external phase modulator which provides the frequency shift and if optimized could be used to improve the SNR of the spectrum. Compared with conventional self-heterodyne detection technique, the results when an external phase modulator was used in a self-heterodyne detection technique showed an SNR improvement of approximately 10 dB when measuring 10 kHz linewidth laser using 39 km length of fibre. This improvement of 10 dB translates into saving 50 km of fibre length.

In this study the self-heterodyne detection technique is described and its dependency on fibre length in order to obtain accurate linewidth measurement is demonstrated. The proposed improvement in the self-heterodyne detection technique using an external phase modulator was also discussed.

SELF-HETERODYNE DETECTION TECHNIQUE

The self-heterodyne detection method is one of the most commonly used methods to measure linewidth due to its simplicity and accuracy. In this method, the laser beam is split to travel along two diferent path lengths so that one is delayed and the other is frequency shifted compared to the other as shown in Figure 1. The linewidth measurement is performed by analyzing the radio frequency (RF) beating spectrum between the laser under study and its time delayed version. In the limit of large delay time, the spectrum becomes exactly Lorentzian with a width equal to twice the laser optical spectral width. The length of the fibre necessary to provide the sufficient delay becomes very long when this method is applied to measure very narrow linewidths. It has been established that the fiber length should be at least 6 times the coherent length. The linewidth Δ_v, group index of refraction of the propagation medium n_g , are related to the coherence length l_c by Lally 2006 as:

$$l_c = \frac{c}{\pi n_g v \Delta_v} \quad (1)$$

[1] Institute of Photonics Research and Applications, Multimedia University, Cyberjaya 63100, Selangor, Malaysia

[*] Corresponding author (e-mail: hairul@mmu.edu.my)

where *c* is the speed of light in vacuum. For example, to measure a laser with linewidth of 100 Hz, the fibre length required is 3900 km since the coherent length is 650 km. However, excessively long optical fibres are associated with degradation factors such as fibre non-linearity and attenuation.

The laser linewidth can be inferred from the self-heterodyne spectrum by measuring the linewidth at –3 dB, –10 dB, or –20 dB levels. Earlier reports show that –20 dB measurements provides accurate results since the broadening effect of the 1/f noise is more pronounced at the center of the spectral lineshape as shown by Mercer (1991). If we need to make a –20 dB measurement, the signal and noise levels should permit a difference of at least 20 dB. As the length of the fibre used in the measurement is increased, the signal level decreases thus degrading the SNR. The reduction in signal level and increase in noise level are due to fibre loss and fibre non-linearity, respectively. Therefore, in order to improve the accuracy in laser linewidth measurement using self-heterodyne detection technique, the SNR needs to be improved. The 1/f noise occurs in a surprising variety of physical systems but the physical processes which give rise to such a spectrum are not generally known. The origin of 1/f noise in lasers has been discussed by several authors and a number of possible mechanisms have been proposed. Included in these are mode partition noise, event driven temperature fluctuations and fluctuations in local current density, optical absorption coefficient or free carrier concentration (Kitching *et al*. 1980).

One way to improve the SNR is to decrease the fibre length used in the self-heterodyne detection technique, which will reduce the losses considerably. However, in order to obtain accurate laser linewidth measurement, the fiber length should be at least equal to the coherent length of the source so that the two interfering waves are mutually independent and as if coming from two independent sources. Figure 2 shows linewidth measurement results obtained from a 10 kHz linewidth laser using the self-heterodyne detection technique. The simulation results here showed that the accuracy of the linewidth improved when the fiber length used was about 6 times the coherent length of the laser source. When the fiber length was less than the coherent length of the laser source, the two optical signals that produced the beating signal were not mutually incoherent and as a result, the linewidth measured by the system was smaller than the actual linewidth.

SELF-HETERODYNE DETECTION TECHNIQUE USING EXTERNAL PHASE MODULATION

In order for the self-heterodyne detection to measure accurately, the spectral distribution of the beating signal should be shifted away from DC. This can be achieved by a number of devices such as intensity modulators (Mercer 1991), phase modulators (Nguyen 1998) and acousto-optic modulators (Dougherty *et al*. 1980). Besides using phase modulators to shift the beating signal spectrum from DC, it also provides additional flexibility in controlling the amplitude of the spectrum by varying the modulation index. An improvement in the spectrum amplitude would thus improve the SNR of the beating signal. The setup of a self-heterodyne detection with external phase modulator to provide the phase shift and improve the SNR is shown in Figure 3.

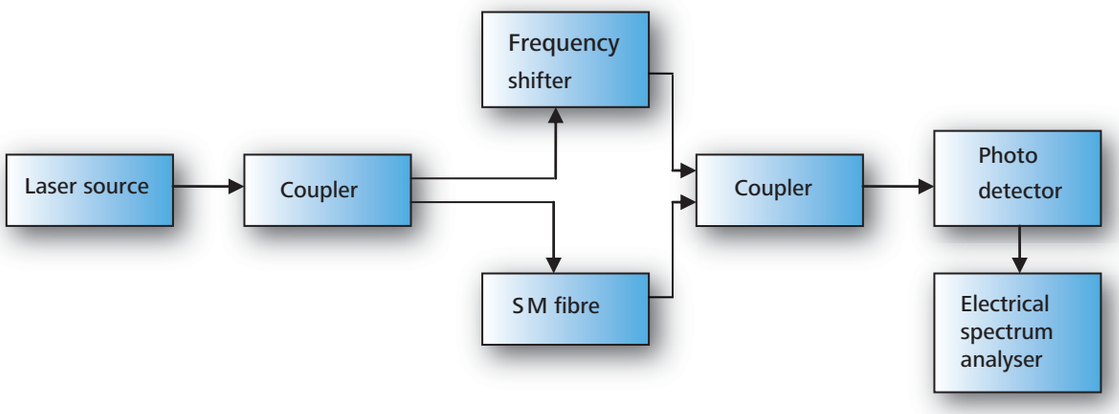

Figure 1. Laser Linewidth measurement setup using self-heterodyne detection technique.

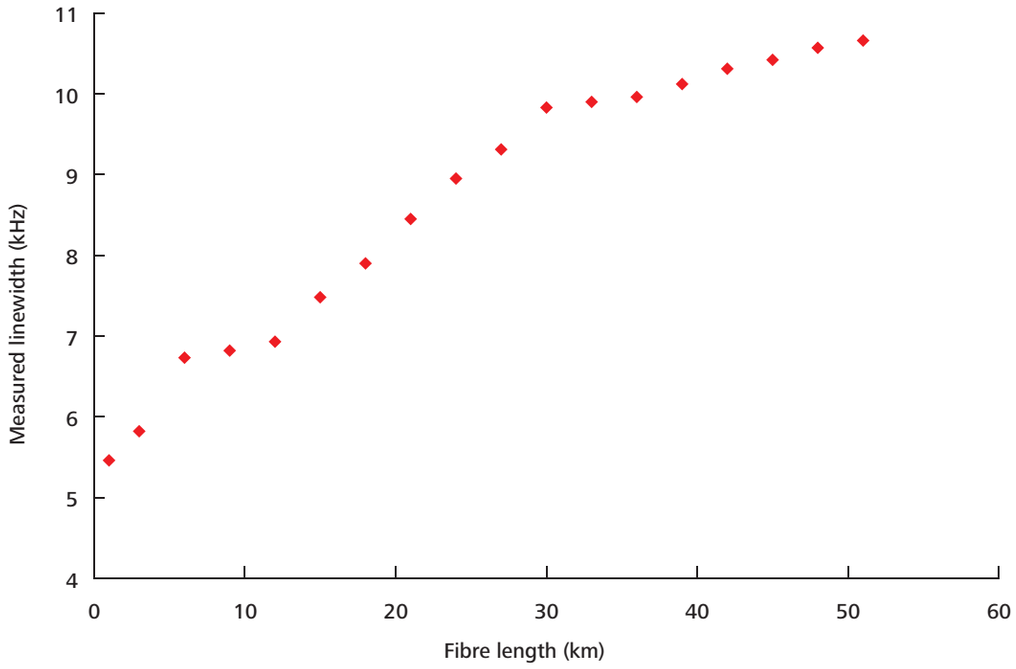

Figure 2. Measured linewidth variation when different fibre length is used in the self-heterodyne detection technique.

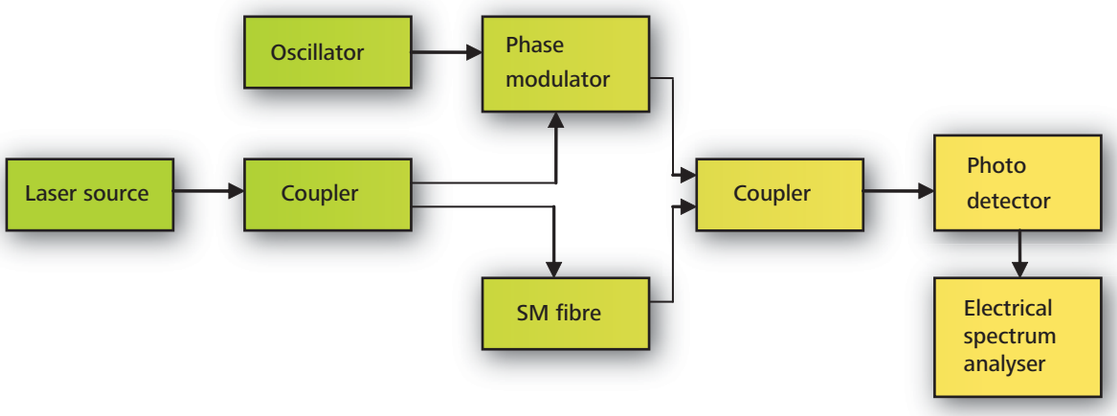

Figure 3. Self-heterodyne detection technique with external phase modulator for frequency shift.

The photo detector current is given by (Nguyen 1998)

$$I(t) = 2E_0^2 \{1 + \sum_{m=-\infty}^{\infty} J_m(\delta)\cos[\varphi(t) - \omega_0\tau - \varphi(t+\tau) + m\Omega t]\} \quad (2)$$

where,

E_o and φ is the amplitude and phase of the laser output, respectively,

τ is the propagation delay time,

$J_m(\delta)$ is the Bessel function,
δ is the modulation index and Ω is the frequency shift provided by the phase modulator.

Taking the Fourier Transform of Equation 2 showed that the electrical spectral density of the current consisted of a DC term and Lorentzian linewidth distribution centered at $m\Omega$. The strength of the Lorentzian linewidth distribution centered at $m\Omega$ would be determined by the modulus of Bessel function coefficient $J_m(\delta)$. Equation (2) shows that the photo diode current was dependent on the strength of the Bessel coefficient as shown in Figure 4 below. The strength of the Bessel coefficient depended on the modulation index as indicated by the Equation 2. Hence the magnitude of the photo diode current and therefore the output spectrum power depended on the modulation index.

RESULTS AND DISCUSSION

A computer simulation of the proposed self-heterodyne detection technique to measure laser linewidth was carried out. The simulation setup is as shown in Figure 3. The laser under study was a DFB laser with 10 kHz linewidth. The phase modulator input was a signal with frequency 10 GHz and the single mode fiber length was varied to provide the required delay. The PIN photodiode was used to detect the self-heterodyne signal and the Electrical Spectrum Analyzer with resolution of 500 points between 9.9 GHz and 10.2 GHz measured the spectrum of the self-heterodyne signal.

The signal peak power variation with different optical modulation index was plotted for different fibre lengths in Figure 4. It could be seen that the SNR is maximum when the modulation index was approximately 64%. Figure 5 showed the improvement in SNR using an external phase modulator compared to frequency shifter using an accousto-optic modulator. An improvement of about 10 dB was observed using an optimized external phase modulator with optical modulation index of 64%. Although signal peak power improvement could be seen for modulation index from 48% to 68%, spectrum peak was maximum at the modulation index of 64%. Since we were concerned with the maximizing the SNR, this modulation index of 64% could be taken as the optimum value. The improvement in SNR would allow self-heterodyne systems using long fibers to measure the laser linewidth at the 20 dB level and improve measurement accuracy. Besides the SNR improvement, the use of an external phase modulator allowed an advantage of approximately 50 km before the SNR reached the minimum 20 dB level, as shown in Figure 5.

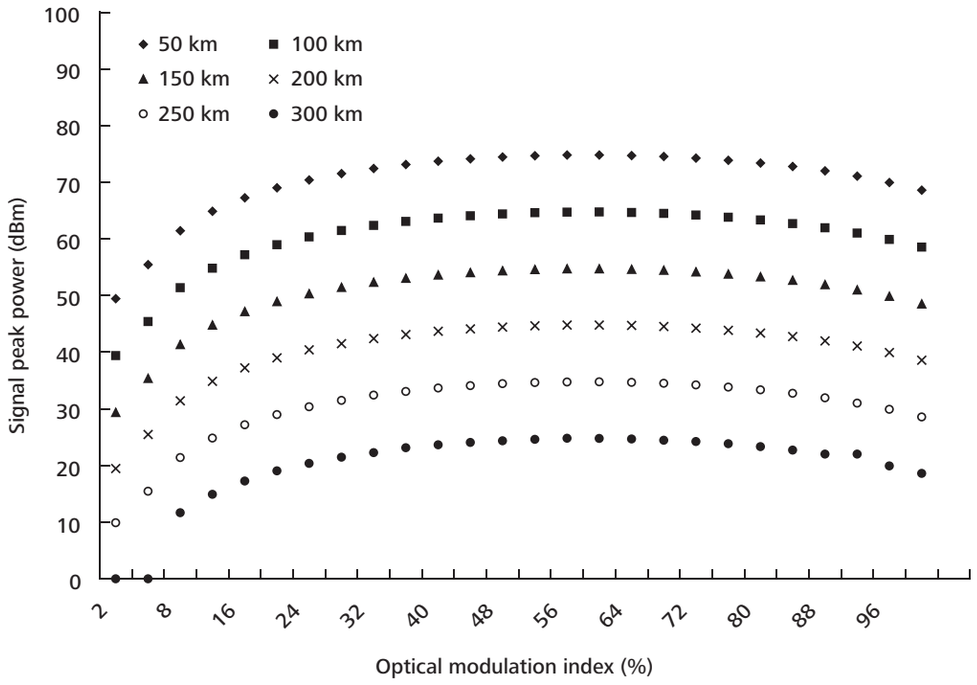

Figure 4. Signal peak power (dBm) vs. optical modulation index (%) for various fibre lengths.

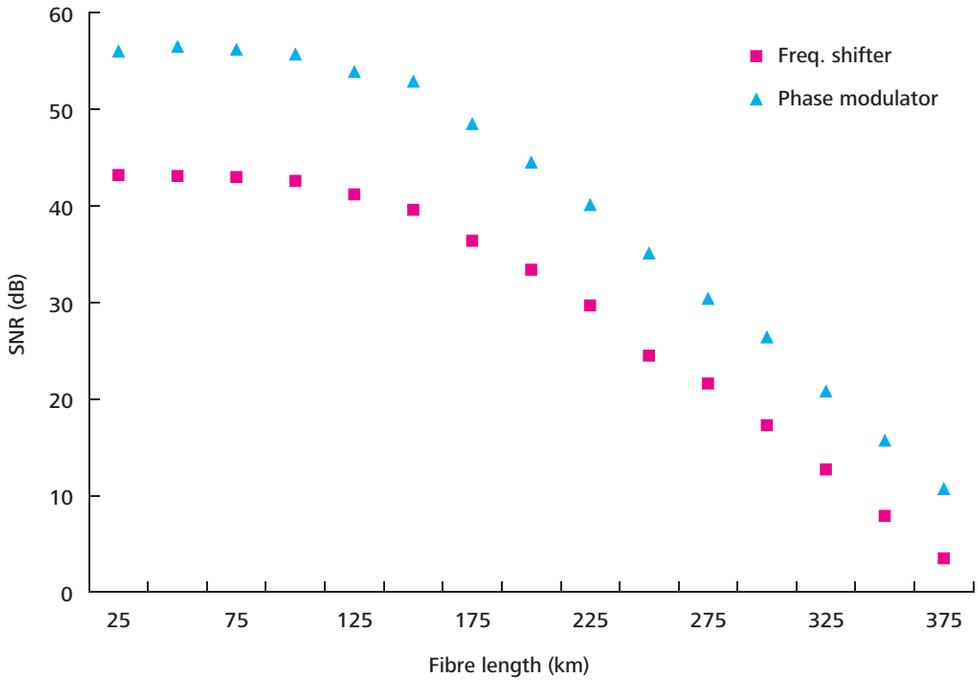

Figure 5. SNR improvement when the external phase modulator is used as a function of fibre length.

CONCLUSION

This paper studied the various factors influencing the SNR in the self-heterodyne linewidth measurement technique when it was used to measure ultra-narrow linewidth lasers. It was shown that when the spectrum SNR was considerably higher then 20 dB, source linewidth could be measured more accurately. However, when long fibres were used to provide the necessary propagation delay, the minimum 20 dB SNR was compromised. Use of an external phase modulator for frequency shift to improve SNR was considered. It was shown that optical modulation index of 64% would improve SNR the most. Compared with conventional self-heterodyne detection techniques, the results when an external phase modulator was used showed an SNR improvement as high as 10 dB and an additional 50 km advantage when measuring 10 kHz linewidth laser.

Date of receipt: April 2008
Date of acceptance: December 2008

REFERENCES

Chen, X 2006 'Ultra-narrow laser linewidth measurement', PhD thesis, Virginia Polytechnic Institute and State University.

Dougherty, DJ, Guttierrez, RC, Dubovitsky, S & Forouhar S 1980 'Semiconductor laser line width measurements for space interferometry applications', *Electron Lett*., vol. 16, no.16, pp. 630–634.

Evan, ML 2006, 'A narrow-linewidth laser at 1550 nm using the pound-driver hall stabilisation technique', MSc thesis, Virginia Polytechnic Institute and State University, August.

Kitching, J, Shevy, Y, Iannelli, J & Yariv, A 1993, 'Measurements of 1/f noise reduction in semiconductor lasers using optical feedback with dispersive loss', *Journal of Lightwave Technology*, vol. 11, no.10, pp. 1526–1532.

Mercer, LB 1991, '1/f frequency noise effects on self-heterodyne line width measurement', *Light Wave Tech*, vol. 9, no. 4, pp. 485–493.

Nguyen, LVT 1998, '*Distributed-feedback (dfb) laser coherance and linewidth broadening*', Defence Science and Technology Organisation, Department of Defence, Australia.

Richter, LE 1986, 'Linewidth determination from self-heterodyne measurements with subcoherence delay times', *IEEE Journal of Quantum Electronics*, vol. QE-22, no.11, pp. 2070–2074.

Tadashi, N, Tanaka, Y & Kurokawa, T 1989, 'Delayed self-heterodyne linewidth measurement of fibre grating laser', *IEEE Journal of Quantum Electronic*, vol. 25, pp. 684–688.

ASM Sci. J., **2(2)**, 139–148

Analysis of a Low Refractive Index Grating Waveguide Polarisation Splitter Based on Resonant Tunnelling

M.H.M. Yusoff[1,2]* H.A. Hassan[1], M.R. Hashim[1] and M.K. Abd-Rahman[2]

The fabrication tolerance of a short and compact low refractive index grating waveguide polarisation splitter based on the principle of resonant tunnelling was analyzed in this study. The design utilised two grating waveguides with an intermediate conventional waveguide layer. The design and optimisation were conducted using the quasi 2-D effective index solver with global search algorithm. An optimum device operating at 1.55 μm wavelength was obtained at a length of 340 μm. The splitting ratios were calculated to be 36 dB and 15 dB, and the overall device transmission efficiencies, after considering the three-dimensional waveguide leakage loss, were estimated at 88% and 83% for tranverse magnetic and tranverse electric polarisation, respectively.

Key words: grating waveguide; polarisation splitter; resonant tunnelling; low refractive index; simulation

A polarisation splitter is an important component in optical communication and sensor applications. Polarisation splitters based on different principles such as metal clad directional coupler (Rajarajan *et al*. 1997), Y-branched waveguide (Ridder *et al*. 1993) and four port Mach-Zehnder interferometer (Soldano *et al*. 1994) have been demonstrated. These devices utilized material with high refractive indices thus realizing short and compact devices.

In this paper, we report the fabrication tolerance and loss analysis of a short and compact grating waveguide polarisation splitter (Yusoff *et al*. 2007) based on resonant tunnelling (Thyagarajan & Pilevar 1992) using material with a low refractive index of 1.458 on silica substrate with a refractive index of 1.444. Previously designed single-mode polarisation splitters based on resonant tunnelling mechanism (Thyagarajan & Pilevar 1992; Huang *et al*. 2005) used three channel waveguides; however, it was necessary to use different optical material for the resonator waveguide. Fabrication tolerance was very strict and the accuracy needed for high index central layer thickness was very high (Thyagarajan & Pilevar 1992). A fabrication tolerant polarisation splitter (Augustin *et al*. 2007) reportedly used a multimode resonator waveguide and its coupling length was in the order of about 3 mm. In the grating waveguide polarisation splitter design using low refractive index material (Yusoff *et al*. 2007), the coupling length achieved is in sub-millimetre length scale, however fabrication tolerance was rather stringent in the grating waveguide structure. At a splitting ratio of 13 dB, the fabrication tolerance in the grating structure was of a few nanometres.

DESIGN PRINCIPLE

The polarisation splitter consisted of a symmetrical three channel directional coupler with a narrow conventional waveguide or resonator (WG2) at the centre and two grating waveguides (WG1 and WG3) on the outside (Figure 1).

The local fundamental quasi tranverse magnetic (TM) and tranverse electric (TE) modes were computed at a wavelength of 1.55 μm using the polarisation dependent effective index method (EIM) (Bienstman 2007; FIMMWAVE 2008). The effective indices for fundamental quasi-TM and quasi-TE modes were computed for waveguides WG1 (WG3) at a slab height of 8.4 μm, width of 0.5 μm and an air gap size of 0.1 μm. Each slab was over-etched 2 μm into the substrate. In Figure 2, each point (circle) computed for the grating waveguide denotes increasing number of slabs, beginning with 2 slabs from the left of the figure to 21 slabs at the far right. The effective width for the grating waveguide was taken to include the total width of the number of slabs including the air gaps. The resonator WG2's effective indices (diamond) were analyzed for slab height of 8.4 μm and width ranging from 0.4 μm to 8 μm. The computed effective index for TM polarized light in the grating waveguide WG1 (WG3) at a total effective width of 6.5 μm (corresponding to 11 slabs) was matched to the effective index of the resonator WG2

[1] School of Physics, Universiti Sains Malaysia, 11800 USM, Penang, Malaysia.
[2] Faculty of Applied Sciences, Universiti Teknologi MARA, 40450 Shah Alam, Selangor, Malaysia.
* Corresponding author (e-mail: mohdhanapiah@salam.uitm.edu.my; mohdhanapiah@hotmail.com)

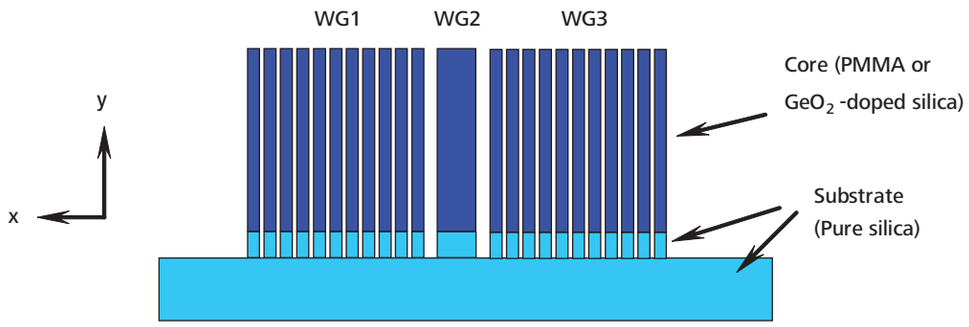

Figure 1. The resonant tunnelling polarisation splitter configuration based on low index grating waveguide.

of width 1.25 µm, and they were in resonance. However for TE polarisations, due to different polarisation birefringence of the resonator compared to the grating waveguides, the TE polarized light was not in resonance. Based on these results, the coupling of light in the two grating waveguides which were having an effective width of 6.5 µm with the resonator at a width of 1.25 µm, would allow the TM polarized light to tunnel through the resonator, while at the same time prevent the TE polarized light from tunnelling through.

The operation of the polarisation splitter was based on a three channel directional coupler; therefore its operation may be explained in terms of *supermodes* of the coupled waveguides. However, if the three channel waveguides were end-coupled to an input from a single mode waveguide as shown in Figure 3, this would excite multiple guided modes and also radiation modes in the three channel waveguides.

At the junction discontinuity ($z = 0$) between the input section and coupled section as shown in Figure 3, Maxwell's equations impose continuity conditions for the field, i.e. the tangential magnetic fields as given in Equation 1, must be equal on each side of the interface.

$$H^x_{\text{input}}(x,y,0) = \sum_{i=1}^{M}\sum_{j=1}^{N} c_{ij} H^x_{ij}(x,y) + \iint H^x_{\text{radiation}}(x,y)\partial x\,\partial y \quad (1)$$

where,

$$c_{ij} = \frac{\iint H^x_{\text{input}}(x,y,0) H^x_j(x,y)\,\partial x\,\partial y}{\sqrt{\iint H^x_j(x,y)^2\,\partial x\,\partial y}}$$

Based on 3-D analysis of the power excitation coefficient or overlap between the input field and the excited modal field in the coupled waveguide section, we found that about 99.2% of the input power was transferred to the first three guided modes, H_{11}^x, H_{21}^x and H_{31}^x, in the coupled section. These modes are the first order vertical modes and two of these modes are symmetrical with one anti-symmetric mode for each of the polarization states were as shown in Figure 4. The analysis also revealed that only about 0.3% of the input power was transferred to H_{12}^x, H_{22}^x, and H_{32}^x, and 0.006% was transferred to H_{13}^x, H_{23}^x, and H_{33}^x, thus allowing the design and optimization process to be simplified by using quasi 2-D EIM based on the first order vertical modes.

In order to obtain an efficient transfer of power from one outside waveguide to another, the effective indices of the first three propagating modes must satisfy the following conditions (Donnelly *et al*. 1987):

$$(n_1 - n_2)_{\text{TM}} \approx (n_2 - n_3)_{\text{TM}} \quad (2)$$

$$(n_1 - n_2)_{\text{TE}} \rangle\rangle (n_2 - n_3)_{\text{TE}} \quad (3)$$

By fulfilling these conditions, it meant that TM polarized light launched into WG1 would couple to WG3 (via tunnelling through WG2) and exit WG3, while the TE polarized light launched into WG1 would mainly exit through WG1. The crosstalk and splitting efficiency in three waveguides couplers, due to the uneven spacing of the effective indices of the three eigenmodes in the coupling region were quantified in terms of the extinction and splitting ratios, ER_{TE} and SR_{TE} for TE polarisation, and ER_{TM} and SR_{TM} for TM polarisation (Equations 4 and 5):

$$\text{ER}_{\text{TE}}\,(\text{SR}_{\text{TE}}) = 10\log_{10}\frac{\text{Output power of TE polarization in WG1}}{\text{Output power of TM (TE) polarization in WG1 (WG3)}} \quad (4)$$

$$\text{ER}_{\text{TM}}\,(\text{SR}_{\text{TM}}) = 10\log_{10}\frac{\text{Output power of TM polarization in WG1}}{\text{Output power of TE (TM) polarization in WG3 (WG1)}} \quad (5)$$

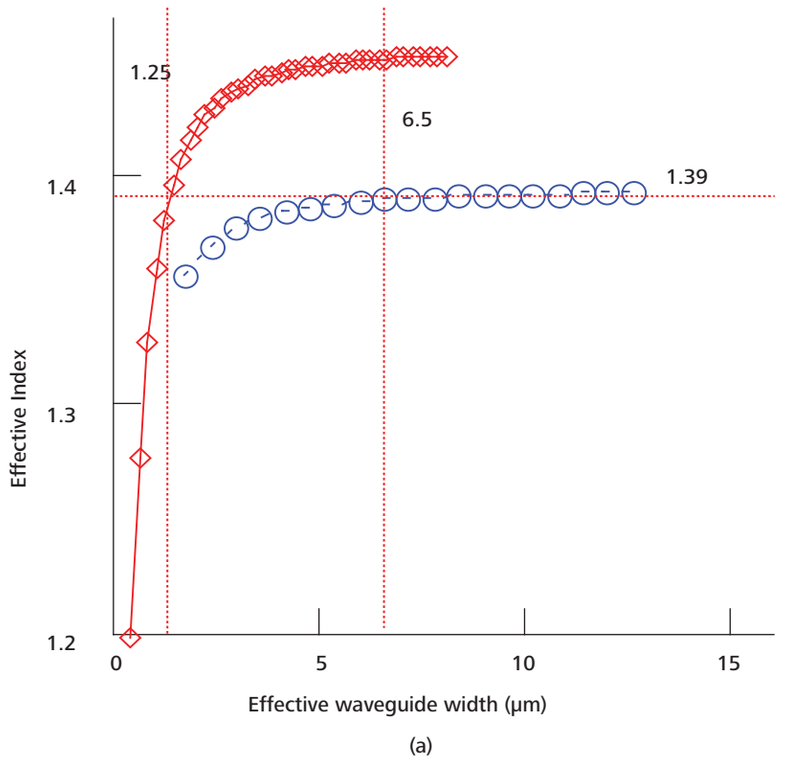

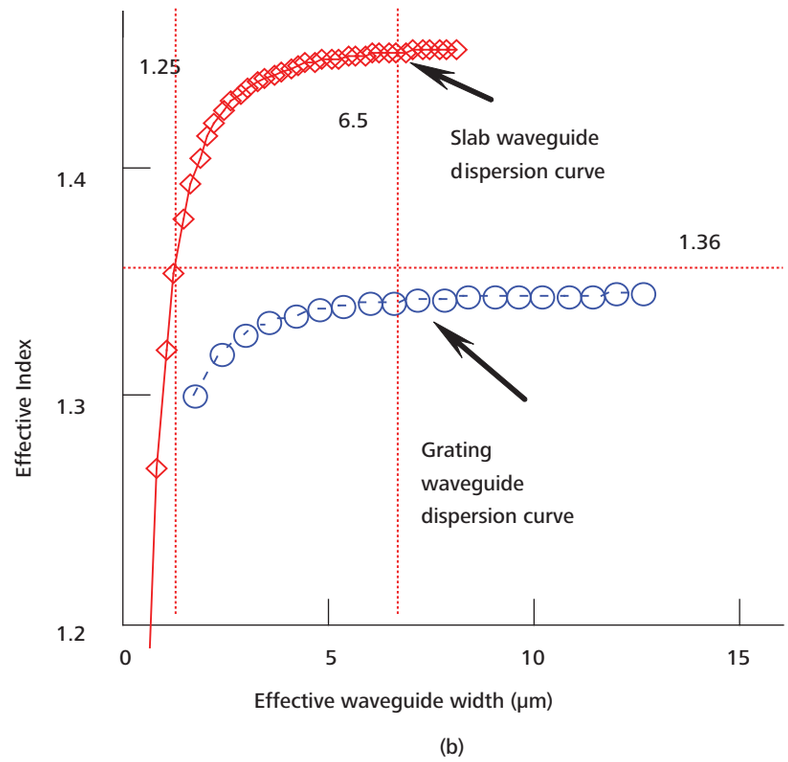

Figure 2. The grating waveguide WG1 (WG3) effective indices (circles) shown for (a) TM and (b) TE polarisation were computed for the grating waveguide slab width of 0.5 μm, with an air gap size of 0.1 μm. The conventional slab waveguide effective index (solid line – diamonds) was computed for waveguide width from 0.4 μm to 8 μm.

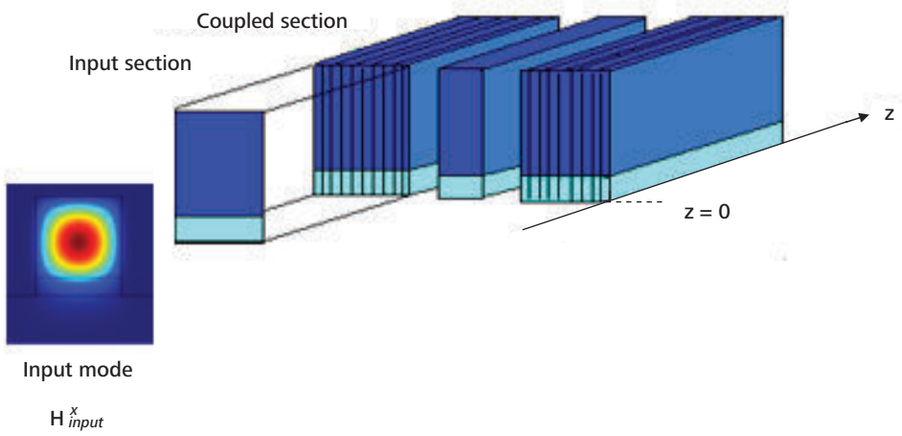

Figure 3. The input singlemode waveguide is end-coupled to the three channel waveguide directional coupler.

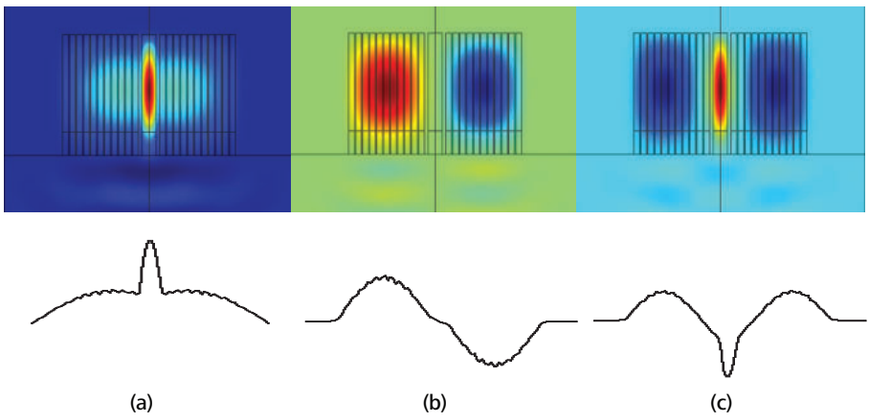

Figure 4. Supermodes in the coupling section of the grating waveguide polarisation splitter. The modes in Figures 4(a), 4(b) and 4(c) are having effective indices n_1, n_2 and n_3, respectively.

RESULTS AND DISCUSSION

The polarisation splitter design comprised of three sections: the input, output and coupled sections, as shown in Figure 5. The coupled section would split the TE and TM polarized light. The initial design parameters obtained from the previous section were optimized using quasi 2-D effective index - eigenmode expansion (EIM-EME) method (FIMMWAVE, FIMMPROP 2008) and global search algorithm (KALLISTOS 2008) with the objective of minimizing the difference in effective index spacing as stated in Equation 2. By satisfying Equation 2, the power transfer for TM polarisation, propagating from Port 1 to Port 3 would be maximized. The optimization was conducted by varying the resonator's width and the air gaps between resonator and grating waveguides. The grating waveguide's parameters, width of 0.5 µm and air gap of 0.1 µm, with 11 arrays of dielectric slabs were maintained constant throughout this process. The optimum design obtained with the stated objective consisted of a resonator width of 1.212 µm and an air gap of 0.308 µm. The field intensity for the TM and TE modes at 1.55 µm is shown in Figure 6.

In the 2-D transmission analysis based on EIM-EME method (FIMMWAVE, FIMMPROP 2008), we used 100 modes in the modal expansion of the coupled waveguides in the coupling section, consisting of guided and radiation modes. The transmission efficiencies for TM

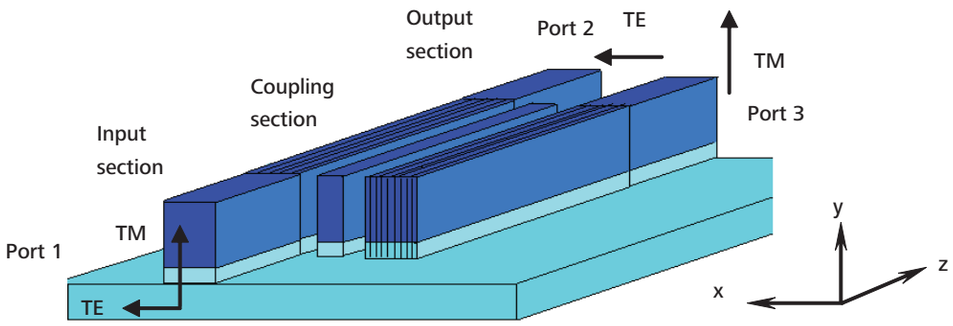

Figure 5. Polarisation splitter designed with two grating waveguides and an intermediate conventional waveguide (resonator).

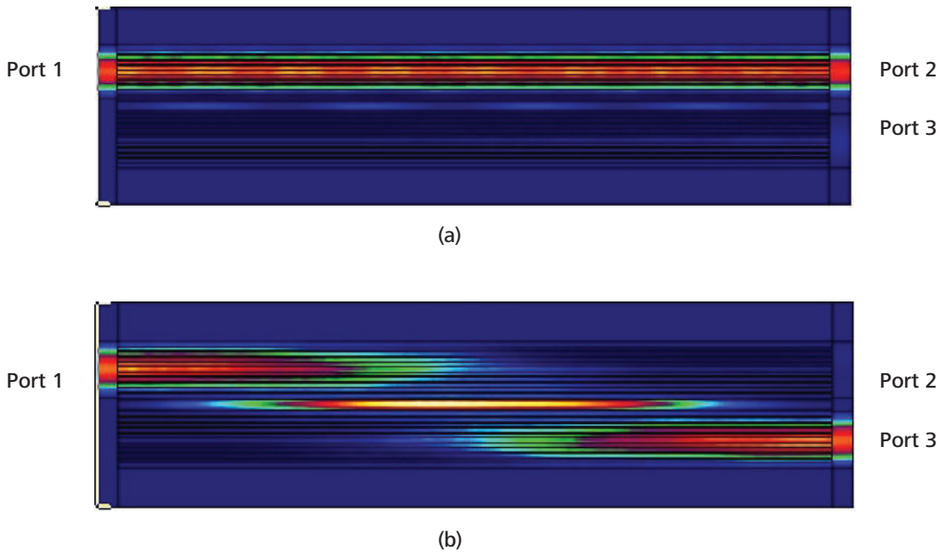

Figure 6. Field intensity of (a) TE polarized light launched into Port 1 exiting Port 2, and (b) TM polarized light launched into Port 1 exiting Port 3, computed using quasi 2-D EIM-EME method.

and TE polarized light are as shown in Figure 7(a). The transmission maximum for TM output was about 350 µm. In order to increase the splitting ratio [Figure 7(b)] in the TE polarized light to about 15 dB, we chose a length of 340 µm for the coupled section. The transmission efficiencies of the device at this length were 99% and 96% for TM and TE polarisation, respectively. However these transmission efficiencies were based on 2-D propagation analysis in the x-z directions, they did not include leakage loss in the y-direction. The leakage losses shown in Figure 8, for the grating waveguide and the resonator were estimated with three-component H-field computation using quadratic vector finite elements implemented with perfectly matched layer (COMSOL 2008). In the grating waveguide, at an operating wavelength of 1.55 µm, the TM and TE mode losses for waveguide width of 6.5 µm were 1.85 dB/mm and 1.93 dB/mm, respectively. The corresponding mode loss in the resonator at a slab width of 1.212 µm for TM mode was 1.2 dB/mm. Considering the 2-D transmission efficiencies and the leakage loss of local modes in the y-direction, the overall transmission efficiencies were estimated to be about 88% and 83% for TM and TE polarisation, respectively.

The splitting ratios were 36 dB and 15 dB for SR_{TM} and SR_{TE}, respectively. In terms of splitting efficiency they were 99.97% and 96.84%, respectively. We further conducted fabrication tolerance analysis on parameters related to the design and varied the grating waveguide, resonator's

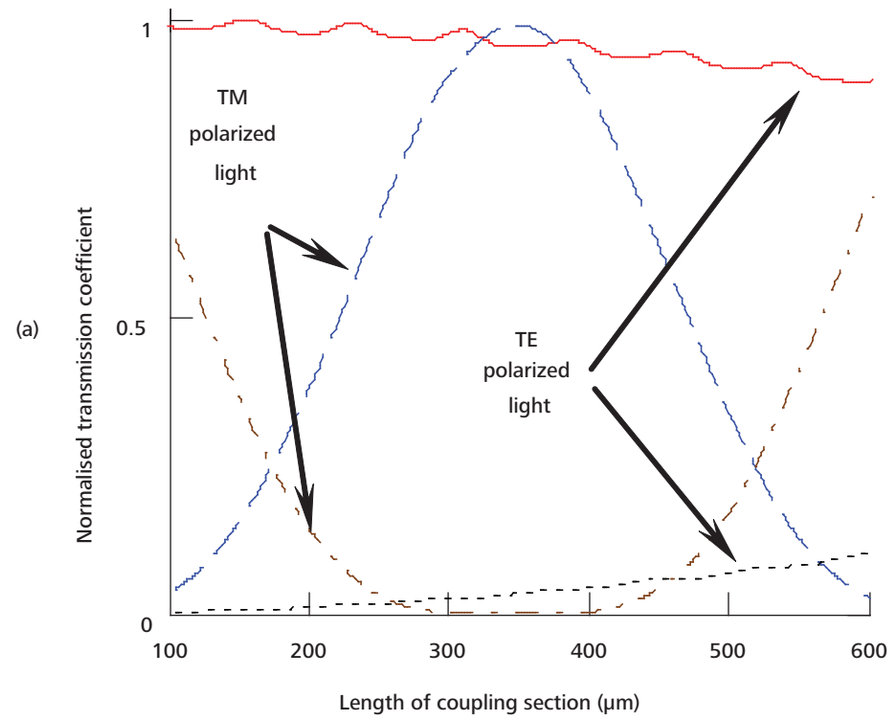

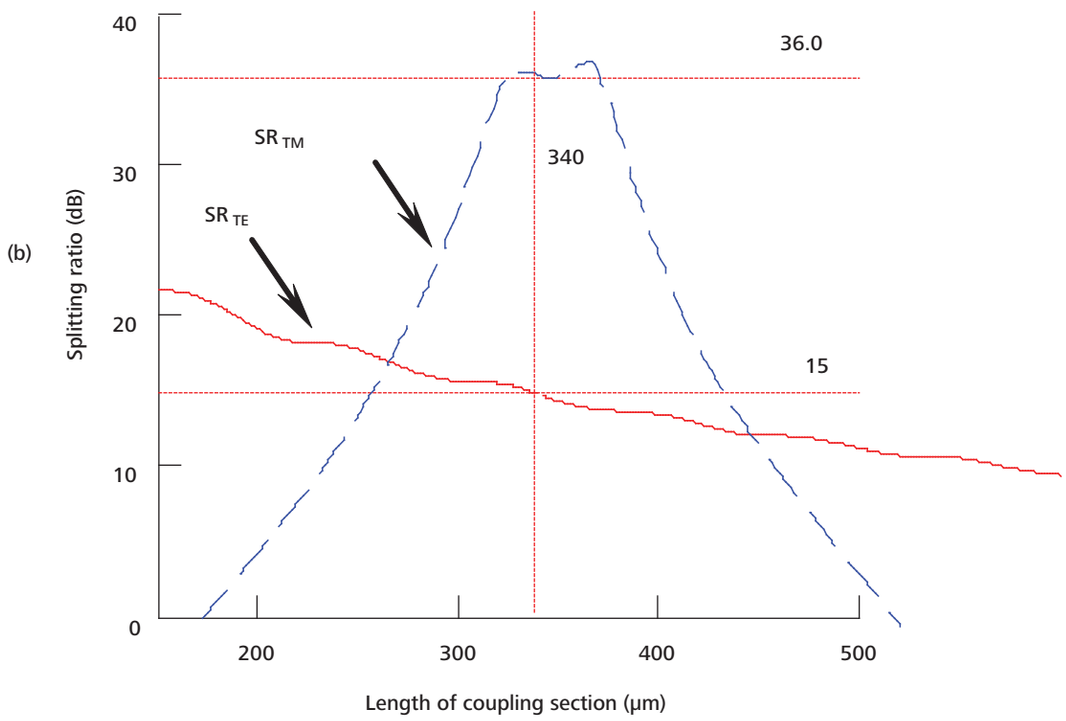

Figure 7. (a) The transfer coefficient of the TE and TM polarized light launched into Port 1. The solid (dash-dotted) line and dotted (dashed) lines are the TE (TM) polarized light exiting Ports 2 and 3, respectively; (b) The splitting ratio (SR) calculated for TE and TM polarisation are shown by solid and dashed lines, respectively. Both figures shown are results analyzed against length of coupling section.

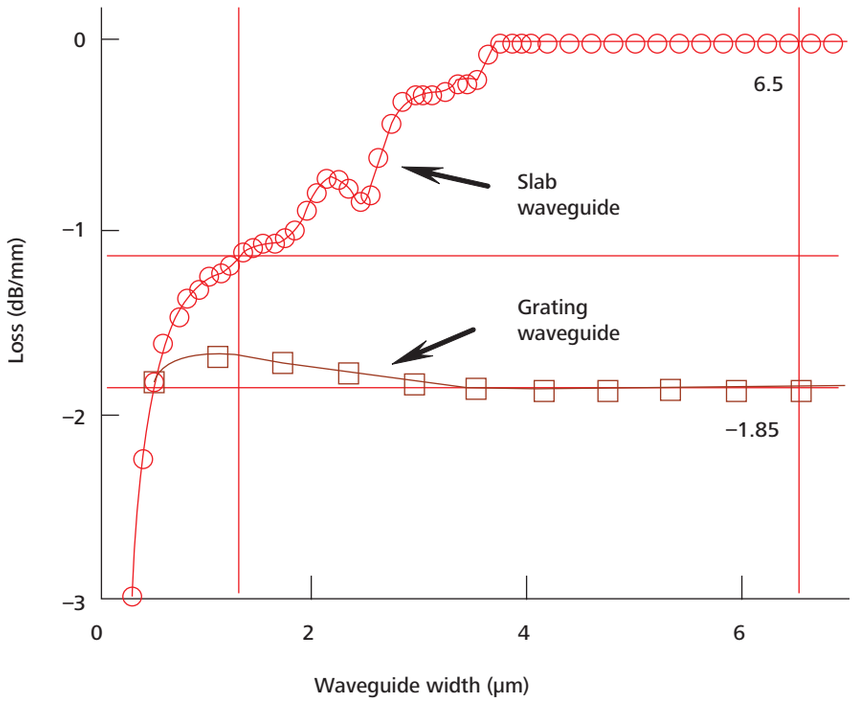

(a)

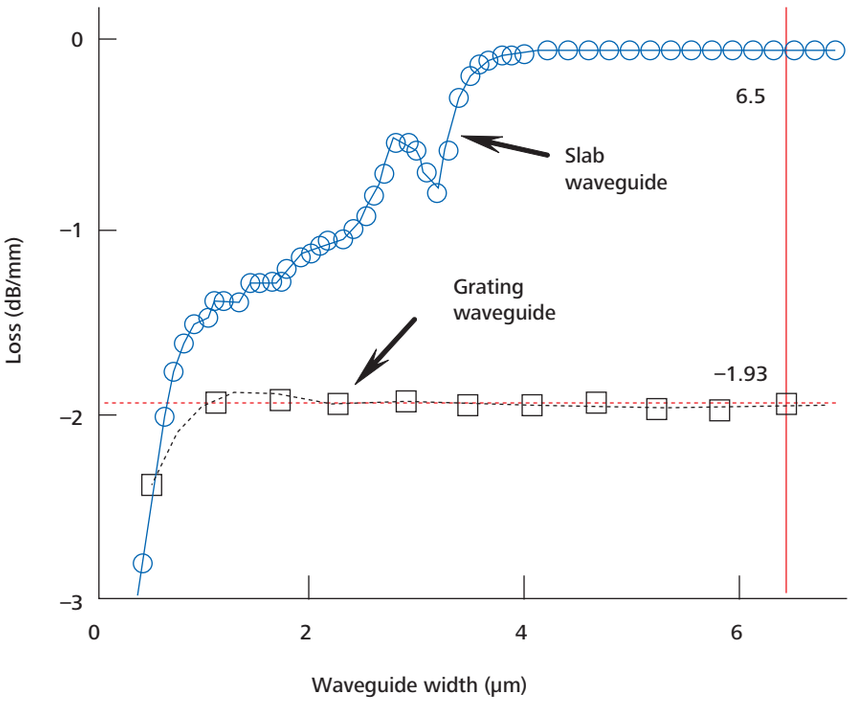

(b)

Figure 8. Loss analysis were based on full vectorial H-field computation using finite elements with perfectly matched layer boundary conditions. In the grating waveguide, (a) TM and (b) TE mode losses at waveguide width of 6.5 μm were 1.85 dB/mm and 1.93 dB/mm, respectively. Mode loss in resonator at a slab width of 1.212 μm for TM mode was 1.2 dB/mm.

slab width and air gap size, and we found that the critical parameter in this design was the grating waveguide air gap size. In order to attain an SR of greater than 13 dB or 95% needed for a practical polarisation diverse scheme (Hanfoug *et al*. 2003), the required tolerance in the size of the grating waveguide air gap (g_s) was ±1.7 nm from the optimum gap of 0.1 µm, as was limited by the device splitting ratio for TM polarisation. The tolerance for the resonator width (w), resonator's air gap (g) and grating waveguide slab width (w_s) were less stringent, values ranged from ±13 nm, ±14 nm and ±7 nm, respectively. Figure 9 shows the parameters that were varied in the fabrication tolerance analysis, and as shown in Figure 10 were their respective SRs obtained in the analysis.

CONCLUSION

In conclusion we have proposed an efficient and compact polarisation splitter based on low refractive index grating waveguide. The simulated SR_{TM} and SR_{TE} were 36 dB and 15 dB for a device length of 340 µm, respectively. However the fabrication tolerance was rather strict, especially for the grating waveguide air gap size.

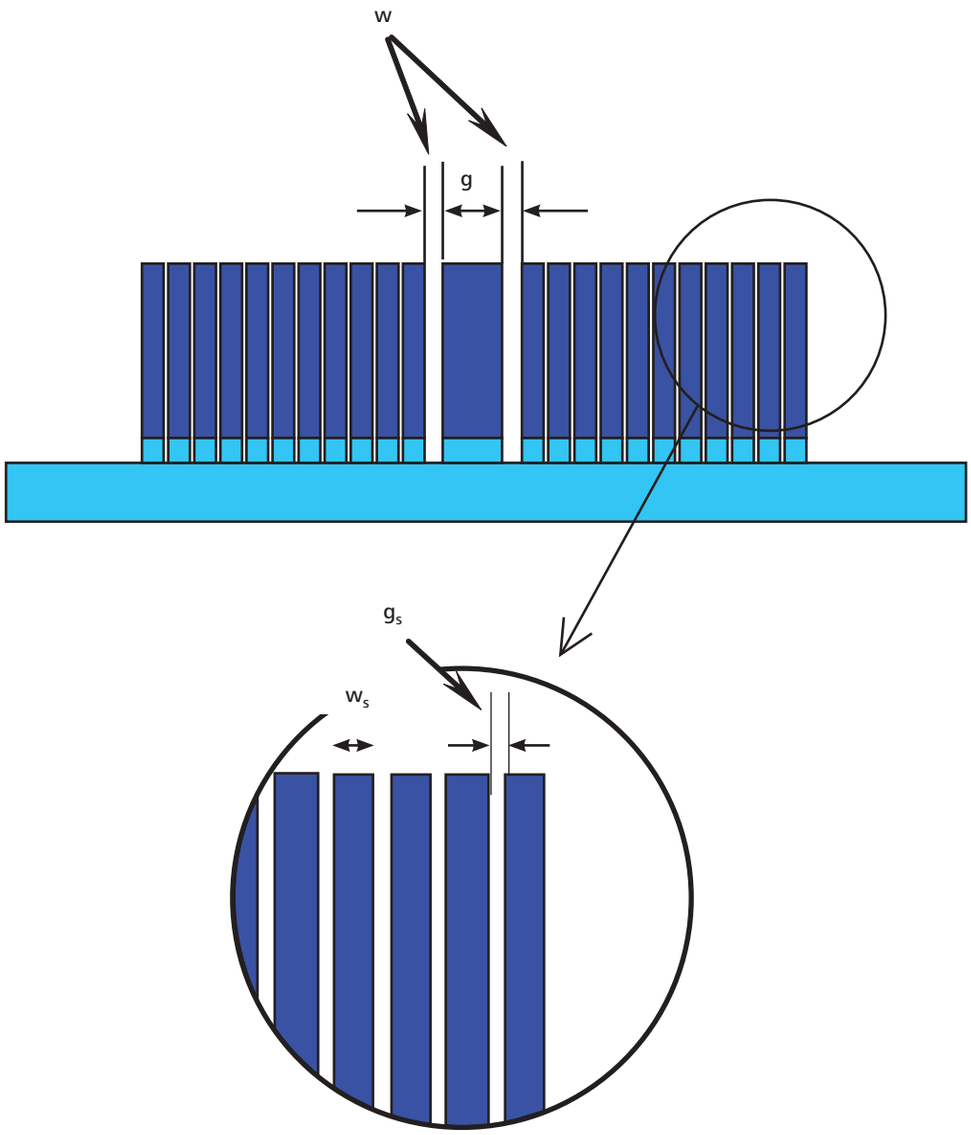

Figure 9. Parameters in the polarisation splitter design which were varied in the fabrication tolerance analysis.

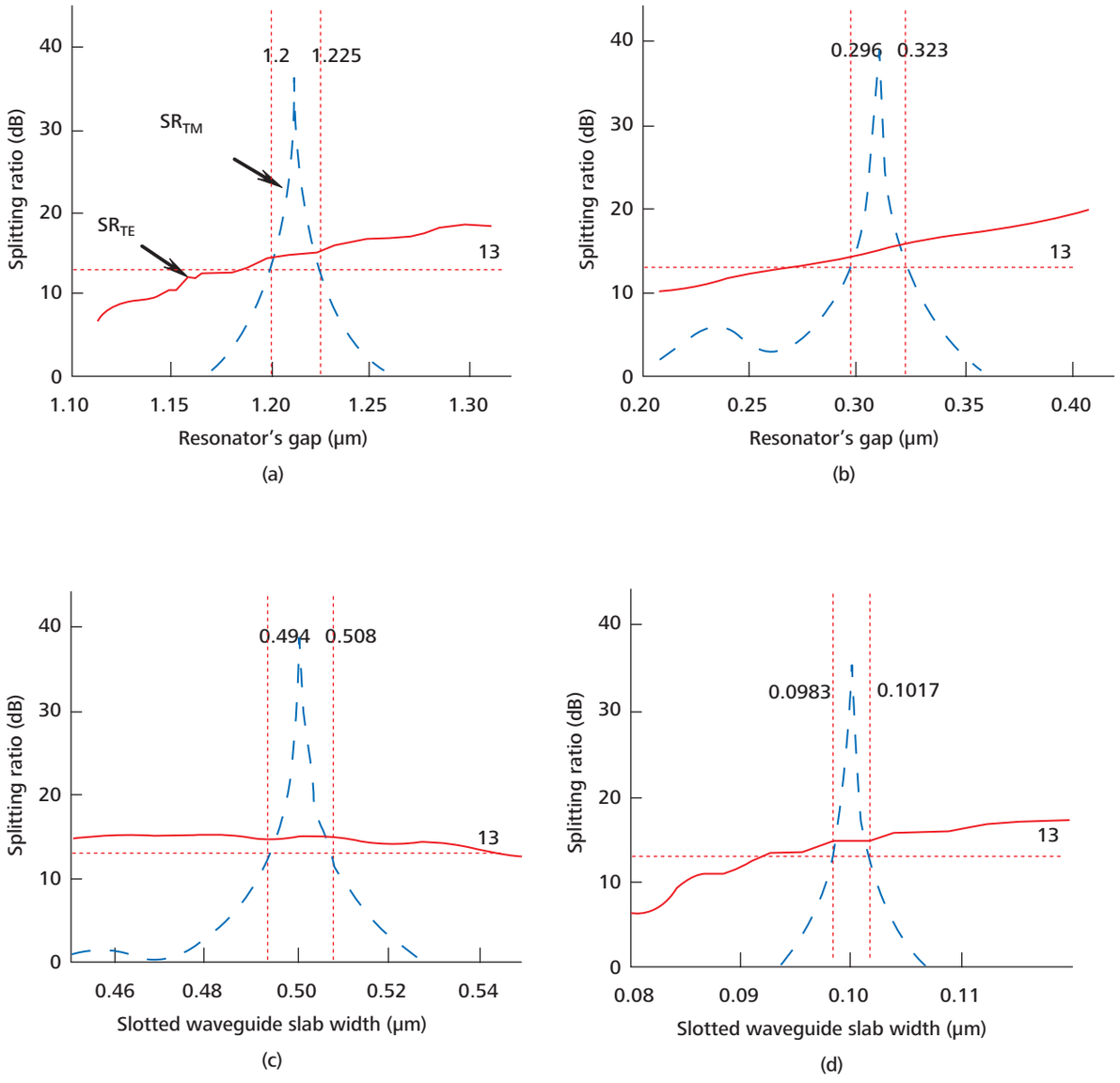

Figure 10. The splitting ratio for TM (SR_{TM}) and TE (SR_{TE}) modes computed in the fabrication tolerance of the (a) Resonator width, (b) Resonator's gap, (c) Grating waveguide slab width, and (d) Grating waveguide gap spacing. The SR value of 13 dB was the minimum acceptable SR for a practical polarisation diverse scheme.

ACKNOWLEDGMENTS

The authors would like to extend their appreciation to Universiti Sains Malaysia, Universiti Teknologi MARA and the Ministry of Science Technology and Innovation, Malaysia for the support provided in this research project (Project no. 06-01-01-SF0187).

Date of submission: April 2008
Date of acceptance: November 2008

REFERENCES

Augustin, LM, van de Tol, JJGM, Hanfoug, R, de Laat WJM, van de Moosdijk MJE, van Dijk PWL, Oek, YS & Smit MK 2007, 'A single etch-step fabrication-tolerant polarisation splitter', *J. Lightwave Technol*., vol. 25, no. 3, pp 740–746.

Bienstman, P 2007, CAMFR software, University of Ghent, Belgium , <http://camfr.sourceforge.net>.

COMSOL, Comsol AB, Stockholm, Sweden, 2008, <http://www.comsol.com>.

Donnelly, JP, Haus, HA & Whitaker, N 1987, 'Symmetric three-guide optical coupler with nonidentical center and outside guides', *IEEE J. Quantum Electron*., vol. 23, no. 4, pp 401–406.

FIMMWAVE, FIMMPROP and KALLISTOS softwares, Photon Design, Oxford, England, 2008, <http://www.photond.com>.

Hanfoug, R, van de Tol, JJGM, Augustin, LM & Smit, MK 2003, 'Wavelength conversion with polarisation labelling for rejection and isolation of signals (POLARIS)', in *Proc. 11th Eur. Conf. ECIO*, Prague, Czech Republic.

Huang, CC, Huang, CC & Twu, RC 2005, 'Polymeric three-waveguide polarisation splitter utilizing resonant tunneling effect', in *Pacific Rim Conference on Lasers and Electro-Optics*, Tokyo, Japan.

Rajarajan, M, Thermistos, C, Rahman, BMA & Grattan, KTV 1997, 'Characterization of metal-clad TE/TM mode splitters using the finite element method', *J. Lightwave Technol*., vol. 15, no. 12, pp. 2264–2269.

de Ridder, RM, Sander, AFM, Driessen, A & Fluitman, JHJ 1993, 'An integrated optic adiabatic TE/TM mode splitter on silicon', *J. Lightwave Technol*., vol. 11, no. 11. pp 1806–1811.

Soldano, LB, de Vreede, AH, Smit, MK, Verbeek, VH, Metaal, EG & Groen FH 1994, 'Mach-Zehnder interferometer polarization splitter in InGaAsP/InP', *IEEE. Photon. Technol*. *Letters*, vol. 6, no. 3, pp 402–405.

Thyagarajan, K & Pilevar, S 1992, 'Resonant tunneling three-waveguide polarization splitter', *J. Lightwave Technol*., vol. 10, no. 10, pp 1334–1337.

Yusoff, MHM, Hassan, HA, Hashim, MR & Rahman, MKA 2007, 'Compact low refractive index slotted waveguide polarization splitter based on resonant tunneling', in *Persidangan Fizik Kebangsaan 2007 (PERFIK 2007)*, Universiti Malaysia Terengganu, Kuala Terengganu.

ASM Sci. J., **2(2)**, 149–152

Distributed Feedback Er-Yb Co-doped Phosphate Fibre Laser

S.W. Harun[1*], P. Hofmann[2], A. Schülzgen[2], L. Li[2], N. Peyghambarian[2] and H. Ahmad[3]

A distributed feedback fibre laser made of highly Er-Yb co-doped phosphate glass fibre was demonstrated experimentally. The 45 mm long fibre laser device operated at 1540 nm with more than 50 dB side mode suppression ratio. However, the output power was still relatively lower due to un-optimized grating structure and thermal management.

Key words: distributed feedback; Er-Yb co-doped; phosphate; glass fibre; grating; thermal management

The high-performance, single frequency, grating-based fiber laser has gained a tremendous interest for many applications (Mackechnie *et al*. 1993; Pask *et al*. 1995). A relatively simple fabrication involving only the writing of a grating structure with ultraviolet (UV) light on to an appropriate fibre together with it's stable performance, compared to single frequency semiconductor lasers, make this device attractive. In addition, single-mode pump light can be sent into the fibre core that contains the active ions inside the laser cavity, leading to an alignment free resonator with optimum overlap of pump and signal light. To ensure robust single-frequency operation without mode hopping, the fibre laser cavity needs to be short, a few centimeters in length, at the most. Phosphate fibre is an excellent choice for the design of compact fibre amplifiers and lasers because it exhibits a high solubility for rare-earth ions. This allows a high concentration of those active-ions into a small volume of the phosphate glass. The high number density of active-ions results in small sized optical devices such as Er-Yb co-doped phosphate fibre laser (Li *et al*. 2005).

However, it has been difficult to fabricate volume gratings in the phosphate fibre with the standard UV-writing techniques used to produce Bragg gratings in silica fibres. Recently, a photosensitivity study in different phosphate glass has been reported which allows high-quality Bragg gratings to be constructed in both phosphate fibres and planar glass waveguides (Honkanen 2008). The photosensitivity of Er-Yb-co-doped phosphate glasses opens possibilities for the fabrication of Distributed Feedback (DFB) lasers. In this work, an Er-Yb co-doped phosphate DFB laser was demonstrated using a single-mode diode laser as the pump source. The laser resonator was formed by an asymmetric grating structure that provided distributed feedback for a 1540 nm signal light propagating from the single-mode core of an active Er-Yb co-doped phosphate fibre.

The configuration of the phosphate DFB laser is shown in Figure 1; it consists of a 980/1550 nm wavelength division multiplexer (WDM) coupler and a section of high concentration Er-Yb co-doped phosphate fibre (EYDPF) with an asymmetric grating structure. The grating was the wavelength selective output coupler of the laser while the Er-Yb co-doped fibre provided the gain required for laser operation. The pump sources were two laser diodes (P1 and P2) with a centre wavelength of 976 nm, which had maximum output power of 600 mW and 250 mW, respectively. Through the 980/1050 nm WDM, the pump light was coupled into the EYDPF. The output of the DFB laser was tapped from the 1550 nm port of WDM coupler and characterized by an optical spectrum analyzer (OSA) with a resolution of 0.015 nm. The EYDPF is 45 mm long with erbium and ytterbium ion doping of 1.1×10^{26} ions/m^3 and 8.6×10^{26} ions/m^3, respectively. It had a core diameter of 9 micrometer, 125 micrometer cladding diameter, and a numerical aperture of 0.12.

The DFB grating structure was written directly on to the doped single-mode fibre by exposure to 193 nm UV light through a phase mask. The grating consisted of a 20 mm and 15 mm long section at C1 and C2 sides, respectively that were separated by a 0.05 mm wide gap that created the defect state inside the grating's reflection band. The period of grating was estimated to be approximately 500 nm. The overall ~35 mm long grating structure was located approximately at the center of the active fibre piece, and the asymmetric DFB grating design resulted in unidirectional DFB laser emission. This laser could only be controlled externally by the amount of pump power that was injected

[1] Department of Electrical Engineering, University of Malaya, 50603 Kuala Lumpur, Malaysia
[2] College of Optical Sciences, University of Arizona, Tucson, Arizona 85721, USA
[3] Photonics Research Center, University of Malaya, 50603 Kuala Lumpur, Malaysia
[*] Corresponding author (e-mail: swharun@um.edu.my)

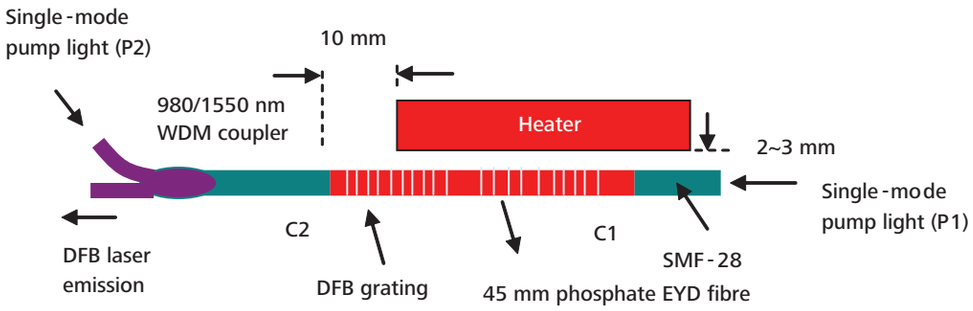

Figure 1. Experimental set-up. Splicing loss (C1→ C2) = 5 dB and (C2→ C1) 12 dB. Maximum pump power: P1 = 600 mW (@1200 mA) and P2 = 250 mW (@600 mA).

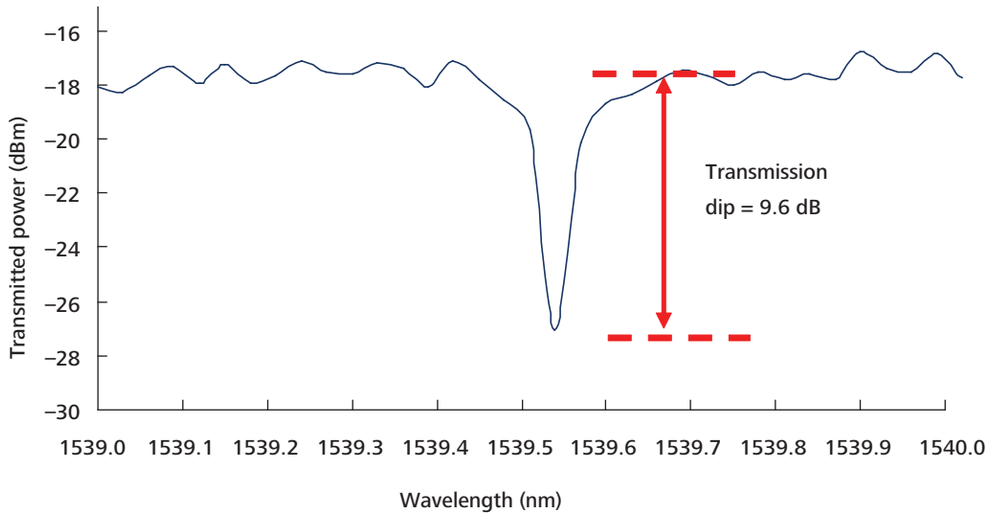

Figure 2. Transmission spectrum for the DFB grating (Maximum reflectivity = 89%).

and the temperature applied on the grating part by a heater. The heater consisted of a peltier and thermistor on a piece of metal which was controlled by ILX TEC controller. A transmittance spectrum of the gratings in the phosphate fibre is shown in Figure 2 which was measured using an erbium ASE source. The spectrum showed a transmission dip of 9.6 dB which translated to 89% reflectivity. The central wavelength of the grating was around 1539.55 nm at room temperature.

Lasing could be achieved by the pump power of at least 200 mW of P1 and 50 mW of P2 with a very precise temperature adjustment of the grating. The emission spectrum of the laser was measured by the optical spectrum analyzer as shown in Figure 3. The DFB laser emited a narrow laser line located at the grating structure design wavelength of 1540 nm. The bandwidth of line was measured to be approximately 0.02 nm, limited by the resolution of the OSA and the true emission line-width was expected to be much narrower. As shown in Figure 3, the side-mode suppression ratio (SMSR) was better than 50 dB, indicating stable single longitudinal mode operation of the DFB laser. The DFB laser only achieved the maximum power of 1.2 mW after precise adjustment of both pump powers and temperature on the grating. This low power might be due to the constructed grating which was not perfectly asymmetrical and the change of the grating spectrum by the pump power and temperature. The high splicing loss between phosphate glass and SMF also affected the attainable output power of the laser.

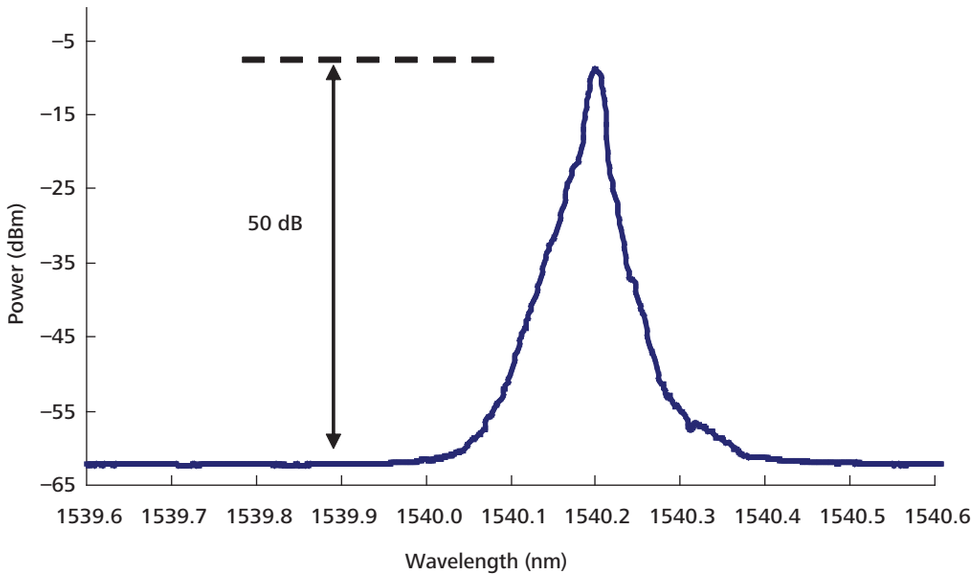

Figure 3. Emission spectrum of the core pumped DFB fibre laser measured by an optical spectrum analyzer with 0.015 nm resolution.

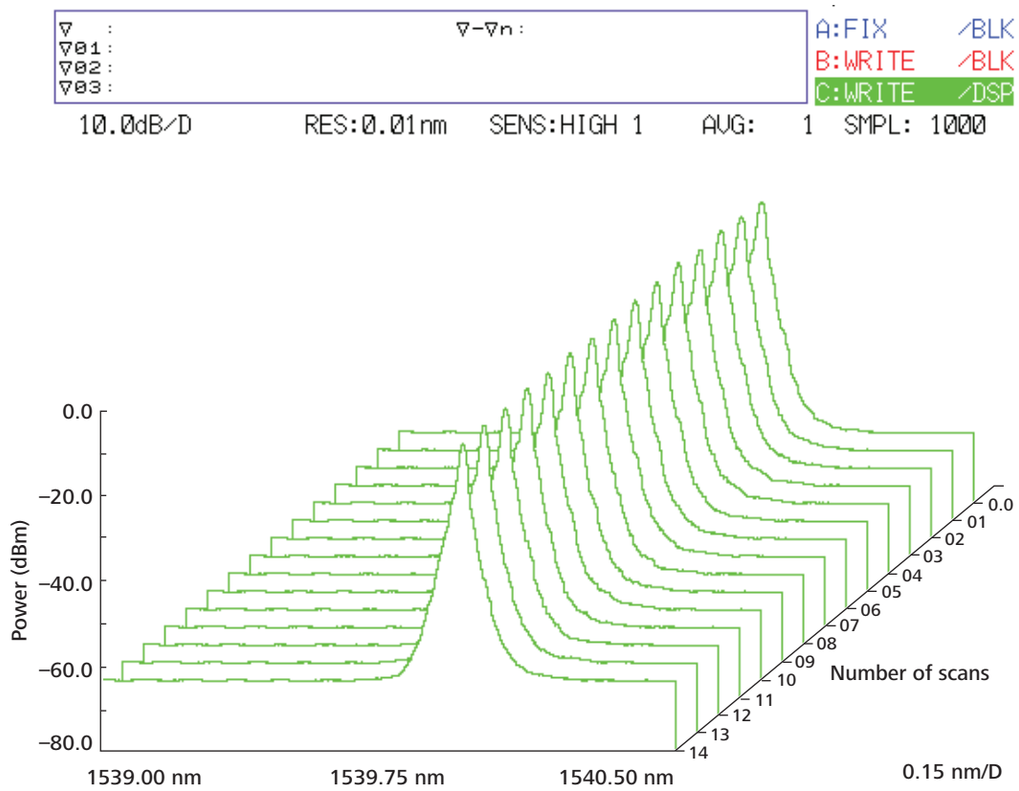

Figure 4. Laser output spectrum scanned every 10 minutes.

In order to study the lasing wavelength's stability at a fixed temperature, 14 successive scans of the system output were carried out for every 10 min and the results recorded in Figure 4. The variation in output power and emission wavelength were below 2% and 0.05 nm, respectively. Even though the achieved power level was relatively low for a fibre laser, the improvements in grating fabrication as well as temperature control set-up were expected to give a reasonably higher output power, indicating the potential of our laser scheme for the development of high-power DFB fibre lasers.

CONCLUSION

We have demonstrated a stable and compact DFB fibre laser scheme based on the Er-Yb co-doped phosphate fibre, despite the large amount of splicing loss at both ends of the doped fibre, and our relatively crude level of thermal management. A stable and narrow line-width laser was obtained at 1540 nm with SMSR of more than 50 dB by adjusting the amount of pump power that was injected and the temperature adjustment of the grating. The achieved device performance made our DFB laser a promising candidate for the fabrication of single-frequency fibre lasers that could be optimized for high-powered simple structures, compact and with low noise.

ACKNOWLEDGMENT

S.W. Harun would like to thank the Academy of Sciences Malaysia for the Post-doctoral Fellowship under the Brain-Gain Malaysia Programme.

Date of submission: June 2008
Date of acceptance: December 2008

REFERENCES

Honkanen, S, Schülzgen, A, Albert, J & Peyghambarian, N 2008, 'Photosensitivity in phosphate glasses and its use for integrated optic and fiber lasers,' in *Proc. SPIE*, vol. 6897, p. 3.

Li, L, Schülzgen, A, Temyanko, VL, Qiu, T, Morrell, MM, Wang, Q, Mafi, A, Moloney, JV & Peyghambarian, N 2005, 'Short-length microstructured phosphate glass fiber lasers with large mode areas,' *Opt. Lett*., vol. 30, no. 10, pp. 1141–1143.

Mackechnie, CJ, Barnes, WL, Hanna, DC & Townsend, JE 1993, 'High-power ytterbium (Yb^3+) doped fiber laser operating in the 1.12-mm region,' *Electron. Lett*., vol. 29, no. 1, pp. 52–53.

Pask, HM, Carman, RJ, Tropper, DC, Mackechnie, CJ, Barber, PR & Dawes, JM 1995, 'Ytterbium-doped silica fiber lasers: versatile sources for the 1–1.2-μm region,' *IEEE J. Sel. Topics Quantum Electron*, vol. 1, no. 1, pp. 2–13.

ASM Sci. J., **2(2)**, 153–161

Design of a Plastic Optical Fibre Waveguide Coupler for a Portable Optical Access Card System

A.A. Ehsan[1], S. Shaari[1] and M.K. Abd-Rahman[2]

An optical code generating device for a portable optical access-card system was constructed using the plastic optical fibre (POF) waveguide coupler. The newly constructed device provided output light intensities which were used as optical codes in a portable optical access-card system. The construction of a basic 1 × 2 waveguide design combined two major components which were the asymmetric Y-junction splitter and the linear taper. A hollow waveguide structure was utilized as it provided more flexibility in guiding light rays. A basic 1 × 2 waveguide coupler was designed using the CAD tool and then the ray was traced using the non-sequential ray tracing tool. A linear relationship between the tap-off ratio and the waveguide tap-width enabled a higher-level hollow waveguide coupler to be designed using the simple cascading technique. Construction of a 1 × 4 and higher level waveguide coupler was easily realized using the basic 1 × 2 waveguide coupler design together with a simple cascading technique.

Key words: code generating; plastic optical fibre; waveguide; coupler; hollow; cascading technique; design; access-card

Plastics optical fibre (POF) waveguide devices are a new genre of devices which have high potential usage in data communications and optical sensors. However, research was limited due to the fact that highly multimode devices have a smaller market demand due to the high attenuation of POF compared to that of glass fibre (Loch 2004). The attenuation of POF fibre at 650 nm wavelength is close to 200 dB/km whereas for single mode glass fibre, the attenuation is only 0.2 dB/km at 1550 nm (Daum *et al*. 2002).

Multimode-based components such as POF fibres have been employed for short-distance data communication and has established wide applications in multimode intensity-based sensors (Kalymious 2005). In sensor applications, POF sensors are normally used for physical or linear displacement sensors. Other application examples of the intensity-based POF sensors are detection of variation in liquid level, detection of liquid nitrogen levels, temperature sensing (Kalymious 2005), crack monitoring (Olivero 2007), monitoring dynamic response of fibre composite beam (Kuang & Cantwell 2003), automobile sensor (Polishuk 2006) and long-term environmental monitoring (Wong 2003). Nevertheless, the use of POF devices for physical access to restricted facilities have not been ventured on yet.

The applications of optical components in security-access system are known and several international patents have been issued using a variety of optical technologies but none has utilized the concept of a unique series of light-intensity from POF waveguide couplers for code generation. The application of a POF waveguide coupler design for generating a unique series of light-intensity for code generation in an access-card system is a new concept and has not been reported in any publication.

MATERIALS AND METHOD

The design of an optical code generating device utilizing large core POF waveguide coupler device for a simple access-card system is presented. The access-card would employ simple coding-decoding of a light signal transmitted from a LED or laser. The light signal was 'coded' using the 1 × M POF waveguide coupler and M was the number of output ports. The decoding of the coded signals was done at the receiving section which employed a simple receiver circuit. The 1 × M POF waveguide coupler could have a M-number of output ports and only one input port. When the light source or LED was activated, a light ray would travel from the LED into the input port of the device. The device would split the original optical power into M distinct optical power values. The output power would depend on the design of the device itself. A unique unbreakable optical code could be produced by a simple arrangement of the output power of the waveguide coupler. Figure 1 shows the concept of code generation

[1] Institute of Microengineering and Nanoelectronics (IMEN), Universiti Kebangsaan Malaysia, 43600 UKM, Bangi, Selangor, Malaysia
[2] Faculty of Applied Science, Universiti Teknologi MARA, 40450 Shah Alam, Selangor, Malaysia
* Corresponding author (e-mail: aaehsan@eng.ukm.my)

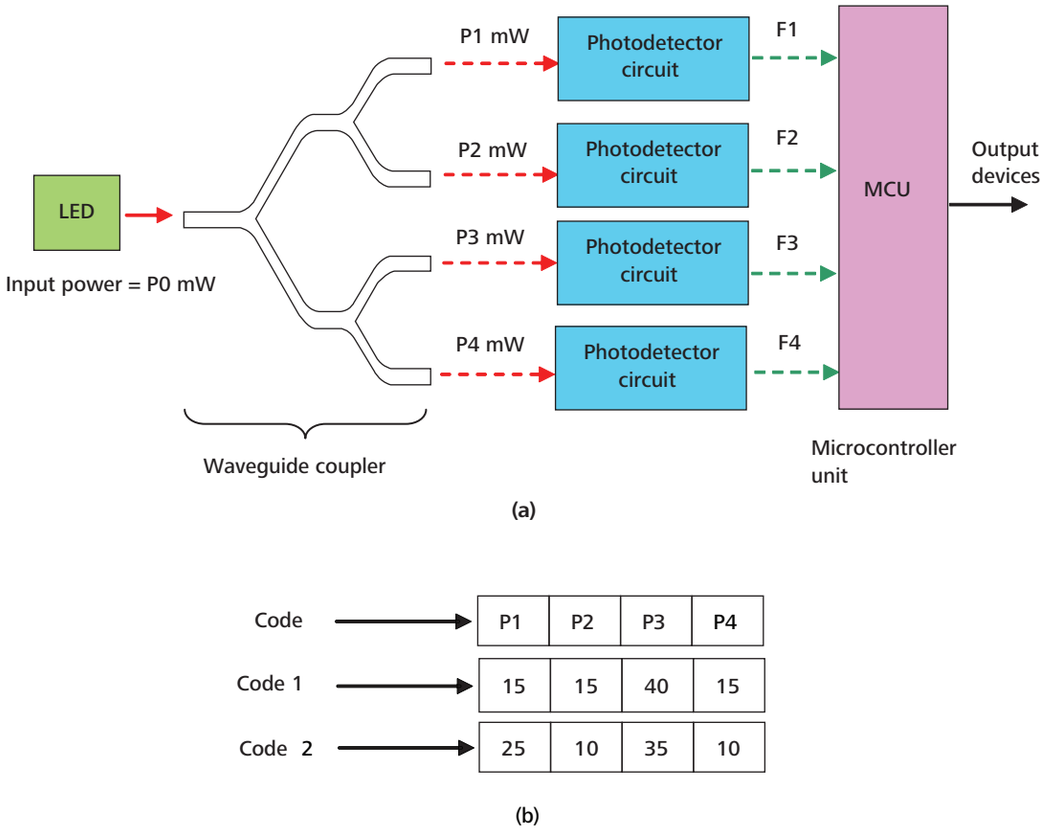

Figure 1. (a) Functional diagram of optical access-card system components with a generic 1 × 4 waveguide coupler as the code generating device (b) Examples of optical codes generated.

using a generic 1 × 4 waveguide coupler in simple optical access-card system. Two examples of the optical code are given in Figure 1, which are Code 1 and Code 2. Each of the numbers in the code series represented the output power (percentages) of the generic 1 × 4 POF waveguide coupler.

One of the important features of the POF waveguide coupler was the size of the core region. A suitable core size which allowed the coupling of the waveguide to a standard size POF fibre was chosen. The standard size of the POF fibre had a core size of 1 mm. Instead of using polymeric material for the waveguide core, a metallic hollow-type structure had been proposed for waveguiding. Light propagated along the waveguide solely by reflection on the metallic inner-surface. The hollow waveguide structure allowed more flexibility in guiding light rays without the constraint of the material's refractive index. Application of hollow waveguides structures are well know in laser light delivery system for medical applications (Hongo 2004 & Verdaasdonk; Swol 1997) where the radiation wavelengths used are greater than 2 um (Verdaasdonk & Swol 1997). The temperature insensitivity requirement was another reason why this structure is also being used for photonics integrated circuits (Miura *et al*. 2001 and Miura *et al.* 2002).

The device design was focused on three main components, namely (i) linear taper (ii) asymmetric Y-junction splitter and (iii) hollow waveguide. The use of linear taper was critical in this project as it permited the use of large core POF fibre to be coupled to the POF waveguide coupler. Figure 2 illustrates a linear taper design. The theory behind the linear taper was given by D. Israel *et al*. (1997), they showed that the power transmission of a uniform ray distribution in a linear taper, working from B to A is given by Equation 1 as follows:

$$T = \frac{w_1}{w_0} \tag{1}$$

However, reversing the direction of propagation from A to B gave no losses (Israel *et al*. 1997). This allowed the linear taper to be used precisely in the proposed device structure.

In addition to the linear taper design, another additional feature of the POF waveguide coupler was the tap-off ratio (TOFR) for an asymmetric Y-junction splitter device. The concept of TOFR was demonstrated by Henry and Love (1997) where a simple power tap can be achieved in multimode devices. This design is wavelength independent and is an ideal device for use as a low loss, low power tap in a linear taper structure.

The asymmetric Y-Junction splitter with TOFR and linear taper is shown in Figure 3. An input beam ray entered the device at Port 1 where at the tap-off region or tap line, a portion of this beam was tapped-off and the remaining portion stayed in the bus line. The TOFR or the ratio of the power exiting through Port 2 to the total power incident in the bus Port 1 is given by Equation 2 below (Henry & Love 1997):

$$\text{TOFR} = \frac{Y}{Y + X} \tag{2}$$

Now, at the end of the tap-off region, there was a linear taper which expanded the size of the channel, from Y mm to X mm, where the core size increased back to X mm which was the size of the bus line. The reason behind this was that the waveguide could be coupled to the same POF fibre (for example, a 1 mm core size POF fibre) at all the input and output ports. Using this concept, a simple 1 × 2 waveguide coupler had been designed which included an asymmetric Y-junction splitter and a linear taper. In this design, the main bus line's width would be fixed at 1 mm while the tap line's width varied depending on the TOFR requirements. Figure 4 illustrates our simple 1 × 2 POF waveguide coupler.

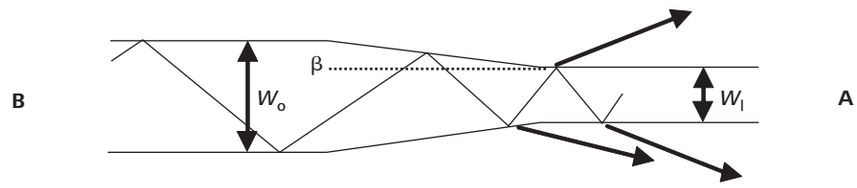

Figure 2. Linear taper where the waveguide width is reduced from w_o to w_1 (Israel *et al*. 1997).

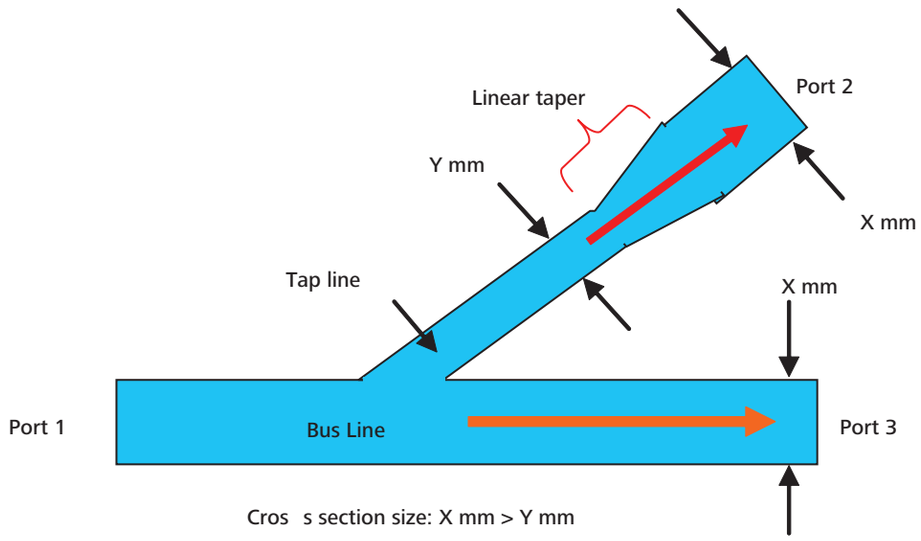

Figure 3. Asymmetric multimode Y-junction splitter with bus and tap lines.

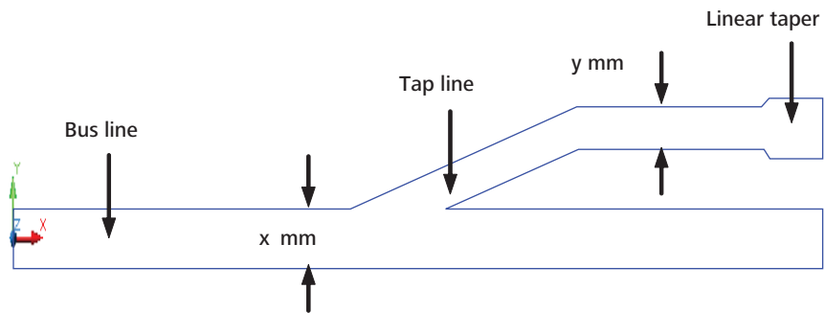

Figure 4. 1 × 2 POF waveguide coupler design with different tap line (y) and bus line (x).

We could generate several types of asymmetric waveguide coupler with any combination of splitting ratio by applying the concept structure as in Figure 4. This paper will illustrate some of the waveguide coupler designs for 1 × 2 and 1 × 4 couplers.

1 × 2 POF Waveguide Coupler

The simplest coupler design would be a 1 × 2 POF waveguide coupler. We set one branch to be the main bus line which had a core size of 1 mm. Another branch would be the tap line whereby changing the tap line core width, any combination of output power at the two branches could be obtained. Figure 5 shows examples of the 1 × 2 asymmetric waveguide design with different tap line sizes. Three different tap line sizes are shown, which are 50%, 41% and 32% TOFR. These correspond to tap width (y) of 1 mm, 0.7 mm and 0.55 mm, respectively.

1 × 4 POF Waveguide Coupler

The construction of a 1 × 4 POF waveguide coupler was easily done by utilizing the preceding 1 × 2 POF waveguide coupler design. A simple 1 × 2 Y-junction splitter was cascaded with two 1 × 2 POF waveguide couplers. The concept of cascading the designs is shown in Figure 6.

Waveguiding in the POF waveguide coupler design was achieved by using a hollow waveguide structure. Here, instead of using polymeric material for the waveguide core, the core of the waveguide would be hollow (air). Light propagated along the waveguide solely by reflection on the metallic inner-surface. The hollow waveguide structure allowed more flexibility in guiding light rays without the constraint of the material's refractive index.

The modeling block for the hollow waveguide structure was designed by building a rectangular block and inserting a 3D waveguide coupler design into it. The inserted 3D object was then subtracted from the main rectangular block. Figure 7 illustrates how a 1 × 2 hollow POF waveguide coupler is constructed from a 2D waveguide design by subtracting the 3D structure from a rectangular block. Similarly, a 1 × 4 hollow POF waveguide coupler was constructed from its 2D waveguide design by subtracting its 3D structure from a rectangular block.

The fabrication process of the waveguide coupler would utilize the micro-engraving technique which was a simple and low-cost fabrication process. In this process, a rigid mould insert was designed and fabricated using a micro-engraving tool. The limits of this mechanical technique was currently up to about 100 μm, i.e. conventional CNC micro-milling (Albers & Marz 2005). Once the mould insert had been fabricated, another metallic block was stamped onto and both were welded together. Hence, multimode devices, especially POF devices, could be fabricated easily using the micro-milling technique. This technique was a maskless process and mould inserts could be easily and quickly produced.

RESULTS AND DISCUSSION

The modeling and simulation of the POF waveguide coupler was done using non-sequential ray tracing in Zemax. Ray tracing allowed the optical performance and code combination generation of the waveguide design to be forecasted. The non-sequential ray tracing was done using the 3D design of the hollow waveguides in Figures 7 and 8. In order to make the hollow waveguide to reflect light rays all the way from the input port to the output ports, the inner surface of the waveguide was defined as reflective and the coating was written as metal coating. The wavelength used in this simulation was 650 nm, with an input power of 1.0 mW. Another feature of this waveguide structure was that it is operated unidirectionally only.

The ray tracing diagram of the waveguide coupler is shown in Figure 9 for a 1× 2 POF waveguide coupler

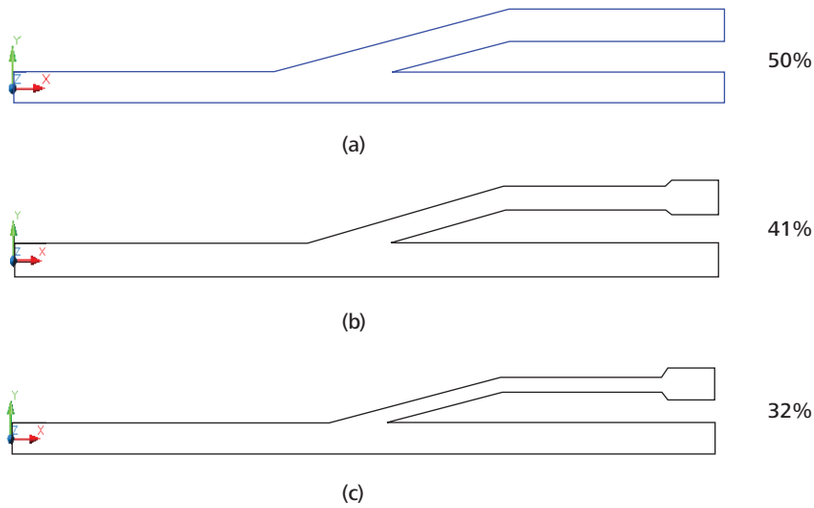

Figure 5. 1 × 2 POF asymmetric waveguide coupler: (a) 50% TOFR; (b) 41% TOFR and (c) 32% TOFR.

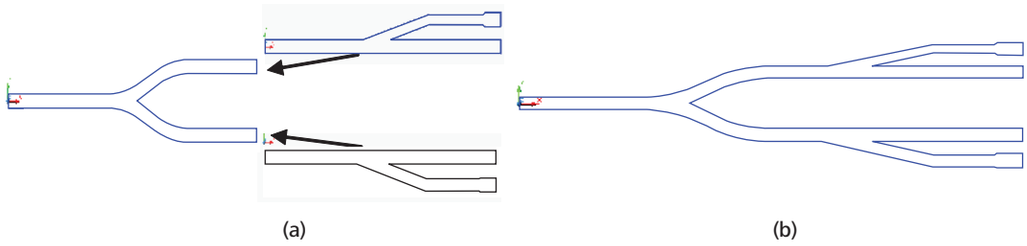

Figure 6. Higher-level waveguide design: (a) 1 × 2 Y-junction splitter before joining with two 1 × 2 POF waveguide couplers and (b) 1 × 4 POF waveguide couplers with asymmetric branches.

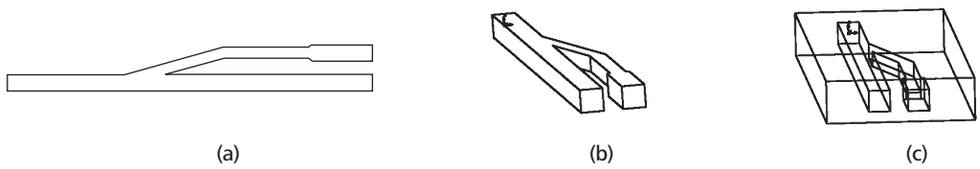

Figure 7. 1 × 2 hollow POF waveguide coupler: (a) 2D layout; (b) 3D layout and (c) 3D hollow structure.

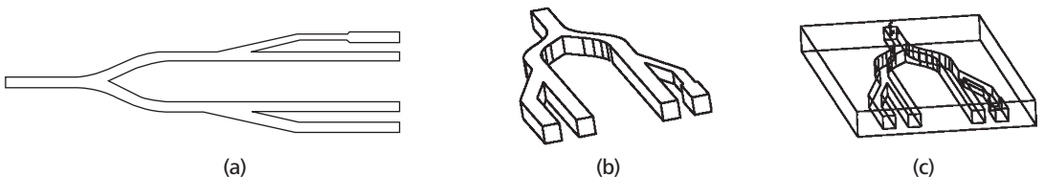

Figure 8. 1 × 4 hollow POF waveguide coupler: (a) 2D layout; (b) 3D layout and (c) 3D hollow structure.

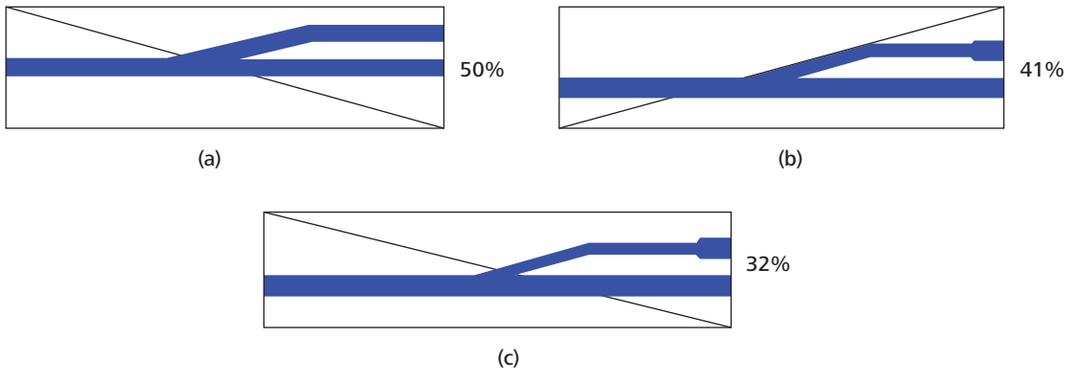

Figure 9. Ray tracing of 1 × 2 POF waveguide coupler: (a) 50% TOFR; (b) 41% TOFR and (c) 32% TOFR.

design. The ray tracing showed the design for 50%, 41% and 32% TOFR. Light which entered the input port of the waveguide was totally reflected at the inner-wall of the hollow waveguide. Photodetectors were positioned at the output ports of the waveguide to allow the values of the output light intensities at both the bus and tap lines to be measured.

Some other TOFR values were tested for the 1 × 2 coupler design. The results for the TOFR against the tap line width are given in Figure 10. Tap widths of 250 µm up to 1 mm were used for TOFR of 5% until 50%. The linear relationship between the TOFR and the tap width enabled a higher-level 1 × M POF waveguide coupler to be constructed.

The modeling and ray tracing of the 1 × 4 POF waveguide coupler was done by first partitioning the device, which is shown in Figure 11. The device structure was partitioned into six sections as shown in the figure. A simple 50% split was achieved using a Y-splitter (section A and B). If the input power was label P_o, then A and B would have output power of 0.5 P_o. Once the power was split by 50% at these two sections, the asymmetric coupler design in section C, D, E and F would split the 0.5 P_o into smaller fractions of the optical power, based on the actual design of the 1 × 2 POF waveguide coupler. In this example, sections C and D were part of the 1 × 2 POF waveguide coupler design using a 50:50 ratio design with a tap core width of 1000 µm. In addition, sections E and F were part of the 1 × 2 POF waveguide coupler design using 32:65 ratio design (32 and 65 were values obtained from the Zemax ray tracing for a 1 × 2 waveguide coupler). The tap core width (E) was 700 um.

For example, in section C (tap), the output power detected (as a fraction of the input power) would be:

$$\text{P out (C)} = \frac{50}{100} \times 0.5\, P_o = 0.25\, P_o \qquad (3)$$

The design and the simulation results for the five sets of 1 × 4 POF waveguide couplers are shown in Tables 1, 2, 3, 4, and 5 (P_o = 1 mW). The design values were based on the simple arithmetics shown in Equation 3 while the simulation values were values obtained in Zemax. For an example, in Table 1 the 1 × 4 POF coupler was based on a 1 × 2 asymmetric coupler with tap width of 900 µm (C) and 700 µm (E). The bus line width for both 1 × 2 asymmetric couplers was set at 1000 µm. Similarly in Table 2, tap width was 500 µm (C) and 500 µm (E). In Table 3, tap width was 1000 µm (C) and 700 µm (E). In Table 4, tap width was 600

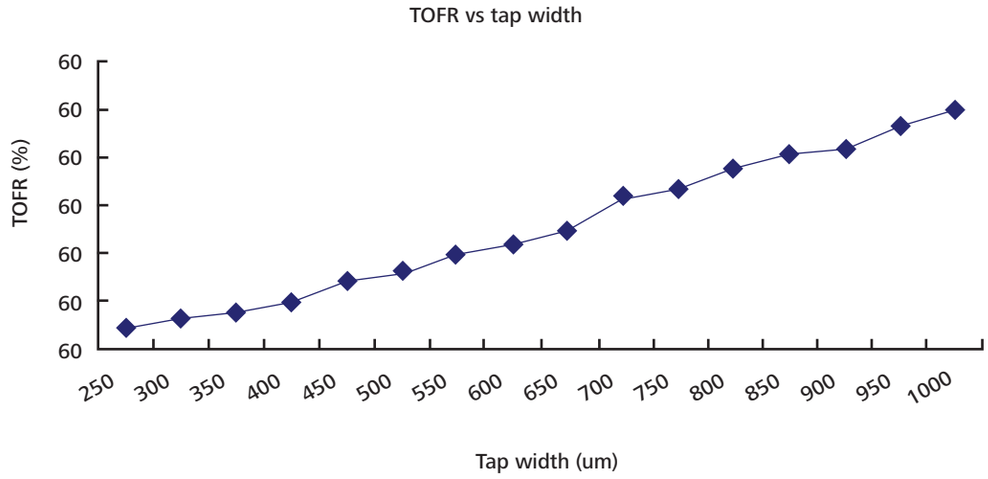

Figure 10. TOFR versus Tap (Line) Width for a 1 x 2 POF waveguide coupler (Simulation)

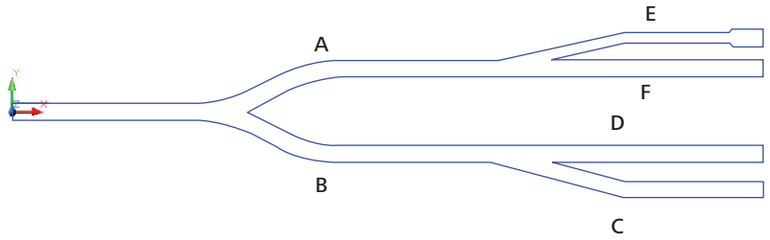

Figure 11a. Partitioning the 1 x 4 POF waveguide coupler.

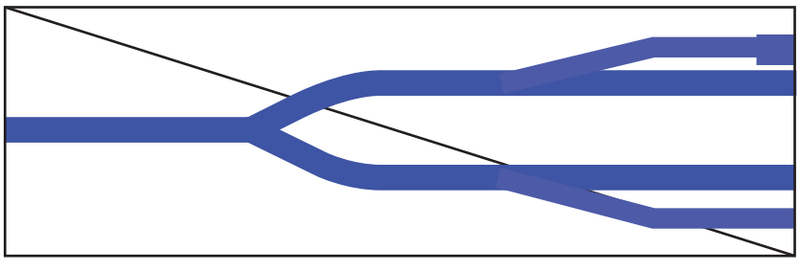

Figure 11b. Ray tracing of a 1 × 4 POF waveguide coupler.

μm (C) and 800 μm (E). In Table 5, tap width was 1000 μm (C) and 500 μm (E).

The results demonstrated that the Y-junction splitter section of this device split the power evenly. In addition, each of the 1 × 2 POF waveguide couplers split the incoming power from the Y-branch splitter appropriately based on the TOFR-Tap width design rule, as illustrated in Tables 1 to 5. These tables show the design examples for 1 × 4 POF waveguide coupler design, demonstrating the designed and simulated effective power values at the output ports. As per design, each of the simulated output ports corresponded close to the required design value. The technique indicated that a higher and more complex POF waveguide coupler design could be constructed using this simple cascaded design technique.

Table 1. 1 × 4 POF coupler design 1.

Design				Simulation			
C	D	E	F	C	D	E	F
0.2 P_o	0.28 P_o	0.15 P_o	0.32 P_o	0.22 P_o	0.27 P_o	0.15 P_o	0.32 P_o

Table 2. 1 × 4 POF coupler design 2.

Design				Simulation			
C	D	E	F	C	D	E	F
0.08 P_o	0.38 P_o	0.08 P_o	0.38 P_o	0.08 P_o	0.39 P_o	0.08 P_o	0.39 P_o

Table 3. 1 × 4 POF coupler design 3.

Design				Simulation			
C	D	E	F	C	D	E	F
0.25 P_o	0.25 P_o	0.15 P_o	0.32 P_o	0.3 P_o	0.2 P_o	0.15 P_o	0.32 P_o

Table 4. 1 × 4 POF coupler design 4.

Design				Simulation			
C	D	E	F	C	D	E	F
0.11 P_o	0.37 P_o	0.18 P_o	0.31 P_o	0.12 P_o	0.39 P_o	0.17 P_o	0.28 P_o

Table 5. 1 × 4 POF coupler design 5.

Design				Simulation			
C	D	E	F	C	D	E	F
0.25 P_o	0.25 P_o	0.08 P_o	0.38 P_o	0.26 P_o	0.22 P_o	0.08 P_o	0.4 P_o

CONCLUSION

The designs of 1 × 2 and 1 × 4 POF waveguide couplers for a portable optical security access-card system were presented. These optical code generating devices were constructed using a combined structure of asymmetric Y-junction splitter and linear taper. The newly constructed devices provided a unique series of output light intensities which were successively used as an optical code in a portable optical access-card system. Waveguiding in these waveguides was done using hollow waveguide structure. Starting with a basic 1 × 2 waveguide coupler design, a 1 × 4 waveguide coupler was constructed by a simple cascade of a Y-junction splitter with two 1 × 2 waveguide couplers. Non-sequential ray tracing of the POF waveguide couplers were performed to predict the optical performances of the actual device. The simulation results showed a linear relationship between the tap-off ratio and the waveguide tap width.

ACKNOWLEDGEMENT

The authors would like to thank Universiti Teknologi MARA for the financial support towards this project (01-01-01-SF0197) and to the Institute of Micro-engineering and Nanoelectronics (IMEN), Universiti Kebangsaan Malaysia for providing the simulator tool Zemax.

Date of submission: September 2008
Date of acceptance: November 2008

REFERENCES

Albers, A & Marz, J 2005, 'Design environment and design flow', in *Advanced Micro and Nanosystems — Microengineering of metals and ceramics: part 1 – design, tooling and injection molding*, eds D Lohe & J Haufbelt, Wiley-VCH, Verlag, Germany, pp.16.

Daum, W, Krauser, J, Zamzow, PE & Ziemann, O 2002, *POF – Polymer optical fibers for data communication*, Springer-Verlag, Berlin, Germany.

Henry, WM & Love, JD 1997, 'Asymmetric multimode Y-junction splitters', *Journal of Optical and Quantum Electronics*, vol. 29, no. 3, pp. 379–392.

Hongo, A, Koike, T & Suzuki, T 2004, 'Infrared hollow fibers for medical applications', *Hitachi Cable Review*, vol. 23, pp. 1–5.

Israel, D, Baets, R, Goodwin, MJ, Shaw, N, Salik, MD & Groves-Kirkby, CJ 1997, 'Multimode polymeric Y junctions for star couplers in backplane optical interconnect', *Applied Optics*, vol. 36, no. 21, pp. 5091—5096.

Kalymious, D 2005 'Plastic optical fibres (POF) in sensing — current status and prospects', in *17th International Conference on Optical Fibre Sensors:Proceedings of SPIE, Bruges, 23rd – 27th May 2005*, Bruges.

Kuang, KSC & Cantwell, WJ 2003, 'The use of plastic optical fibre sensors for monitoring the dynamic response of fibre composite beams', *Measurement Science Technology*, vol. 14, pp. 736–745.

Loch, M 2004, 'Plastic optical fibers: properties and practical applications', in *Optical transmission systems and equipment for WDM networking III: Proceedings of SPIE*, vol. 5596, pp. 299–308.

Miura, T, Koyama, F, Aoki, Y, Matsutani, A & Iga, K 2001, 'Hollow optical waveguide for temperature-insensitive photonic integrated circuit', *Japanese Journal of Applied Physics*, vol. 40, part 2, no. 7A, pp. L688–L690.

Miura, T, Koyama, F & Matsutani, A 2002, 'Modeling and fabrication of hollow optical waveguide for photonic integrated circuits', *Japanese Journal of Applied Physics*, vol. 41, part 1, no. 7B, pp. L4785–L4789.

Olivero, M, Perrone, G, Vallan, A & Abrate, S 2007, 'Plastics optical fiber displacement sensors for cracks monitoring', *Key Engineering Materials*, vol. 37, pp. 487–492.

Polishuk, P 2006, 'Automotive Fiber: Plastic optical fiber builds on MOST success', *Laser Focus World Magazine*, vol. 42, no. 3, pp. 57–59.

Sugihara, O, Mizuno, H, Jordan, S, Kaino, T, Okamoto, N & Oohama, M 2004, 'Passive alignment structure: simple fabrication of polymeric optical waveguide with POF guides', in *Proceedings of the 13th International Plastic Optical Fibres Conferences, Nurnberg, 27th–30th September 2004*, Nurnberg.

Verdaasdonk, RM & Swol, CFP 1997, 'Laser light delivery systems for medical applications', *Physical Medical Biology*, vol. 42, pp. 869–894.

Wong, YM, Scully, PJ, Bartlett, RJ, Kuang, KSC & Cantwell, WJ 2003, 'Plastic optical fibre sensors for environmental monitoring: biofouling and strain applications', *International Journal for Experimental Mechanics:Strain*, vol. 39, no. 3, pp. 115.

ASM Sci. J., **2(2)**, 163–168

Er^{3+}/Yb^{3+} Co-doped Fibre Amplifier Demonstrates Significant Gain Enhancement with Improved Noise Figure

S.Z. Muhd-Yassin[1]* S.W. Harun[2], H. Ahmad[3] and M.K. Abd-Rahman[1]

An efficient erbium/ytterbium co-doped fibre amplifier was demonstrated by using a dual-stage partial double-pass structure with a band-pass filter (BPF). The amplifier achieved the maximum small signal gain of 56 dB and the corresponding noise figure of 4.66 dB at 1536 nm with an input signal power and total pump power of –50 dBm and 140 mW, respectively. Compared with a conventional single-stage amplifier, the maximum gain enhancement of 16.99 dB was obtained at 1544 nm with the corresponding noise figure was improved by 2 dB. The proposed amplifier structure only used a single pump source with a partial double pass scheme to provide a high gain and dual-stage structure to provide the low noise figure.

Key words: EYDFA; ytterbium; fibre amplifier; dual stage; partial double-pass filter; low noise

The demand for a compact and efficient optical amplifier with a short fibre gain medium led to the development of the erbium/ytterbium co-doped fiber (EYDF) (Sudo *et al*. 1997, Grubb *et al*. 1992). An EYDF utilizes ytterbium ions as a co-dopant to provide an intermediate medium for the transfer of pump energy to the erbium ions. As the intermediate medium, the ytterbium ions are first pumped at the absorption wavelength of 800 nm – 1100 nm to the $^2F_{5/2}$ state (Gapontsev 1992). The energy of the ytterbium ions is then transferred to the erbium ions which are in turn excited to the $^4I_{11/2}$ state. The excited erbium ions subsequently undergo a non-radiative transition to the metastable state, $^4I_{13/2}$ and form a population inversion with the ground state, $^4I_{15/2}$. Once the population inversion has been achieved, any incident optical signal traveling through the fibre is amplified via stimulated emission between these two states.

The EYDF is capable of overcoming the erbium ion concentration limit of conventional erbium-doped fibres (EDFs). In a typical EDF, the erbium ions will cluster together once a dopant threshold is met. When subjected to lasing, these clustered ions will undergo an undesirable effect known as pair-induced quenching (PIQ), reducing the amount of stimulated emission in the fibre. As such, PIQ imposes a concentration limit that restricts the amount of lasing ions available for amplification, which is a significant drawback for conventional EDF amplifier systems. In an EYDF however, highly doped ytterbium ions act as ionic buffers that effectively surround the erbium ions due to their similar atomic radius. This reduces the clustering and subsequently the PIQ effect between erbium ions and allows for ion doping concentrations of up to 1000 p.p.m. (Park *et al*. 1996). The energy transfer efficiency from the pump to the erbium ions further increases with the right ratios of ytterbium ions (Layne *et al*. 1977). In comparison to an EDF amplifier, an EYDF amplifier can achieve the same signal amplification with higher pump efficiency by using a shorter length of doped fibre. An EYDFA also has the benefit of a wide pump absorption band, which enables extended range of pump laser wavelengths.

Besides compactness, the EYDFA also provides high levels of small signal gain for application in pre-amplifiers and inline amplifiers in order to amplify weak signals before photo-detection at the receiver or before the next span in a fibre link. In our previous report, a significant improvement of the gain and noise figure was demonstrated in EYDFA by employing a dual-stage structure (Harun *et al*. 2007). However, the dual-stage structure had a low gain efficiency that uses two pump sources to provide pumping for each of the stages (due to high ytterbium absorption of 64 dB/m at 1057 nm). An efficient EYDFA with high small signal gain was later demonstrated using a double-pass structure. (Harun *et al*. 2007). This double-pass structure was able to improve the EYDFA gain efficiency, at the expense of a higher noise figure. In this paper, a new EYDFA architecture which combined both architectures was proposed to further improve the amplifier performance. The proposed amplifier used a single pump source with a partial double-pass

[1] Faculty of Applied Science, Universiti Teknologi MARA, Shah Alam, Selangor Malaysia
[2] Dept. of Electrical Eng., Faculty of Engineering, University of Malaya, 50603 Kuala Lumpur, Malaysia
[3] Photonics Laboratory, Department of Physics, University of Malaya, 50603 Kuala Lumpur, Malaysia
* Corresponding author (e-mail: spzen98@yahoo.com)

structure and band-pass filter to provide high gain as well as a dual-stage structure to provide the low noise figure.

EXPERIMENTAL SETUP

Figure 1(a) shows the configuration of the proposed dual-stage partial double-pass EYDFA. It used an EYDF of 1 m and 3 m at the first and second stages, respectively as the gain medium. A shorter EYDF length was located at the first stage to ensure sufficient excess pump power to the second stage and also to sequentially minimize the ASE induced saturation from the forward ASE. Instead of a single pass of the signal through the second stage, a forward double-pass configuration was set up at the second stage so that the signal experienced extra amplification along the same fibre. The forward pumped double pass scheme was selected due to its better performance as obtained in previous works (Wysocki *et al*. 1996). An optical circulator, OC1 was used to route the signal into the second stage (from Port 1 to Port 2). A second optical circulator, OC2, redirected the light back to the amplifier (from Port 1 to Port 2 and from Port 2 to Port 3) in order to create the double pass at the second stage. The light signal then passes through OC1 from Port 2 to Port 3 to redirect the amplified signal away from the first stage. A band-pass filter (BPF) with 0.5 nm at 3 dB bandwidth was incorporated between Port 3 and Port 1 of OC2 to block some portion of the forward ASE from depleting the inversion level during the second pass. An isolator placed at the beginning of the amplifier prevented light from entering the signal source (TLS). A 1057 nm laser diode was used to create the required ion excitation throughout the whole EYDF and the excess pump beam from the first stage was routed to the second stage via two wavelength selective couplers (WSCs) located before and after OC1. The amplifier performance for a conventional single-stage and conventional dual-stage amplifier was also measured for comparison purposes. Both conventional dual-stage and single-stage amplifier were constructed by using a 140 mW forward pumped 4 m EYDF. The dual-stage structure is shown in Figure 1(b). The single-stage structure are built based on the typical forward pumped single-stage EYDFA (Harun 2006). The results were also compared with the previously reported double-pass amplifier (Wysocki *et al.* 1996).

RESULTS AND DISCUSSIONS

Figure 2 shows the gain and noise figure evolution against pump power for different configurations of EYDFA. In the experiment, the input signal power and wavelength were fixed at –50 dBm and 1536 nm, respectively. In order to prevent random laser oscillation inside the double-pass system, the maximum pump power had to be limited to a maximum of 60 mW (Yassin 2008). However, random laser oscillations were totally suppressed in the proposed dual-stage partial double-pass system. This could be attributed

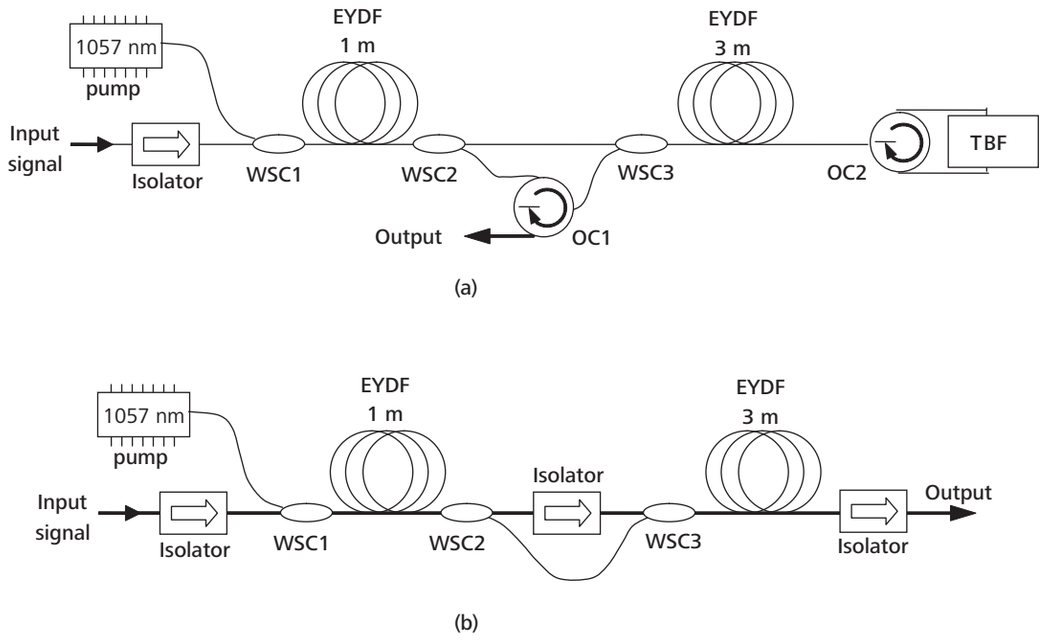

Figure 1. Schematic diagram of (a) proposed dual-stage partial double-pass structure and (b) Conventional dual-stage structure.

to the injected signal from the first stage being dominantly large enough to suppress the self lasing effect once it entered the double-pass structure of the second stage. As shown in Figure 2, the gain of both the proposed and conventional double pass amplifiers improved significantly as the pump power exceeds 30 mW as compared to the single and dual-stage amplifiers. This was due to the efficient utilization of pump power by the double-pass structure as the signal would propagate twice inside the EYDF. The gain of the proposed partial double-pass amplifier was further improved due to the inclusion of the TBF which acted to filter out the forward ASE of the second stage.

It was also observed that the noise figure of the proposed amplifier closely followed the noise figure pattern of the dual stage amplifier. The low-noise figure was attributed to the high population inversion at the first stage, which had a single-pass structure. The dual-stage configuration also contributed to a lower noise figure due to the mid-way circulator which prevented the backward ASE of the second stage from entering the first stage. This strong ASE could reduce the population inversion at the input parts of the amplifier and increase the noise figure observed in the conventional double-pass system. A maximum gain of 56 dB was obtained with the proposed dual-stage partial double-pass amplifier at a maximum pump power of 140 mW as shown in Figure 2 while the noise figure was below 5 dB at pump powers above 30 mW.

Figure 3 compares the gain spectra of the proposed dual-stage partial double-pass amplifier with the dual-stage and conventional single-stage EYDFA configurations. The input signal and pump powers was set at –50 dBm and 140 mW, respectively. Beyond this point, the pump power was maintained at 140 mW. The proposed amplifier achieved a maximum gain of 56 dB at an input signal wavelength of 1536 nm. Moreover, the gain spectrum showed gains of over 20 dB across the 30 nm bandwidth of the input signal from 1530 nm to 1560 nm. At an input signal wavelength of 1544 nm, a gain enhancement of approximately 17 dB and 14 dB were observed by the proposed EYDFA as compared to the conventional single-stage and dual-stage EYDFAs, respectively. The greatest gain enhancement at the respective wavelength (1544 nm) could be attributed to the least difference possible in the absorption and emission cross section of the EYDF. The gain in the dual-stage structure was further enhanced by OC1 which was used to block the backward ASE at the second stage from depleting the inversion level of the input end, while OC2 provided a further gain improvement when the signal was amplified twice along the second stage. The incorporation of BPF between ports 3 and 1 of the OC2 also contributed to the improvement of the gain because a large portion of forward ASE from the second stage was blocked by the BPF. This minimized the self-saturation effect at the output end during the second pass, which in turn increased the total population inversion which subsequently contributed to the improvement of the gain and noise figure.

Figure 4 illustrates the noise figure spectrum of the different EYDFA configurations. As shown in Figure 4, the proposed dual-stage partial double-pass amplifier shows a significant noise figure improvement of 2 dB at a 1536 nm input signal wavelength as compared to the conventional

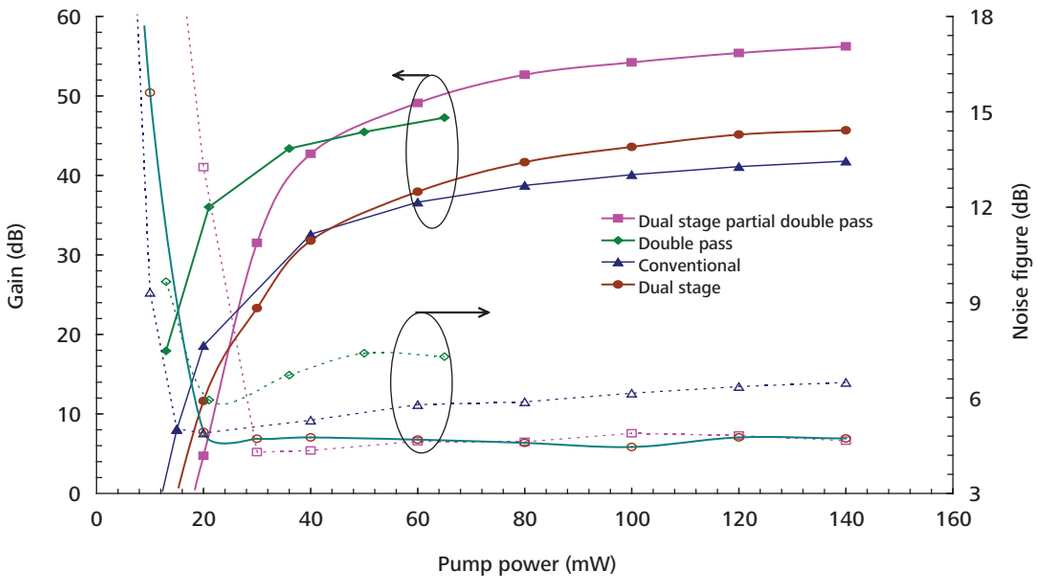

Figure 2. Gain and noise figure of a 1536 nm signal against different pump powers for different EYDFA configurations at –50 dBm input signal power. Gain is represented by solid symbols, while the noise figure is represented by hollow symbols.

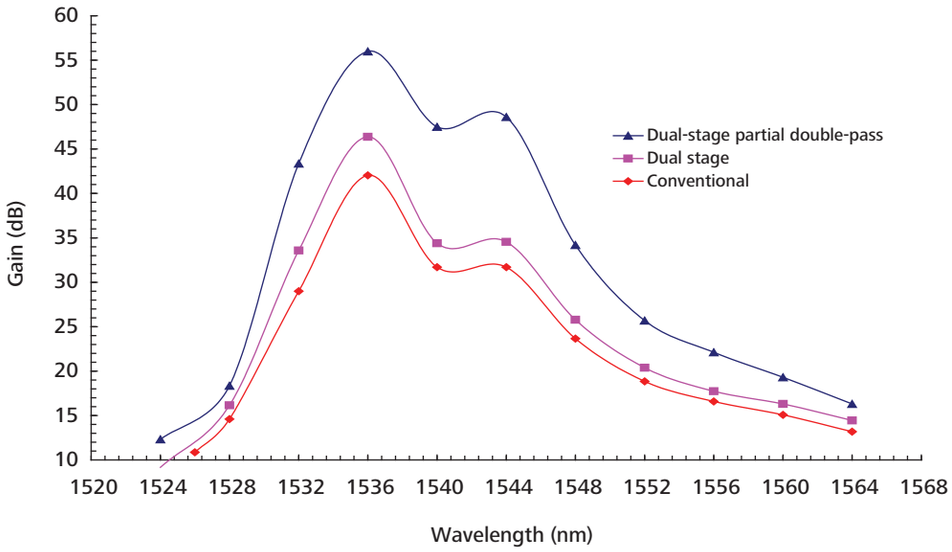

Figure 3. Gain spectra of the dual-stage partial double-pass, dual-stage and conventional EYDFA configurations. Input signal power = –50 dBm.

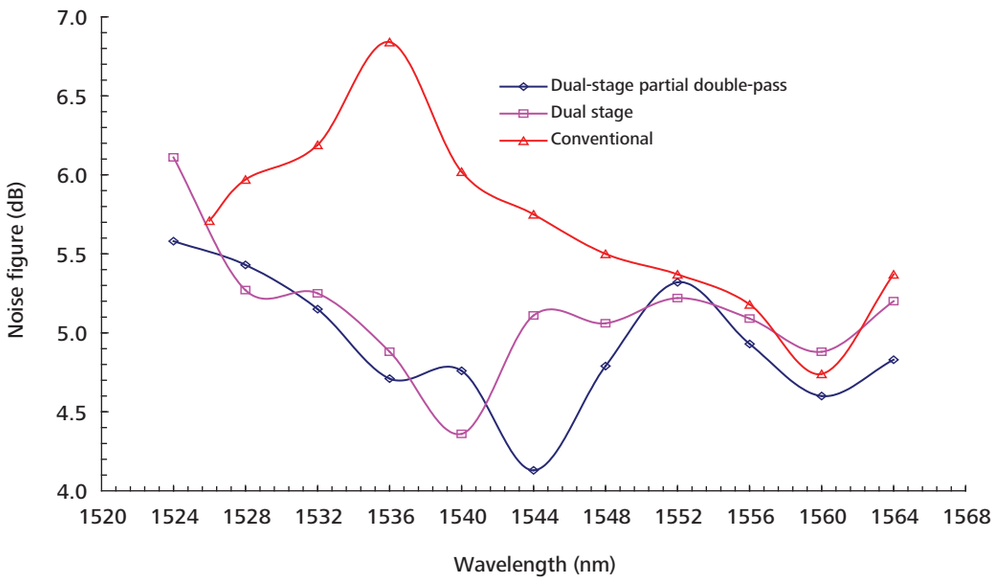

Figure 4. Noise figure spectra of the dual-stage partial double pass, dual-stage and conventional EYDFA configurations. Input signal power = –50 dBm.

EYDFA. At a 1544 nm input signal wavelength, the proposed amplifier showed a low noise figure of 4.1 dB which was near the quantum limit (Wysocki *et al*. 1996). This outstanding performance was attributed to the amplifier structure that utilized the dual-stage configuration in conjunction with the short forward pumped EYDF length at the first stage which increased the population inversion at the input part of amplifier and minimized the noise figure. The use of the short EYDF length at the first stage provided a very high population inversion at the input end of the amplifier. The noise figure of the proposed amplifier was below 5.6 dB throughout the whole gain region in the experiment.

Figure 5 shows the gain of the different EDYFA configurations against different input signal powers. The amplifiers were tested at two 1536 nm and 1550 nm input signal wavelengths which are represented by solid and hollow symbols, respectively. It was observed that the proposed amplifier displayed the highest gain at small input signals as compared to other configurations. At 1536 nm, the gain of the proposed amplifier configuration improved at input signal powers lower than –28 dBm. However for the 1550 nm input signal, the gain enhancement could only be observed up to –6 dBm. At 1550 nm, the gain of the proposed amplifier improved by up to 11 dB and 7.5 dB in comparison to the dual stage and conventional EYDFA configurations, respectively. The 1550 nm gain was also maintained around 30 dB throughout the small signal power region before it started to saturate to half of its value once the input signal power reached the value of –22 dBm. A gain reduction in the proposed amplifier was observed for both wavelengths at large input signal powers as shown in Figure 5 due the incorporation of additional components which increased the loss.

Figure 6 on the other hand depicts the corresponding noise figure for all the three amplifiers mentioned above for a 1550 nm input signal wavelength. It was observed that the noise figure of the proposed amplifier had a smaller value than the dual-stage amplifier at smaller input signal powers (<–30 dBm). The higher noise figure obtained at larger input signal powers was attributed to losses introduced by the additional optical components inside the amplifier system such as the second circulator and BPF that eventually limited the gain and consequently increased the noise figure. In comparison with the conventional EYDFA, a maximum noise figure improvement of 1.7 dB was observed for the proposed amplifier at the smallest input signal power of –50 dBm.

These results showed that the dual-stage partial double-pass configuration was capable of achieving a high-gain and low-noise figure in the EYDFA. The double-pass structure with a BPF at the second stage increased the attainable gain due to the double propagation of the signal in the gain medium as well as the filtering of the forward ASE from the second stage. The noise figure was also reduced by using a short-gain medium at the first stage in conjunction with mid-way circulator. The proposed

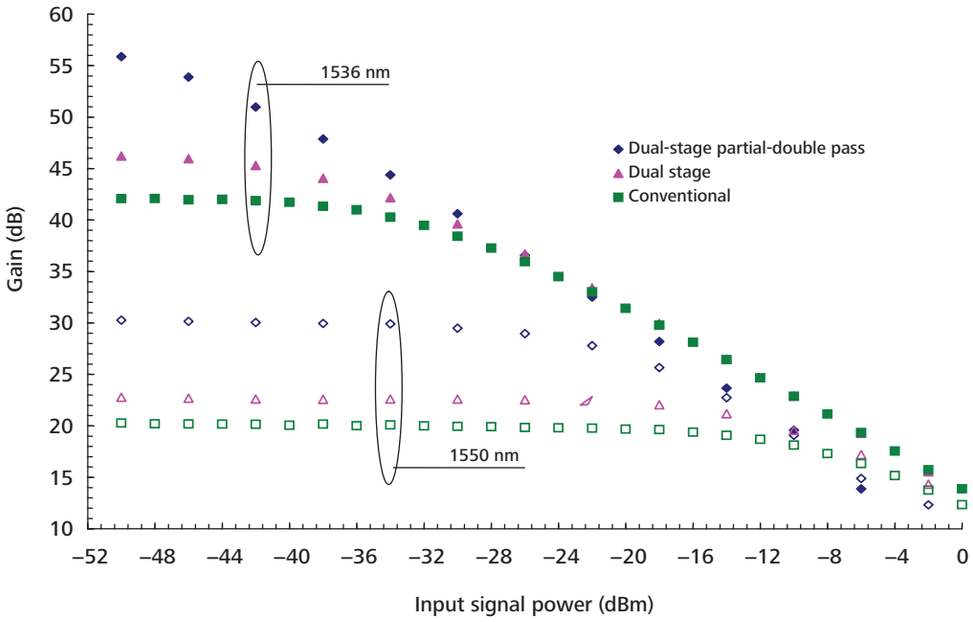

Figure 5. Gain against different input signal powers for the dual-stage partial double-pass, dual-stage and conventional EYDFA configurations. Input signal wavelength = 1536 nm.

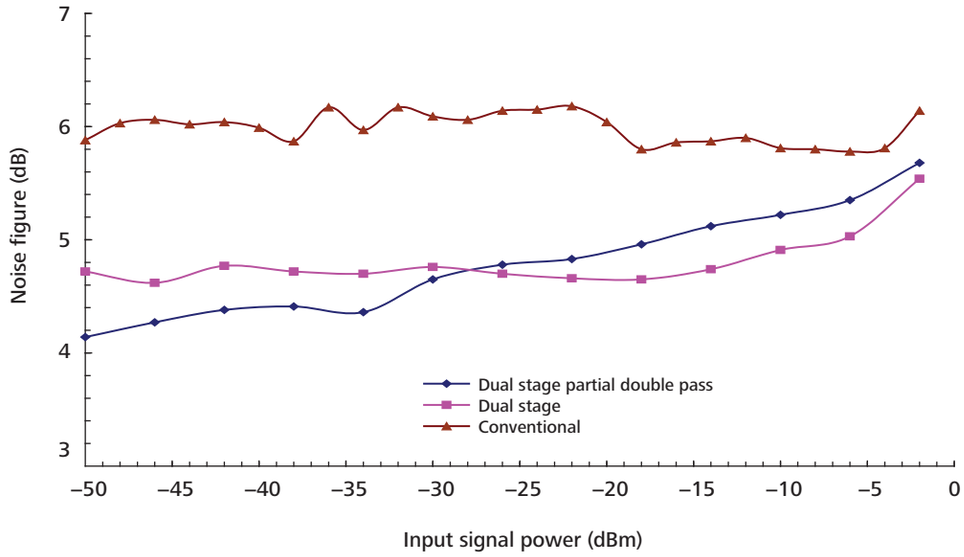

Figure 6. Noise figure against different input signal powers for the dual-stage partial double-pass, dual-stage and conventional EYDFA configurations. Input signal wavelength = 1536 nm.

amplifier was suitable for in-line and pre-amplification applications which required high-gain and low-noise figure characteristics.

CONCLUSION

Significant gain enhancement and a reduced noise figure had been achieved by exploiting certain EYDFA parameters and re-arranging the amplifier configuration. The dual-stage partial double-pass EYDFA demonstrated high efficiency from the double-pass structure and a low-noise figure from the double structure. The amplifier system suppressed the ASE self-induced saturation effect and consequently enhanced the gain and improved the noise figure. A maximum gain of 56.0 dB and a maximum gain enhancement of around 17.0 dB had been achieved for input signal wavelength of l536 nm and 1544 nm, respectively when compared to the conventional EYDFA configuration. The lowest noise figure of 4.1 dB had been achieved in this configuration at 1544 nm input signal wavelength and –50 dBm input signal power.

Date of submission: September 2008
Date of acceptance: November 2008

REFERENCES

Federighi, M & Di Pasquale, F, 1995, 'The effect of pair-induced energy transfer on the performance of silica waveguide amplifiers with high Er^{3+}/Yb^{3+} concentration', *IEEE Photonics Technol. Lett*., vol. 7, pp. 303–305.

Gapontsev, VP, Matitsin, SM, Isineev, AA & Kravchenko, VB, 1982, 'Erbium glass lasers and their applications,' *Optics and Laser Technol*., pp. 189–196.

Grubb, SG, Humer, WF, Cannon, RS, Windhorn, TH, Vendetta, SW & Sweeney, KL, *et al*. 1992, '+21dBm erbium power amplifier pumped by a diode-pumped Nd:YAG Laser', *IEEE Photonics Technol Lett*, vol. 4, no. 6, pp. 553–553.

Harun, SW, Abdul-Rashid, HA, Muhd-Yassin, SZ, Abd-Rahman, MK, Jayapalan, KK & Ahmad, H, 2007, '37.2 dB small-signal gain from Er/Yb co-doped fibre amplifier with 20 mW pump power,' *Opt. Laser Technol*., vol. 40, no. 1, pp. 88–91.

Harun, SW, Abdul-Rashid, HA, 2006, Muhd-Yassin, SZ, Abd-Rahman, MK, Tamjis, MR & Ahmad, H, 'Dual-stage Er/Yb doped fibre amplifier for gain and noise figure enhancements', *IEICE Electronics Express*, vol. 3, no.23, pp. 517–521.

Layne, CB, Lowdermilk, WH & Weber, MJ, 1977, 'Multiphonon relaxation of rare-earth ions in oxide glasses', *Phys. Rev. B*, vol. 16, no. 10, pp. 3259–3261.

Park, N, Wysocki, P, Pedrazzani, R, Grubb, S, DiGiovanni, D & Walker, K, 1996, 'High power Er–Yb-doped fibre amplifier with multichannel gain flatness within 0.2 dB over 14 nm', *IEEE Photon. Technol. Lett*. vol. 8, no. 9, pp. 1148–1150.

Sudo, S, 1997, Optical fiber amplifiers: materials, devices and applications. Boston: *Artech House, Inc*.

Wysocki, PF, Nykolak, G & Scott Shenk, D, 1996, 'Noise figure limitation in ytterbium-codopederbium-doped fibre amplifiers pumped at 1064 nm', in *OFC '96 Technical Digest paper*.

Yassin, SZM, 2008, Erbium Ytterbium Doped Fibre Amplifier, Optimization and Enhancements, Msc. Dissertation, UiTM.

Tsunamis Warning Systems — A Concise Review

W.D. Mooney[1]

Tsunamis are a significant geological hazard, particularly for countries bordering the Indian and Pacific Oceans. National tsunami warning systems consist of three critical components: a detailed tsunami hazard assessment; establishment of an earthquake and tsunami monitoring, notification and warning center; and a broadly based public education programme to promote local community preparedness. Each of these components is described, along with the scientific and technical challenges in establishing an effective national tsunami warning system.

Tsunamis have captured the world's attention in recent years due to their devastating power of destruction. The 2004 Indian Ocean tsunami left hundreds of thousands of people dead, missing or homeless (Satake & Atwater 2007). This tragedy has resulted in a renewed sense of urgency in the field of tsunami warnings and hazard mitigation. In this paper, I have reviewed the general characteristics of tsunamis and summarized the critical elements of an effective programme for tsunami monitoring, notification, and hazard reduction.

GENERAL CHARACTERISTICS OF EARTHQUAKES AND TSUNAMIS

The discovery of plate tectonics, in part through the use of a worldwide network of seismographs that was in operation during the 20th century, led to great advancements in understanding earthquakes (Bolt 2006) as shown in Figure 1. Plate tectonic theory shows that there are three basic types of boundaries between tectonic plates: divergent, convergent, and transform-fault boundaries (Figure 2). At a divergent plate boundary, also called a rift zone, two plates move away from each other and magma is pushed to the Earth's surface. At a convergent boundary, the lower plate is thrust below the upper plate. The upper and lower plates may be either oceanic or continental plates. The world's largest earthquakes happen at convergent boundaries, where an oceanic plate is pushed beneath a continental plate, such as occurs along the south coast of Indonesia and the west coast of South America. A transform-fault boundary is where two plates slide past each other, such as the San Andreas fault in California. Finally, there are plate boundary zones which are wide areas that are not well-defined and the interaction between the plates is broad and quite complex.

Earthquakes occur when neighbouring lithospheric tectonic plates (grey colour in Figure 2) lock against each other, restraining movement between them until the stress exceeds the strength of the rocks. This stress is then released in an earthquake which generates strong ground shaking that often cause severe damage to buildings, deadly landslides and in some cases, a tsunami.

Most tsunamis are generated by earthquakes at convergent plate boundaries, and specifically at oceanic-continental subducting plate boundaries (i.e. at subduction zones; Figure 3). Earthquakes that cause destructive tsunamis have relatively large magnitudes (M $\geq$8) and shallow (depth $\leq$30 km) hypocentre depths. Tsunamis that are not caused by earthquakes are due to underwater volcanic eruptions (e.g. Krakatoa, Indonesia, 1883), underwater landslides and rarely, meteorite impact.

Tsunami generation requires a large (e.g. 5 m – 20 m) displacement of the seafloor, usually caused by the rapid vertical uplift of the seafloor during a subduction zone earthquake. Such earthquakes also cause strong ground shaking at frequencies of 1 Hz – 10 Hz that can be felt in nearby communities. A related type of earthquake that can also generate a tsunami is called a 'slow' or 'tsunami earthquake'. These are slow rupturing subduction zone earthquakes that do not generate significant high frequency (1 Hz – 10 Hz) seismic energy and thus are not felt by the local population, nor are they well recorded on traditional high frequency seismographs (Kanamori & Kikuchi 1993; Mori *et al*. 2007). 'Tsunami earthquakes' can generate large tsunamis, especially for their seismic magnitude because a large fraction of their energy is coupled into the ocean tsunami wave. Tsunami earthquakes are deadly because the local population does not feel strong ground shaking, and therefore have no warning. A warning can only be provided by an advanced tsunami warning system that detects tsunami earthquakes.

In the open ocean, tsunamis propagate at velocities that may reach 900 km/hr and have wave heights less than a meter. As the tsunami approaches the shore and the water depth decreases, the waves get slower and taller, with

[1] US Geological survey, 345 Middlefield Road MS 977, Menlo Park, CA, USA 94025-3591
Correspondence (e-mail: mooney@usgs.gov)

World Seismicity: 1990–2000

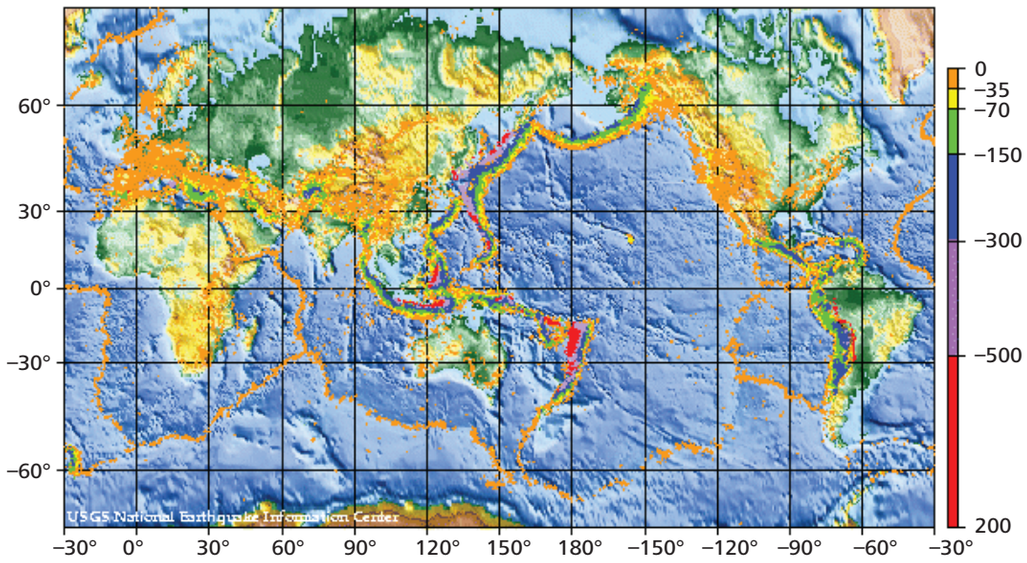

Source: USGS
Figure 1. Seismicity of the Earth (extreme latitudes excluded) over a 10 year period (1990–2000).

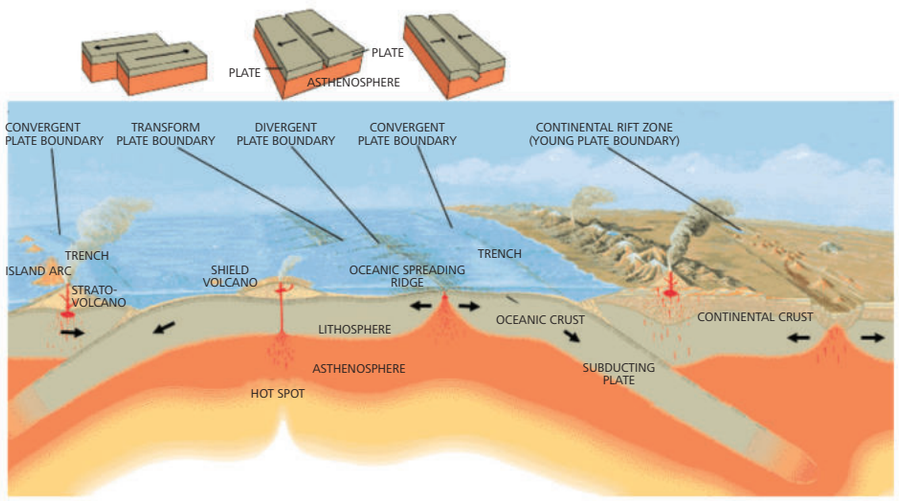

Source: <http://pubs.usgs.gov/gip/dynamic/Vigil.html>
Figure 2. Three dimensional geometry of the Earth's lithosphere.

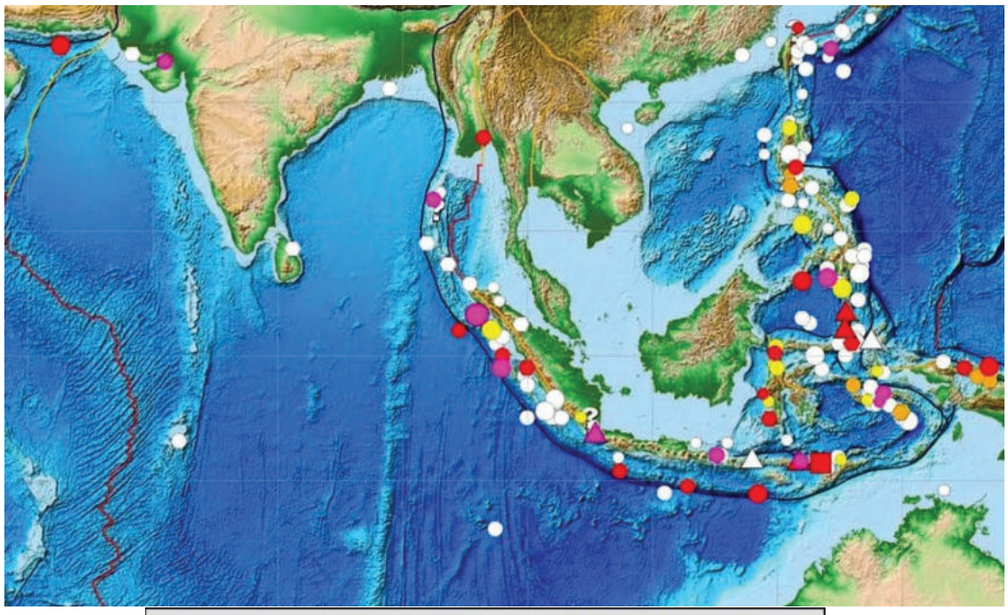

NOAA/NGDC WDC Tsunami Source Events								
Effects of the Tsunami	Volcanic Eruption	Landslide	Unknown Cause	Earthquake Magnitude >=9	>=8	>=7	>=6	Not recorded
Very Many Deaths (~1001 or more deaths)	▲	■	?	●	●	●	●	●
Many Deaths (~101 to 1000 deaths)	▲	■	?	●	●	●	●	●
Some Deaths (~51 to 100 deaths)	▲	■	?	●	●	●	●	●
Few Deaths (~1 to 50 deaths)	▲	■	?	●	●	●	●	●
No Deaths	△	□	?	○	○	○	○	○
Plate Boundaries: Divergent — Convergent — Transform								

Source: WDC-Tsunamis/NGDC and ITIC
Figure 3. NOAA/NGDC WDC tsunami source events.

velocities of 30 km – 40 km/hr and wave heights reaching as much as 10 to 30 meters. Tsunamis do not consist of a single wave, but a series of waves, known as a wave train. Successive waves arrive with a period that ranges from a few minutes to over an hour. As a result, it is difficult to predict the conclusion of a complete tsunami event, as the entire tsunami consists of multiple waves. Furthermore, the original earthquake may be followed by additional aftershocks or landslides that will trigger separate tsunami events. The destructiveness and intensity of waves is largely dependent on particular coastal features such as bays, inlets, seafloor ridges and canyons, or even coral reefs and local flora. *Run-up* height refers to the maximum height that the tsunami reaches above sea level. *Inundation* refers to the maximum horizontal distance that the tsunami travels inland. The prediction of run-up and inundation zones requires detailed knowledge of the offshore bathymetry which determines wave height and onshore topography which determines inundation.

LOCAL VERSUS DISTANT TSUNAMIS

In a local tsunami, the wave is generated near the shore. The first destructive wave may reach the coastline in 10–20 minutes and have a run up of 10 m above sea level. This may not allow enough time for local authorities to issue a formal tsunami warning bulletin. Therefore, awareness training must be provided to the public so that ordinary citizens are able to rely on their own understanding of tsunami's natural warning signs (e.g. earthquake shaking or recession of the ocean prior to an inundation) and make

their own decision on when to evacuate. For a distant tsunami, also referred to as a teleseimic tsunami, the source area will be one or more thousand km from the coastline of interest, and it may require several hours or more for the wave to arrive. In this case, there is ample time for local authorities to issue a warming using sirens located along the coast and messages issued on the broadcast media.

TSUNAMI HAZARDS IN INDIAN OCEAN REGION

On 26 December, 2004, a M 9.2 earthquake occurred about 150 km off the west coast of Sumatra (Indonesia) and the Andaman-Nicobar Islands (India). As no earthquake and tsunami alert system existed in the Indian Ocean at this time, the initial magnitude and location of this event was first determined by the NOAA Pacific Tsunami Warning Center (PTWC) in Hawaii within *ca*. 20 minutes. Due to the fact that no trans-oceanic tsunami had ever before been instrumentally recorded in the Indian Ocean, there was a general lack of preparedness for such this mega-tsunami. Not only were the vulnerable countries not expecting a large tsunami from this earthquake, but even if they had received advanced warning of approaching waves, they lacked effective means to communicate the danger to local populations.

It is well known that all countries that border the Indian Ocean are susceptible to tsunami threat, particularly from the seismically active Sunda trench that lines south and west of the Indonesian archipelago and extends in a broad arch to Burma (Vigny *et al*. 2005; Subaya *et al*. 2006; Satake & Atwater 2007). A compilation of ninety tsunamis that were recorded in the Indian Ocean in the last several centuries revealed that 80% of the tsunamis originated from the Sunda arc, approximately one every three years (Figure 3). The seismic activity in the Sunda arc is caused by elastic strain that builds when the Indian plate slides beneath the Burma plate. This strain which can accumulate over centuries is released in a matter of minutes, potentially causing rapid seafloor uplift that triggers a tsunami.

KEY COMPONENTS OF A TSUNAMI EARLY WARNING SYSTEM

The establishment of an effective Indian Ocean Warning System is needed to avoid a repeat of the devastating losses due to the 26 December 2004 mega-tsunami. To date, a multi-national system has not been established, but national systems have been developed in many Indian Ocean countries. Similar systems are under development in the Caribbean and Atlantic Oceans. All national warning systems have three critical components: assessment of national tsunami risk; establishment of national / regional warning centre for local and distant tsunamis, and a broadly based programme of education regarding preparedness for tsunami hazards.

A first step in preparing for tsunamis is an accurate understanding of the level of risk that is present based on a knowledge of the location of potential tsunami source regions and near-shore seafloor bathymetry near population centres. Second, an earthquake and tide level monitoring system, together with a broadcast warning system is needed that can reliably inform vulnerable populations of impending tsunamis. Thirdly, community education is an important step in preparing citizens to take proper action during an evacuation and thus, save lives during a tsunami. Land use planning and proper engineering design of resistant structures are also important.

TSUNAMI HAZARD ASSESSMENT

Paleotsunami Research

Paleotsunami research establishes the long-term history of past tsunamis in a study area. The paleotsunami record may extend back to hundreds or thousands of years. This record permits a more informed assessment of the risk posed to coastlines due to the impacts of tsunamis and is essential for effective mitigation and for forecasting future catastrophes (Jankaew *et al*. 2008). This assessment requires knowledge of probable tsunami sources, their likelihood of occurrence, and the characteristics of tsunamis from those sources at different places along the coast. Paleotsunami research is a slow, detailed process that requires years of field work (Satake *et al*. 2003; Atwater *et al*. 2005; Kumar & Achyuthan 2006; Satake & Atwater, 2007; Jankaew *et al*. 2008; Monecke *et al*. 2008).

Post-tsunami Assessments

A dictum in Earth Sciences is that the past is the key to the future. Thus, after a tsunami has struck, it is important to conduct detailed post-tsunami surveys in order to measure regional variations in tsunami wave heights as measured by watermarks on buildings, scars on trees, and rafted debris. In addition, it is useful to collect and measure the height of soil samples and sand deposits, and map the thickness and grain size distribution of sand. The latter observations are correlated with measured wave height and flow velocity. This information is useful in the interpretation of paleotsunami deposits. It is also useful for mitigation planning.

Numerical Modeling

Numerical modeling of tsunami inundation provides a prediction of tsunami wave heights and arrival times at regional coastlines for a significant earthquake at a specific location (Liu 2005). Such modeling can be used

to estimate the maximum probable level of destruction a tsunami can deliver at selected coastal cities (i.e. the 'worst case scenario') which is then used by urban planners and emergency management specialists to set standards for building tsunami-resilient communities. This information is the basis for the establishment of tsunami evacuation routes and the placement of tsunami shelters. Simulations are run for three tsunami processes: earthquake source modeling,ocean propagation, and run-up or inundation on dry land.

Earthquake source modeling is the estimation of the fault geometry, the amount of fault slip, and the corresponding seafloor displacement for a subduction zone earthquake. Ocean modeling of tsunami propagation tracks the progress of the tsunami through the ocean and is highly influenced by three-dimensional seafloor bathymetry. Run-up and inundation modeling predicts the effect on land, and requires sophisticated techniques since a single wave may evolve into several waves of different wavelengths. Detailed near-shore seafloor topography is the most important boundary condition for inundation modeling, since it may change the height and direction of wave propagation and may cause wave breaking. Sophisticated numerical simulation techniques are a necessary component of tsunami warning centers because the propagation of tsunami waves may exhibit high directionality that cannot be estimated without modeling.

Information regarding real-time wave heights of an incoming tsunami from tide gauges is quite valuable, but may not be detailed enough to predict the full extent of an impending inundation. For this reason, most tsunami early warning systems do not rely on real-time tsunami inundation models, but rather consult a database of inundation and run-up heights from previous calculated tsunami numerical simulations.

Estimates of the earthquake fault plane mechanism and seafloor displacement can usually be resolved ten to twenty minutes after the earthquake origin time if data from broadband seismometers are available. Near-field GPS receivers can provide complementary information regarding the earthquake source properties (Vigny *et al*. 2005). Previously compiled numerical simulations are then compared with real-time observations from tide gauge data so that an appropriate simulation can be selected as the best forecast of the impending tsunami inundation. The initial selection may be based on seismic parameters, but as additional deep ocean and coastal tide gauge data arrive, this selection can be refined. Figure 4 shows numerical modeling of the maximum computed tsunami amplitudes around the globe after the December 26, 2004 Indian Ocean Tsunami.

Probabilistic Tsunami Hazard Analysis (PTHA)

PTHA is a new technique used to determine the likelihood of a tsunami hazard and is derived from Probabilistic Seismic Hazard Analysis (PSHA). PSHA has been useful for reducing the variability in seismic activity to a manageable set of parameters. PTHA is broken into multiple components, the first of which assesses the hazard for offshore tsunami height. The second component uses these tsunami waveforms and empirical data, when available, to

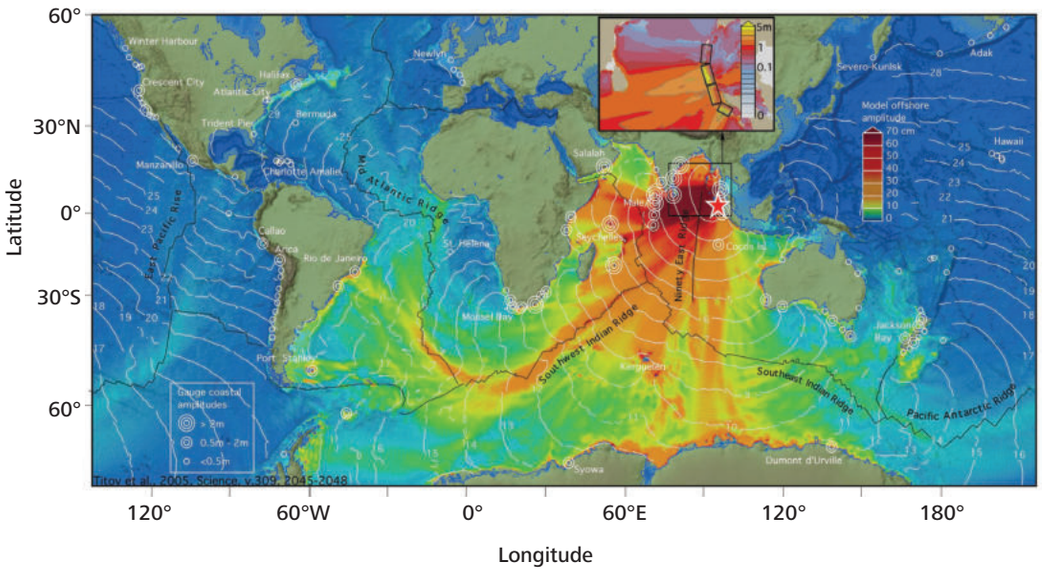

Source: NOAA
Figure 4. Numerical model of wave height following the 26 December 2004 tsunami.

obtain probabilistic tsunami run-up and inundation hazards (Thio *et al*. 2006; Geist & Parsons 2006).

TSUNAMI EARLY DETECTION AND WARNING

Seismology

In all tsunami warning systems, seismic information is the first data examined to determine whether an earthquake has the potential to generate a destructive tsunami. The primary goal is to quickly and accurately determine the earthquake magnitude and hypocentral depth. In the best case, this process can take just 5–10 minutes after the origin time of the event, leaving little time for a local warning. Such warnings are most effective for distant tsunamis, which allow more time for evacuations. For local tsunamis there may not be enough time for a warning based on the analysis of seismological data. An ideal tsunami warning system for local and distant tsunamis would contain broadband and strong ground motion seismometers in order to detect all seismic wave frequencies in near-real-time. Key problems in the seismic monitoring component of a tsunami warning system include data latency (i.e. transmission delay) and data loss (i.e. non-operational seismic stations), difficulties in the rapid calculation of magnitude and focal mechanisms, and in adequate training of staff. The loss of data from some stations reduces the accuracy of magnitude calculations significantly. Training of staff in modern techniques of tsunami warnings are needed to reduce the delay time for processing seismological data.

Sea Level Gauges (DART, GLOSS)

Tsunami warning based entirely on seismic information may run a high risk of false alarms. Not every large earthquake from a subducting oceanic plate will generate a tsunami and a direct measurement of water level is necessary for confirmation. Water level data furthermore provide a basis for determining whether the tsunami hazard has passed.

There are two main types of open-ocean offshore sea-level gauges: the Deep Ocean Assessment and Reporting of Tsunamis (DART) system buoys developed in the United States (Figure 5); and the Ocean Bottom Unit (OBU) connected to a surface GPS-buoy that was developed in Germany. The DART buoy measures sea level with a precision bottom-pressure sensor. The OBU also measures bottom pressure and is equipped with a broadband seismometer to monitor seismic activity. Both of these systems provide deep ocean sea-level data that can be used to confirm the existence of a tsunami while the wave is still in the open ocean.

Along the coast, Global Sea Level Observing System (GLOSS) stations report on sea levels using standard tide gauges. GLOSS stations are a part of the Global Ocean Observing System (GOOS) which in turn is part of the Global Earth Observation System of Systems (GEOSS). GLOSS stations were originally designed to make long-term measurements of sea-level change, but now they play an important role in tsunami early warning systems.

Source: NOAA
Figure 5. Deep Ocean Alerting and Reporting of Tsunami (DART) buoy, showing the main components. Left: surface buoy; right: (yellow) pressure transducer.

Global Positioning System (GPS)

The slip distribution along an earthquake's fault plane, which is a key factor in determining the initial size of tsunami, can be calculated directly from coseismic displacements with GPS techniques (Vigny *et al*. 2005; Subarya *et al*. 2006; Sobelev *et al*. 2007). In order to make such calculations at high resolution, a dense local network of GPS stations is required. Seismic and GPS data are complimentary. While seismicity data defines the geometry of the subduction zone, GPS data is highly effective in determining the amount of slip on the fault. The overall synthesis of seismic, geodetic and oceanic data could provide important redundancy in a tsunami warning system, reducing the chance of a false alarm.

An important application of a local GPS network is to identify slipping versus locked regions of subduction zones. GPS measurements, in conjunction with measurements of coral reef uplift from previous earthquakes, may help identify the regions that are prone to future megathrust earthquakes (Sieh 2004).

DISASTER PREPAREDNESS AND RESPONSE

Pre-tsunami Preparedness Measures: Mitigation Strategies

Effective education and preparedness programme are essential for making a tsunami warning systems successful (Figure 6). Mitigation, education and planning at the government, private sector, community, and personal levels are crucial to minimize the loss of life and property. If a tsunami is generated locally, there is usually no time for authorities to issue a warning to coastal communities, but there is enough time for a self-determined response by local residents. For a local tsunami, the earthquake's strong ground shaking and receding water is often the only warning. Coastal residents must respond to the early signs of a potential tsunami without an official warning. Knowledge of warning indicators depends on community education. Awareness of the coastal tsunami hazards, recognition of the signs of an impending tsunami and use of evacuation routes are all important factors.

Many communities develop evacuation maps based on inundation maps and local tsunami records. As mentioned, numerical simulations can be used to estimate the maximum inundation level for large tsunamis. Emergency drills and simulations can prepare communities for future tsunamis and build confidence. Likewise, land-use policies for coastal areas should be based on vulnerability assessments and risk analysis. Community health clinics, police and fire departments, schools and nursing homes should not be built within inundation zones. Assembly areas and evacuation shelters are needed.

Warning Dissemination

An important aspect of a tsunami early warning system is the rapid and efficient dissemination of the warning. A reliable communications network that does not depend

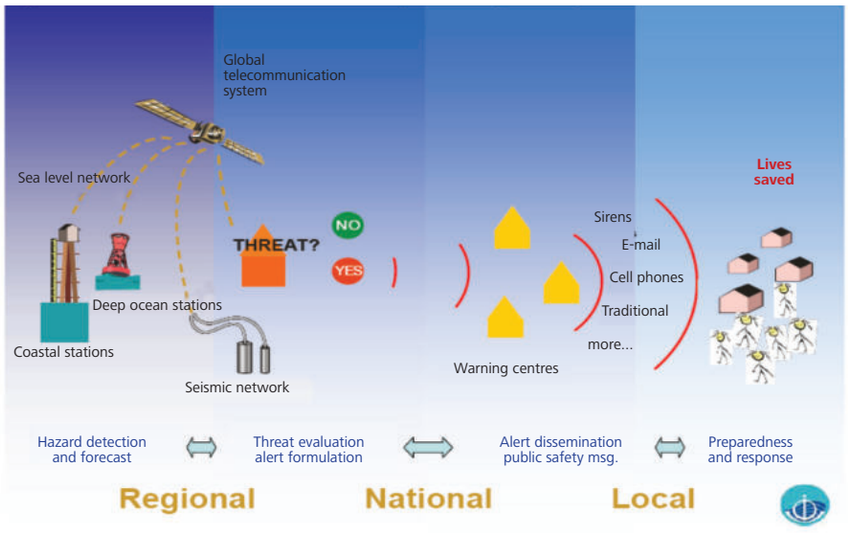

Figure 6. Summary diagram of tsunami warning and mitigation system.

Figure 7. Multi-national participants of an Indian Ocean Tsunami Warning Center training seminar pose with their instructors in Jakarta, Indonesia, 2006.

on highly vulnerable public power systems or cell phone telecommunications is of particular importance. In addition to sirens and the broadcast media, warning dissemination can be undertaken by local police and other officials. RAdio and InterNET for the Communication of Hydro-Meteorological and Climate Related Information (RANET) is a radio and satellite based communications system that uses the Worldspace AsiaStar Satellite. The Global Telecommunications System (GTS) is a global network for the transmission of meteorological data from weather stations, satellites and numerical weather prediction centers. This system is very fast and reliable.

CLOSING COMMENTS

Earthquakes and tsunamis are closely related phenomenon. Damaging tsunamis are most often formed by mega-thrust earthquakes (M >8.0) that occur at oceanic subduction zones (Figure 3). Tsunamis travel in the open ocean with exceedingly fast speeds (900 km/hr) and therefore efficient warning systems are needed to identify them and provide warnings to coastal communities. Fortunately, modern tsunami warning systems are highly effective in detecting tsunamis before they arrive at the coast. The key components of these systems have been summarized here, as well as the methods used to assess local tsunami hazards. Training of the tsunami warning center technical staff is an ongoing process (Figure 7). Most importantly, citizens need to be educated on what to do in the event of a tsunami. The residents of countries surrounding the Indian Ocean, including Malaysia, are now far better prepared for a future tsunami than at the time of the 26 December 2004, mega-tsunami. Continued progress depends on a long-term commitment by regional governments to solidify and reinforce progress in establishing effective national tsunami warning systems.

ACKNOWLEDGMENTS

Discussions with L. Kong, International Tsunami Information Center (ITIC) of the Intergovernmental Oceanographic Commission (IOC-UNESCO), Honolulu, Hawaii, are gratefully acknowledged. Thanks to E. Pryor who assisted with the preparation of this report. The author would like to thank the Malaysian Academy of Sciences for the opportunity to present this material as a lecture in Malaysia in 2008. P. Loganathan provided advice in determining the scope of this report.

Date of submission: August 2008
Date of acceptance: December 2008

REFERENCES

Atwater BF, Musumi-Rokkaku S, Satake K, Tsuji Y, Ueda K & Yamaguchi DK 2005, *The orphan tsunami of 1700: Japanese clues to a parent earthquake in North America*, U.S. Geol. Surv. Prof. Pap. 1707, U.S. Geol. Surv./Univ. Wash. Press, Reston, VA/Seattle, WA.

Bolt, BA 2006, Earthquakes, 5th edn, W. H. Freeman and Company, New York.

Geist, EL & Parsons, T 2006, 'Probabilistic analysis of tsunami hazards,' *Natural Hazards*, vol. 37, no. 3, pp. 277–314.

Jankaew, K, Atwater, BF, Sawai, Y, Choowong, M, Charoentitirat, T, Martin, ME & Prendergast, A 2008, 'Medieval forewarning of the 2004 Indian Ocean tsunami in Thailand', *Nature*, vol. 455, pp. 1228–1231.

Kanamora, H & Kikuchi, M 1993, 'The 1992 Nicaragua earthquake: a slow tsunami earthquake associated with subducted sediments,' *Nature*, vol. 361, 714–716.

Kumar, KA & Achyuthan, H 2006, 'A record of Palaeo-Tsunami in the Indian Ocean', in *Marine Geodesy*, vol. 29, 253–263.

Liu, PLF, 2005, 'Tsunami simulations and numerical models', *Bridge*, vol. 35, no. 2, pp. 14–20.

Monecke, K, Finger, W, Klarer, D, Kongko, W, McAdoo, BG, Moore AL & Sudrajat, SU 2008, 'A 1000-year sediment record of tsunami recurrence in northern Sumatra', *Nature*, vol. 455, pp. 1232–1234.

Mori, J, Mooney, WD, Afnimar, Kurniawan, S, Anaya, AI & Widiyantoro, S 2007, 'The 17 July 2006 tsunami earthquake in West Java, Indonesia, *Seismological Res. Letters*, 78, pp. 201–207.

Satake, K, Wang, K & Atwater, BF, 2003, 'Fault slip and seismic moment of the 1700 Cascadia earthquake inferred from Japanese tsunami descriptions', *Journal of Geophysical Research*, vol. 108 (B11).

Satake, K & Atwater, B 2007, 'Long-term perspectives on giant earthquakes and tsunamis at subduction zones', *Annual Reviews of Earth & Planetary Science*, vol. 35, pp. 349–374.

Sieh, K 2004, <http://www.tectonics.caltech.edu/sumatra/corals.html>.

Sobolev, SV, Babeyko, AY, Wang, R, Galas, R, Rothacher, M, Stein, DV, Schroter, J, Lauterjung, J & Subarya, C 2006, 'GPS-Shield: reliable prediction of tsunami amplitude within less than 10 minutes of an earthquake', *J. Geophys. Res*. vol. 112, B08415doi:10.1029/2006JB004640.

Subarya, C, Chlieh, M, Prawirodirdjo, L, Avouac, JP, Bock, Y, Sieh, K, Meltzner, AJ, Natawidjaja, DH, & McCaffrey, R 2006, 'Plate-boundary deformation associated with the great Sumatra–Andaman Earthquake', *Nature*, vol. 440, pp. 46–51.

Thio, H, Ichinose, G, Polet, J & Somerville, P 2006, 'Probabilistic tsunami hazards analysis', *Seismological Research Letters*, vol. 77, no. 2, p. 289.

Vigny, C, Simons, WJF, Abu, S, Bamphenyu, R, Satirapod, C, Choosakul, N, Subarya, C, Socquet, A, Omar, K, Abidin, HZ, & Ambrosius, BAC 2005, 'Insight into the 2004 Sumatra–Andaman earthquake from GPS measurements in southeast Asia', *Nature*, vol. 436, pp. 201–206.

Laser Research at the University of Technology Malaysia

N. Bidin[1]

The laser technology laboratory (LTL) of the Physics Department, University of Technology Malaysia was established in 1989 to support research and development activities. The laboratory provides activities for short- and long-term projects to serve final year undergraduate and post-graduate students in masters and PhD programmes.

LTL is equipped with a high powered Q-switched Nd:YAG laser system for laser matter interaction study, an argon fluoride excimer laser system for laser surface treatment study and titanium-doped sapphire laser system for ultrafast laser science study. Nitrogen-pumped liquid lasers are available to provide ultraviolet and tunable light sources for scientific research. High powered diode pumped solid lasers are utilized as optical pumped sources as well as sources for medical application study.

Besides using lasers as tools in different scientific research programmes, work is also emphasized in designing and engineering laser systems. In these cases various high voltage power supply system on kilovolt scales have been designed using conventional and modern techniques. These include high speed switch devices for beam modulation techniques using acousto-optic, electro-optic and saturable absorber mechanisms. The innovation in these works have won some medals and patents have been successfuly filed. Among the novel works that have won awards are the electro-optic Q-switch system, programmable energy control unit and the enhancement nanosecond laser assembly.

Laser Matter Interaction

The high powered Q-switched Nd:YAG laser system is used for laser matter interaction study (Figures 1 and 2). The laser can be focused either at atmospheric pressure or in a vacuum chamber to study non-linear effect phenomenon. The activities in the focal region are visualized using a charge coupled devise (CCD) camera in conjunction with high speed photography. Langmuir probes, Faraday cups, high frequency digital oscilloscopes or spectrum analyzers are employed to measure the plasma properties.

Laser Surface Treatment/ Laser annealing

An argon fluoride excimer laser (Figure 3), having a fundamental wavelength of 193 nm, is employed as a source of ablation. Laser ablative figuring is set up to monitor the ablation process. A Fabry-Perot interferometer is used as a dynamic sensor to monitor the ablation process.

Figure 1. Laser matter interaction set-up.

Figure 2. A Q-switched Nd:YAG laser system.

[1] Department of Physics, Faculty of Science, University of Technology Malaysia, 81310, Skudai, Johor, Malaysia
Correspondence (e-mail: noriah@dfiz2.fs.utm.my)

Polymethylmethacrylate film or semiconductor thin films are coated on various types of substrates to form hybrids. Laser ablation is used for surface treatment. Laser annealing is also carried out to fabricate some of the semiconductor devices.

Figure 3. Surface treatment or laser annealing by argon fluoride excimer laser.

Advanced Laser Science

Ultrafast titanium-doped sapphire Ti:sapphire is one of the sources used in advance laser science (Figure 4). The ultrashort pulse duration of the laser can be achieved within femtoseconds. The system is set up using a diode pumped solid state diode pumped solid state (DPSS) laser as an optical pumping source. A Z folded cavity was aligned to match with the pumping source and tightly focus the beam in the cavity. A titanium-doped sapphire crystal is utilized as the gain medium. A non-self starting technique is used to inject the femto-pulse signal. A pair of prisms are introduced to compensate for the dispersion in the cavity.

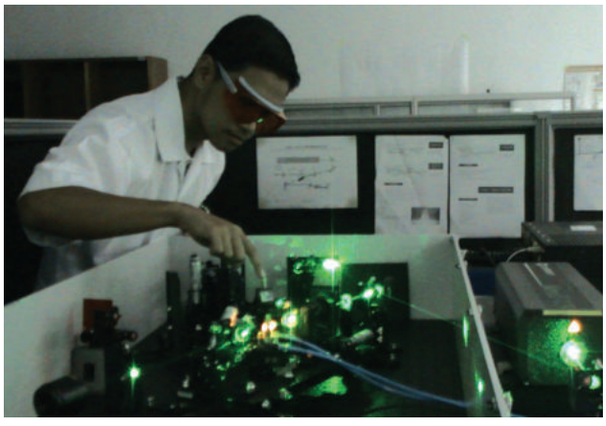

Figure 4. Ultrafast Ti:sapphire laser system.

Solid State Laser Engineering

Research activities are also conducted to design and construct laser systems. These include the design of the flashlamp driver used to pump the solid state Nd:YAG laser rod (Figure 5). Many parts of the driver were innovated to make them more efficient, reliable and robust. The laser resonator is aligned by using different types of laser mirrors. The laser pulse laser was modulated by designing the pockel cell modulator as well as the pockel cell driver. A high voltage power supply using switch mode power supply technique was developed to miniaturize the size as well as to be more user-friendly.

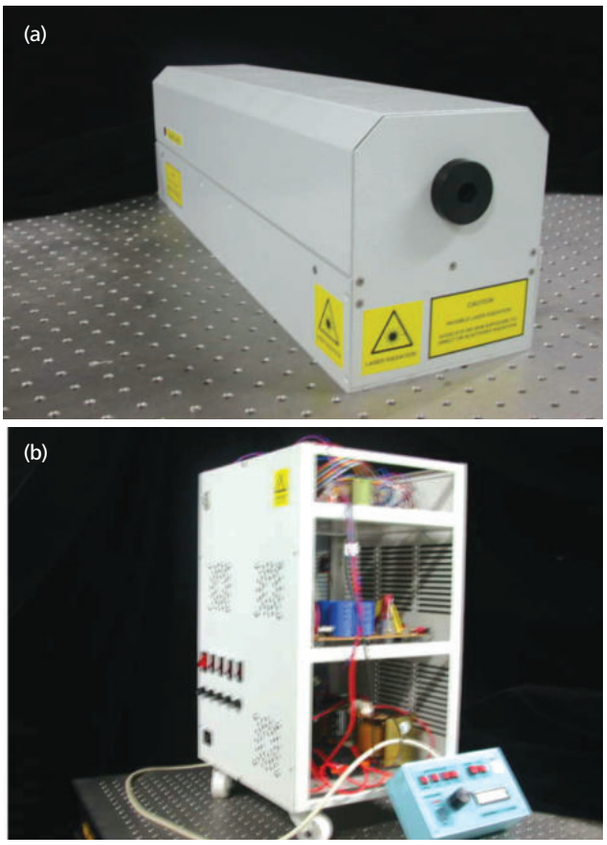

Figure 5. The laser head (a) and flashlamp driver (b) — the first laser developed solid state Nd: YAG at University Technology Malaysia (UTM) in 2007.

Crystal Growth Machine

Laser material used as active medium and non-linear material for electro-optic application are other research studies conducted to support laser research in UTM. For this case, two machine are equipped to grow laser crystals (Figure 6). The first is an automatic machine for crystal growth using Cz method while the other is manually

operated using Bridgement method. Nd:yag laser crystal, lithium niobate crystal and sapphire crystal are among the crystals that have been grown (Figure 7).

Fabrication Machine

A rotary numerical computer controlled CNC ultrasonic drilling machine (Figure 8) which is available in the physics Department in UTM is purposely used to fabricate the bulk crystal grown in the Cz machine. This machine is used to core the bulk crystal into a cylindrical configuration. The shape of the crystal is in the form of a rod. Both ends of the laser rod are then fabricated by using a lapping and polishing machine (Figure 9).

Laser research at UTM covers a broad spectrum from laser material, electronic devices and laser applications.

Figure 6. Auto Diameter Control crystal growth machine: (a) the whole system; (b) Crystal enlargement chamber and (c) conventional crystal growth machine.

Figure 7. The product of crystal growth: (a) Nd:YAG crystal; (b) lithium niobate crystal and (c) Nd:YAG single crystal.

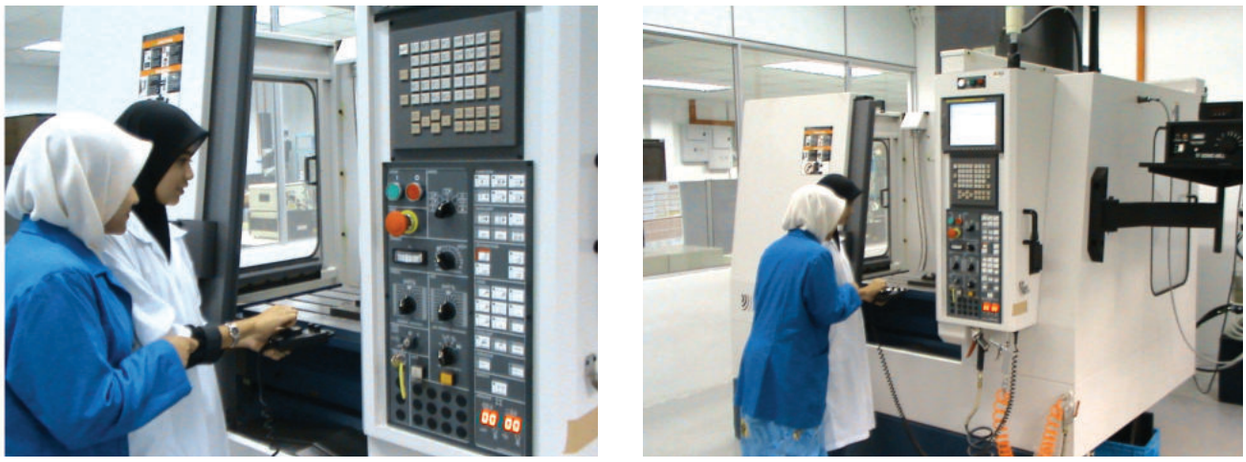

Figure 8. Rotary CNC ultrasonic drilling machine for crystal coring.

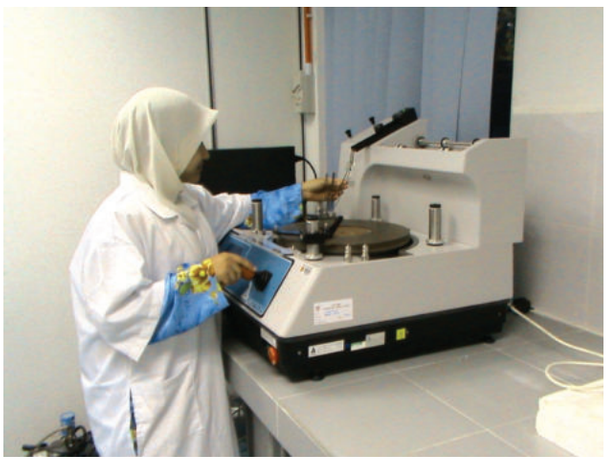

Figure 9. Crystal lapping and polishing machine.

Comet Lulin

M. Othman[1*] and K. Ahmad[2]

Comet Lulin was discovered by Lin Chi-Sheng and Ye Quanzhi using the 16-inch telescope at Lulin Observatory in Nantou, Taiwan in 2007. According to Brian Marsden of the Smithsonian Astrophysical Observatory, it reached its perihelion on 10 January 2009 at a distance of 113 million km from the Sun. It moves in a very nearly parabolic retrograde ('backwards' compared to the movement of the planets) orbit at an inclination of 1.6 degrees from the ecliptic ("Newfound Comet Lulin to Grace Night Skies"). http://www.space.com/spacewatch/090206-ns-comet-lulin.html). It passed nearest to the Earth at a distance of 61 million km on 23 February 2009.

Like other comets, Lulin is a conglomeration of ice and dust particles left over from the formation of the outer part of the solar system. As the comet approaches the Sun, the heat from the Sun vapourises the ice particles, the result of which is a fan-shaped tail of gas pushed away from the Sun by solar particles and the pressure from sunlight. Lulin sported an anti-tail, which is not a second tail but a rare optical effect because as the Earth crosses the comet's orbital plane we see parts of the tail projected on both sides of the comet's head, the coma. The central coma of the comet has a greenish colour which indicates that it is primarily made up of cyanogen and diatomic carbon.

This being its first pass around the Sun makes studies on Comet Lulin particularly valuable as it is in pristine condition, having been largely unchanged since it was formed together with the solar system about 4.5 billion years ago.

Comet Lulin C2007 N3
Optics: TMB152@fl7.9
Camera : SB1G STL-4020
Filters: SB1G Standard LRGB
Dates: 2009-02-18
Location: Langkawi National Observatory, Malaysia
Exposure Details: LRGB= 3:1:1:1 minutes

Comet Lulin C2007 N3
Optics: RCOS 0.5 Meter @ f/8.1
Camera: SBiG STL-11000
Filters: S8/G Standard LRGB
Dates / Times (UT): 2009- 01-06/22:36:06
Location: Langkawi National Observatory, Malaysia
Exposure Details: LRGB = 15:3:3:3 minutes

[1] United Nations Office for Outer Space Affairs, Vienna International Centre, P.O. Box 500, A- 1400 Vienna, Austria
[2] Langkawi National Observatory, National Space Agency of Malaysia, 5th Floor, Complex PJH, Block 2, Precinct 2, 62100 Putrajaya, Malaysia
* Corresponding author (e-mail: Mazlan.OTHMAN@unoosa.org)

MAHATHIR SCIENCE AWARD 2010

Invitation for Nominations

The Academy of Sciences Malaysia (ASM) is a body set up with a mission that encompasses pursuit, encouragement and enhancement of excellence in the fields of science, engineering and technology for the development of the nation and the benefit of mankind. The Academy has instituted the Mahathir Science Award (formerly known as ASM Award for Scientific Excellence in honour of Tun Dr Mahathir Mohamad) in recognition of scientists/ institutions who have contributed to cutting-edge tropical research that have had an impact on society.

This Award is Malaysia's most prestigious Science Award for tropical research launched in honour of Tun Dr Mahathir Mohamad who promoted and pursued with great spirit and determination his convictions in science and scientific research in advancing the progress of mankind and nations. Tun Dr Mahathir was the major force and the man who put into place much of the enabling mechanisms for a scientific milieu in our country.

This Award will be given to researchers who have made internationally recognised breakthroughs in pioneering tropical research in the fields of Tropical Medicine, Tropical Agriculture, Tropical Architecture and Engineering, and Tropical Natural Resources.

One Award will be conferred in 2010 covering any of the above four fields. The Award carries a cash prize of RM100 000, a gold medal and a certificate.

NOMINATION CRITERIA

- Awards will be given to researchers who have made internationally recognised breakthroughs in pioneering tropical research that have brought greater positive impacts on the well-being of society.
- Nominations can be made by individuals or institutions.
- A recipient could be an individual or an institution.

Nomination forms may be downloaded from the Academy's website:
www.akademisains.gov.my

Closing date: 31 March 2010

For more information, please contact:
Academy of Sciences Malaysia
902-4, Jalan Tun Ismail, 50480 Kuala Lumpur
Tel : 603-2694 9898; Fax : 603-2694 5858
E-mail: seetha@akademisains.gov.my
admin@akademisains.gov.my

22nd Pacific Science Congress

Asia Pacific Science in the New Millenium: Meeting the Challenges of Climate Change and Globalisation

13 –17 June 2011, Kuala Lumpur, Malaysia

The Congress will provide an inter-disciplinary platform for scientists from the region to discuss and review common concerns and priorities; bring together scientists from remote states; and serve as a catalyst for scientific and scholarly collaboration and to announce and establish new research initiatives. The Pacific Science Association (PSA) focuses on countries bordering the Pacific Ocean and the islands of the Pacific basin. PSA is a regional, non-governmental, and a scholarly organization that seeks to advance S&T in support of sustainable development in the Asia Pacific.

Sub-themes will include topics on:

- Impact on Large Marine Ecosystems
- Impact on Water & Food Systems
- Impact on Biodiversity & Ecosystem Services
- Ecological Economics
- Urbanization and the Health Challenge
- Energy for Sustainable Development
- Forces of Nature: Reducing Vulnerability to Hazards
- Monitoring and Assessment.

Schedule and Programme:

Both plenary and parallel sessions, invited lectures, poster sessions, with at least one session open to the public and an optional post-congress field excursion will be planned. Various symposia will also be organized around the sub-themes.

Enquiries:

Congress Secretariat
22nd Pacific Science Congress
c/o Academy of Sciences Malaysia
902-4, Jalan Tun Ismail
50480 Kuala Lumpur
Malaysia

Tel : (603) 2694 9898
Fax : (603) 2694 5858

e-mail: nasa@akademisains.gov.my; fardy@akademisains.gov.my
Website: www.akademisains.gov.my

ASM Publications

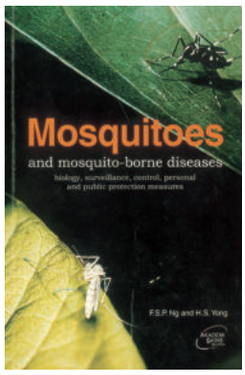

Mosquitoes and Mosquito-borne Diseases: Biology, Surveillance, Control, Personal and Public Protection Measures

F.S.P. Ng and *H.S. Yong (Editors)*
(2000)

ISBN 983-9445-05-7
Price: RM60.00 / USD20.00

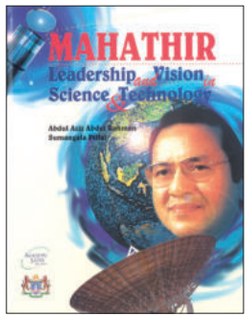

Mahathir: Leadership and Vision in Science and Technology

Abdul Aziz Abdul Rahman and *Sumangala Pillai*
(1996)

ISBN 983-9319-09-4
Price: RM100.00 / USD30.00

Budaya Kreativiti: Pameran Seratus Tahun Hadiah Nobel

Ulf Larsson (Editor)
(2004)

ISBN 983-9445-09-X
Price: RM50.00 / USD15.00

CD Kompilasi *Estidotmy*

Edisi 1 – 82, 2002–08
Price: RM35.00 / USD12.00

Mahathir: Kepimpinan dan Wawasan dalam Sains dan Teknologi

Abdul Aziz Abdul Rahman
dan *Sumangala Pillai*
(1996)

ISBN 983-9319-09-4
Price: RM100.00 / USD30.00

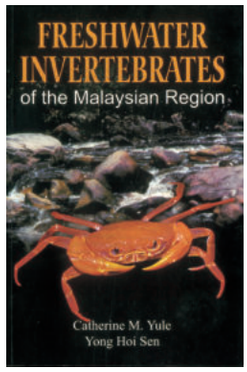

Freshwater Invertebrates of the Malaysian Region

Catherine M. Yule and *Yong Hoi Sen*
(2004)

ISBN 983-41936-0-2
Price: RM180.00 / USD52.00

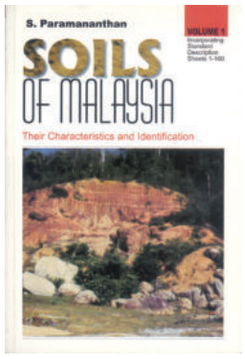

Soils of Malaysia: Their Characteristics and Identification (Vol. 1)

S. Paramananthan
(2000)

ISBN 983-9445-06-5
Price: RM100.00 / USD30.00

Bencana Tsunami 26.12.04 di Malaysia: Kajian Impak Alam Sekitar, Sosio-Ekonomi dan Kesejahteraan Masyarakat

Ibrahim Komoo (Editor)
(2005)

ISBN 983-9444-62-X
Price: RM100.00 / USD30.00

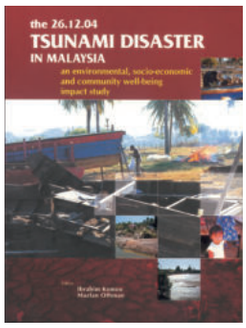

The 26.12.04 Tsunami Disaster in Malaysia: An Environmental, Socio-Economic and Community Well-being Impact Study

Ibrahim Komoo and *Mazlan Othman (Editors)*
(2006)

ISBN 983-9444-62-X
Price: RM100.00 / USD30.00

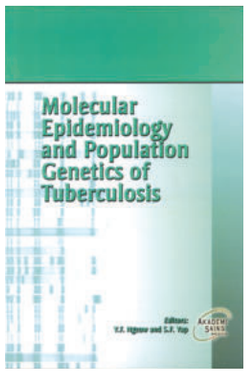

Molecular Epidemiology and Population Genetics of Tuberculosis

Y.F. Ngeow and *S.F.Yap (Editors)*
(2006)

ISBN 983-9445-14-6
Price: RM40.00 / USD12.00

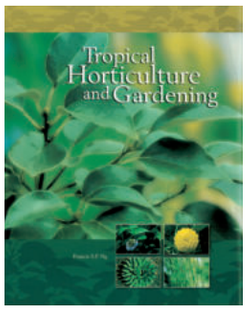

Tropical Horticulture and Gardening

Francis S.P. Ng
(2006)

ISBN 983-9445-15-4
Price: RM260.00 / USD75.00

Kecemerlangan Sains dalam Tamadun Islam: Sains Islam Mendahului Zaman
Scientific Excellence in Islamic Civilization: Islamic Science Ahead of its Time

Fuat Sezgin
(2006)

ISBN 983-9445-14-6
Price: RM40.00 / USD12.00

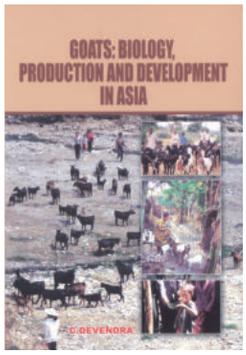

Goats: Biology, Production and Development in Asia

C. Devendra
(2007)

ISBN 978-983-9445-18-3
Price: RM180.00 / USD52.00

Proceedings: Seminar on Antarctic Research, 27–28 June 2005, University of Malaya, Kuala Lumpur, Malaysia

Irene K.P.Tan et al. *(Editors)*
(2006)

ISBN 978-983-9445-17-6
Price: RM40.00 / USD12.00

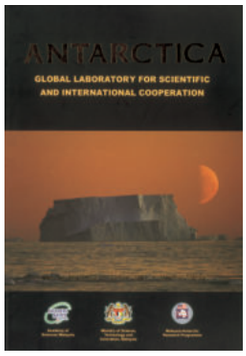

Antarctica: Global Laboratory for Scientific and International Cooperation

Aileen Tan Shau-Hwai et al. *(Editors)*
(2005)

ISBN 983-9445-13-8
Price: RM40.00 / USD12.00

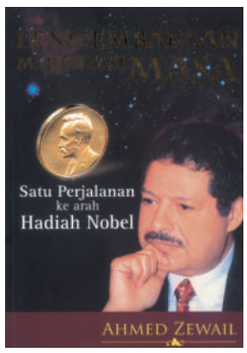

Pengembaraan Merentasi Masa: Satu Perjalanan ke Arah Hadiah Nobel

Ahmed Zewail
(2007)

ISBN 978-9445-20-6
Price: RM40.00 / USD12.00

ASM Publications

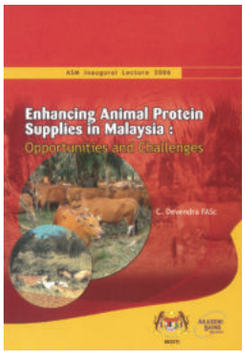

Enhancing Animal Protein Supplies in Malaysia: Opportunities and Challenges

C. Devendra
(2007)

ISBN 983-9444-62-X

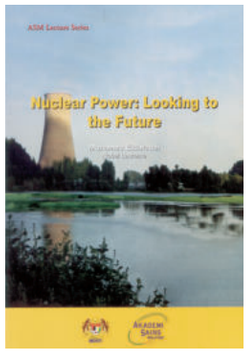

Nuclear Power: Looking to the Future

Mohamed ElBaradei
(2008)

ISBN 983-9445-14-6

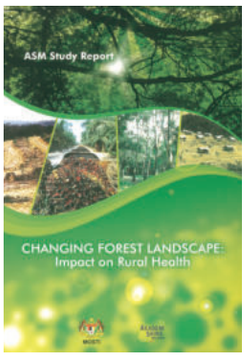

Changing Forest Landscape: Impact on Rural Health
(2007)

ISBN 983-9445-15-4

Dunia Sains
Vol. 5, No. 4, Oktober – Disember 2007
(2008)

A World of Science
Vol. 5, No. 4
October – December 2007

http://portal.unesco.org/science/en/ev.php-URL ID=5572&URL DO=DO TOPIC&URL SECTION=201.html

http://www. akademisains.gov.my/unesco/dunia_sains/okt_dis_2007.pdf

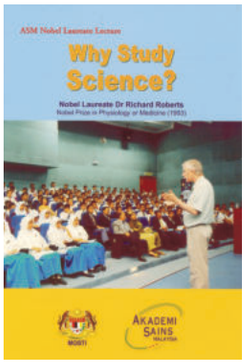

Why Study Science?

Richard Roberts
(2008)

ISBN 978-983-9445-18-3

Dunia Sains
Vol. 6, No. 1, Januari – Mac 2008
(2008)

A World of Science
Vol. 6, No. 1
January – March 2008

ASM Science Journal
Vol. 1, No. 1, June 2007

ISSN : 1823-6782

Price: RM100.00 / USD50.00 (Individual)
RM200.00 / USD100.00 (Institution)

ASM Science Journal
Vol. 1, No. 2, December 2007

ISSN : 1823-6782

Price: RM100.00 / USD50.00 (Individual)
RM200.00 / USD100.00 (Institution)

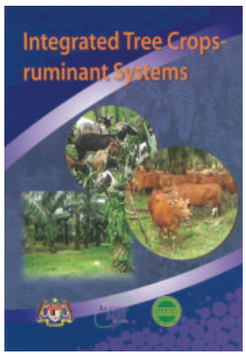

Integrated Tree Crops-ruminant Systems (Proceedings)

C. Devendra, S. Shanmugavelu and *Wong Hee Kum (Editors)*
(2008)

ISSN : 983-9445-24-3

Price: RM40.00 / USD12.00

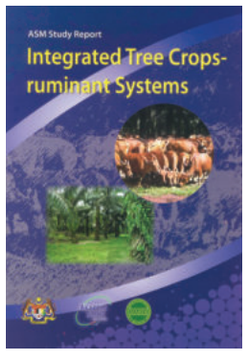

ASM Study Report: Integrated Tree Crops-ruminant Systems
(2008)

ISSN : 983-9445-24-4

Price: RM30.00 / USD9.00

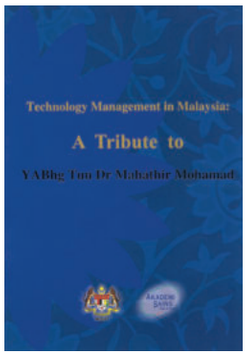

Technology Management in Malaysia: A Tribute to YABhg Tun Dr Mahathir Mohamad
(2008)

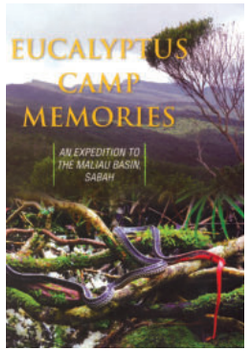

Eucalyptus Camp Memories: An Expedition to the Maliau Basin, Sabah
(2008)

ISSN : 978-983-9445-25-1

Price: RM220.00 / USD61.00 (Hard cover)
RM160.00 / USD42.00 (Soft cover)

ASM Science Journal
Vol. 2, No. 1, December 2008

ISSN : 1823-6782

Price: RM100.00 / USD50.00 (Individual)
RM200.00 / USD100.00 (Institution)

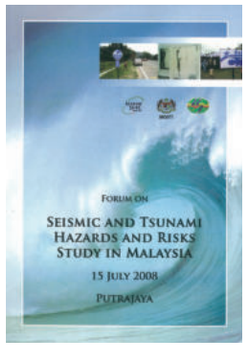

Forum on: Seismic and Tsunami Hazards and Risks Study in Malaysia 15 July 2008

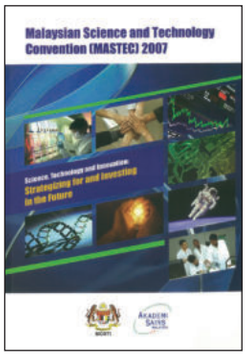

Science, Technology and Innovation: Strategizing for and Investing in the Future [Malaysian Science and Technology Convention (MASTEC) 2007]
(2009)

ISSN : 978-983-9445-27-5

Price: RM51.00 / USD22.00

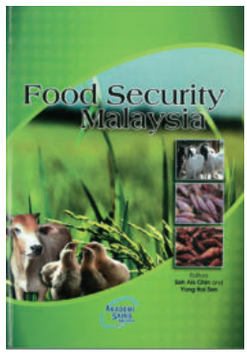

Food Security Malaysia (Proceedings)
Soh Aik Chin and Yong Hoi Sen (Editors)
(2009)

ISSN : 978-983-9445-28-2

Price: RM20.00 / USD6.00

ASM Publications

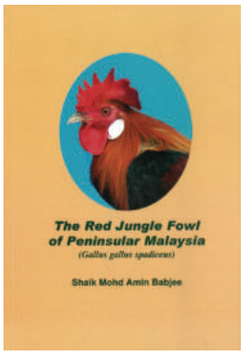

The Red Jungle Fowl of Peninsular Malaysia

Shaik Mohd Amin Babjee
(2009)

ISBN : 978-983-9445-29-9

Price: RM35.00 / USD12.00

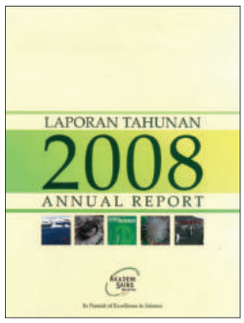

Academy of Science Malaysia

Annual Report 2008

Journal of Science & Technology in the Tropics

Vol. 4, No. 2, December 2008

ISSN:1823-5034

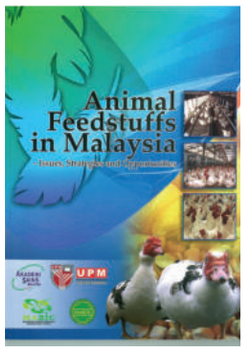

Animal Feedstuffs in Malaysia – Issues, Strategies and Opportunities
(2009)

ISBN : 978-983-9445-30-5

Price: RM35.00 / USD12.00

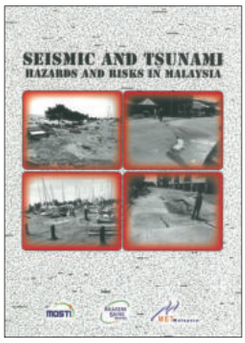

Seismic and Tsunami Hazards and Risks in Malaysia
(2009)

ISBN 978-983-9445-32-9

Price: RM45.00 / USD15.00

For purchasing, please access:
http://www.akademisains.gov.my

About the Journal

Mission Statement

To serve as the forum for the dissemination of significant research, S&T and R&D policy analyses, and research perspectives.

Scope

The ASM Science Journal publishes advancements in the broad fields of medical, engineering, earth, mathematical, physical, chemical and agricultural sciences as well as ICT. Scientific articles published will be on the basis of originality, importance and significant contribution to science, scientific research and the public.

Scientific articles published will be on the basis of originality, importance and significant contribution to science, scientific research and the public. Scientists who subscribe to the fields listed above will be the source of papers to the journal. All articles will be reviewed by at least two experts in that particular field. The journal will be published twice in a year.

The following categories of articles will be considered for publication:

Research Articles

Each issue of the journal will contain no more than 10 research articles. These are papers reporting the results of original research in the broad fields of medical, engineering, earth, mathematical, physical, chemical and life sciences as well as ICT. The articles should be limited to 6000 words in length, with not more than 100 cited references.

Short Communications

These are articles that report significant new data within narrow well-defined limits or important findings that warrant publication before broader studies are completed. These articles should be limited to 2000 words and not more that 40 cited references. Five (5) Short Communications will be accepted for publication in each issue of the journal.

Research Perspectives

These are papers that analyse recent research in a particular field, giving views on achievements, research potential, strategic direction etc. A Research Perspective should not exceed 2000 words in length with not more than 40 cited references.

Reviews/Commentaries

Each issue of the journal will also feature Reviews/ Commentaries presenting overviews on aspects such as Scientific Publications and Citation Ranking, Education in Science and Technology, Human Resources for Science and Technology, R&D in Science and Technology, Innovation and International Comparisons or Competitiveness of Science and Technology etc. Reviews/Commentaries will encompass analytical views on funding, developments, issues and concerns in relation to these fields and not exceed 5000 words in length and 40 cited references.

Science Forum

Individuals who make the news with breakthrough research or those involved in outstanding scientific endeavours or those conferred with internationally recognised awards will be featured in this section. Policy promulgations, funding, science education developments, patents from research, commercial products from research, and significant scientific events will be disseminated through this section of the journal. The following will be the categories of news:

- Newsmakers
- Significant Science Events
- Patents from Research
- Commercial Products from Research
- Scientific Conferences/Workshops/Symposia
- Technology Upgrades
- Book Reviews.

Instructions to Authors

The ASM Science Journal will follow the Harvard author-date style of referencing examples of which are given below.

In the text, reference to a publication is by the author's name and date of publication and page number if a quote is included, e.g. (Yusoff 2006, p. 89) or Yusoff (2006, p. 89) 'conclude.....' as the case may be. They should be cited in full if less than two names (e.g. Siva & Yusoff 2005) and if more than two authors, the work should be cited with first author followed by *et al*. (e.g. Siva *et al*. 1999).

All works referred to or cited must be listed at the end of the text, providing full details and arranged alphabetically. Where more than one work by the same author is cited, they are arranged by date, starting with the earliest. Works by the same author published in the same year are ordered with the use of letters a, b, c, (e.g. Scutt, 2003a; 2003b) after the publication date to distinguish them in the citations in the text.

General Rules

Authors' names:

- Use only the initials of the authors' given names.
- No full stops and no spaces are used between initials.

Titles of works:

- Use minimal capitalisation for the titles of books, book chapters and journal articles.
- In the titles of journals, magazines and newspapers, capital letters should be used as they appear normally.
- Use italics for the titles of books, journals and newspapers.
- Enclose titles of book chapters and journal articles in single quotation marks.

Page numbering

- Books: page numbers are not usually needed in the reference list. If they are, include them as the final item of the citation, separated from the preceding one by a comma and followed by a full stop.
- Journal articles: page numbers appear as the final item in the citation, separated from the preceding one by a comma and followed by a full stop.

  Use the abbreviations p. for a single page, and pp. for a page range, e.g. pp. 11–12.

Whole citation

- The different details, or elements, of each citation are separated by commas.
- The whole citation finishes with a full stop.

Specific Rules

Definite rules for several categories of publications are provided below:

Journal

Kumar, P & Garde, RJ 1989, 'Potentials of water hyacinth for sewage treatment', *Research Journal of Water Pollution Control Federation*, vol. 30, no. 10, pp. 291–294.

Monograph

Hyem, T & Kvale, O (eds) 1977, *Physical, chemical and biological changes in food caused by thermal processing*, 2nd edn, Applied Science Publishers, London, UK.

Chapter in a monograph

Biale, JB 1975, 'Synthetic and degradative processes in fruit ripening', eds NF Hard & DK Salunkhe, in *Post-harvest biology and handling of fruits and vegetables*, AVI, Westport, CT, pp. 5–18.

Conference proceedings

Common, M 2001, 'The role of economics in natural heritage decision making', in *Heritage economics: challenges for heritage conservation and sustainable development in the 21st century: Proceedings of the International Society for Ecological Economics Conference, Canberra, 4th July 2000*, Australian Heritage Commission, Canberra.

Website reference

Thomas, S 1997, *Guide to personal efficiency*, Adelaide University, viewed 6 January 2004, <http://library.adelaide.edu.au/~sthomas/papers/perseff.html>.

Report

McColloch, LP, Cook, HT & Wright, WR 1968, *Market diseases of tomatoes, peppers and egg-plants*, Agriculture Handbook no. 28, United States Department of Agriculture, Washington, DC.

Thesis

Cairns, RB 1965, 'Infrared spectroscopic studies of solid oxygen', PhD thesis, University of California, Berkeley, CA.

Footnotes, spelling and measurement units

If footnotes are used, they should be numbered in the text, indicated by superscript numbers and kept as brief as possible. The journal follows the spelling and hyphenation of standard British English. SI units of measurement are to be used at all times.

Submission of Articles

General. Manuscripts should be submitted (electronically) in *MS Word* format. If submitted as hard copy, two copies of the manuscript are required, double-spaced throughout on one side only of A4 (21.0 × 29.5 cm) paper and conform to the style and format of the *ASM Science Journal*. Intending contributors will be given, on request, a copy of the journal specifications for submission of papers.

Title. The title should be concise and descriptive and preferably not exceed fifteen words. Unless absolutely necessary, scientific names and formulae should be excluded in the title.

Address. The author's name, academic or professional affiliation, e-mail address, and full address should be included on the first page. All correspondence will be only with the corresponding author (should be indicated), including any on editorial decisions.

Abstract. The abstract should precede the article and in approximately 150–200 words outline briefly the objectives and main conclusions of the paper.

Introduction. The introduction should describe briefly the area of study and may give an outline of previous studies with supporting references and indicate clearly the objectives of the paper.

Materials and Methods. The materials used, the procedures followed with special reference to experimental design and analysis of data should be included.

Results. Data of significant interest should be included.

Figures. If submitted as a hard copy, line drawings (including graphs) should be in black on white paper. Alternatively sharp photoprints may be provided. The lettering should be clear. Halftone illustrations may be included. They should be submitted as clear black and white prints on glossy paper. The figures should be individually identified lightly in pencil on the back. All legends should be brief and typed on a separate sheet.

Tables. These should have short descriptive titles, be self explanatory and typed on separate sheets. They should be as concise as possible and not larger than a Journal page. Values in tables should include as few digits as possible. In most cases, more than two digits after the decimal point are unnecessary. Units of measurements should be SI units. Unnecessary abbreviations should be avoided. Information given in tables should not be repeated in graphs and vice versa.

Discussion. The contribution of the work to the overall knowledge of the subject could be shown. Relevant conclusions should be drawn, and the potential for further work indicated where appropriate.

Acknowledgements. Appropriate acknowledgements may be included.

Reprints. Twenty copies of reprints will be given free to all the authors. Authors who require more reprints may obtain them at cost provided the Editorial Committee is informed at the time of submission of the manuscript.

Correspondence

All enquiries regarding the ASM Science Journal, submission of articles, including subscriptions to it should be addressed to:

The Editor-in-Chief
ASM Science Journal
Academy of Sciences Malaysia
902-4, Jalan Tun Ismail
50480 Kuala Lumpur, Malaysia.
Tel: 603-2694 9898; Fax: 603-2694 5858
E-mail: sciencejournal@akademisains.gov.my

ASM SCIENCE JOURNAL
(ASM Sc. J.)

ORDER FORM

Subscription (Two issues per year)

	Malaysia	Other Countries
Individual	**RM100**	**USD50**
Institution	**RM200**	**USD100**

1. Complete form and return.

Name/Institution: .....
(Please print)
.....
.....

Street Address: .....
.....
. .

City, Region: .....

Country, Postal Code: .....

2. Payment method: Cheque/Bank Draft/Postal Order/
Money Order No.: .....
Payable to **"Akademi Sains Malaysia"**
(Please include bank commission, if applicable)
RM/USD: .....

Date: ..... Signature: .....

Please send to:
Academy of Sciences Malaysia
902-4, Jalan Tun Ismail
50480 Kuala Lumpur, Malaysia
Tel: 03-2694 9898; Fax: 03-26945858
E-mail: sciencejournal@akademisains.gov.my

ASM Science JOURNAL

In Pursuit of Excellence in Science

Affix
stamp
here

Academy of Sciences Malaysia
902-4, Jalan Tun Ismail
50480 Kuala Lumpur
Malaysia

RESEARCH ARTICLES

REVIEW

SCIENCE FORUM

ANNOUNCEMENTS